Beamforming Approaches for Ultrafast Nonlinear Ultrasound Imaging

Ting-Yu Lai

A dissertation

submitted in partial fulfillment of the requirements for the degree of

Doctor of Philosophy

University of Washington

2021

Reading Committee:

Mike Averkiou, Chair

Matthew O'Donnell

Matthew Bruce

Thanasis Loupas

Lilo Pozzo

Program Authorized to Offer Degree:

Bioengineering

University of Washington

Abstract

Beamforming Approaches for Ultrafast Nonlinear Ultrasound Imaging

Ting-Yu Lai

Chair of the Supervisory Committee:

Mike Averkiou

Department of Bioengineering

Recent advances in ultrafast contrast imaging have facilitated innovations such as super-resolution imaging and ultrafast contrast-enhanced Doppler imaging (**Chapter 1**). It has become evident that combining ultrafast imaging with tissue harmonic imaging (THI) may offer improvements in image quality in clinical areas such as 4D THI and harmonic color flow (**Chapter 1**). In the first half of this work, we investigated the feasibility of combining ultrafast imaging with THI. We began with developing a numerical solution based on the Khokhlov-Zabolotskaya-Kuznetsov (KZK) to model the nonlinear propagation of sound beams produced by diagnostic arrays in tissue (**Chapter 2**). We then expanded our research for ultrafast THI and investigated the harmonic generation of a matrix array for identifying optimal beamforming strategies for 4D cardiac THI (**Chapter 3**). In the second half of this work, we proposed imaging approaches for improving tissue signal suppression and contrast sensitivity for ultrafast contrast imaging. We began with investigating the linear signal cancellation (tissue signal suppression) performance of the Verasonics research ultrasound scanner and compared it with the Philips iU22 (**Chapter 4**). We then studied the phase response of the microbubbles and tissue, and presented evidence that unique microbubble nonlinear dynamics can produce a phase response that can be used as a segmentation tool to further improve tissue signal suppression in contrast imaging (**Chapter 5**). Finally, we identified an aperture pattern for AM that improves the tissue signal suppression compared to the conventional AM. We also demonstrated that the additional phase response induced by the spatial difference between complementary half amplitude fields in OAM pulse sequences is useful for improving phase segmentation and image contrast (**Chapter 6**). We concluded with a summary of all the results and accomplishments and future directions of this work (**Chapter 7**).

DEDICATION

To my parents, Mei-Ru and Ching-Te,
my wife, Hsiao-I,
and my son, Aaron.

ACKNOWLEDGEMENTS

The research reported in this study was partially supported by the National Institute of Biomedical Imaging and Bioengineering of the National Institutes of Health under Award Number T32EB001650 and College of Engineering Fellowship from the James Chao-Yao Koh and Maria Lee Koh Endowed Fellowship fund. All acknowledgements to individuals are included following their respective chapters.

This thesis would have not been possible without the support of many people. First, I would like to express my gratitude and appreciation to my advisor, Dr. Mike Averkiou, for his support and guidance throughout my Ph.D. studies. I've learned from him the value of attention to detail and critical thinking and the art of communicating science to others. I will definitely miss our long discussions on research and life lessons. I would also like to thank my Supervisory Committee: Dr. Matthew O'Donnell, Dr. Matthew Bruce, Dr. Thanasis Loupas, and Dr. Lilo Pozzo for their scientific advice and insightful discussions. I would also want to forward special thanks to Dr. Geng-Shi Jeng for sharing his knowledge and expertise in ultrasound imaging as well as advice for signal processing.

I will also take the opportunity to thank my earlier mentors, Dr. Chung-Chiun Liu, Dr. Fu-Chan Wei, Dr. Yon-Hua Tzeng, and Dr. Chih-Chung Huang, who have been supporting and guiding me throughout my research career.

It has been an honor to work alongside all these talented individuals: Sara Keller, Eric Juang, Alicia Clark, Dingjie Suo, Richard Zong, Conner Pitts, Ryan Hammond, David Li, and the rest of the uWAMIT lab. Thank you all for your support that has shaped me into a better person. Special thanks to Chih-Yen Chien, for being my "coffee buddy" for all these years. I am also grateful to Alex Hannah for teaching me how to program Verasonics Vantage System.

This work would have not been possible without the warmest support from my best friend, soul-mate, and wife, Hsiao-I Chen, during all these years. Thank you for your unconditional love and willing to watch Evangelion movies and other Japanese anime with me. I am also unconditionally

grateful to my parents, Mei-Ru Wu and Ching-Te Lai, for their love and unwavering support throughout my life and for being such a good role model. Finally, I would like to thank my son, Aaron Lai, for bringing joy to my life and giving me a chance to become your role model.

CONTENTS

LIST OF FIGURES

LIST OF TABLES

Chapter 1. INTRODUCTION

Abstract

Ultrasound is an important tool in diagnosing a wide variety of conditions affecting the organs and soft tissues of the body. Nonlinear ultrasound imaging techniques such as tissue harmonic imaging (THI) and contrast enhanced ultrasound (CEUS) offer additional clinical benefits that improve the accuracy of the diagnosis. THI improves image quality by reducing image artifacts from phase aberrations and multiple reverberations, which are often encountered in echocardiography. CEUS provides information of the microvasculature and perfusion kinetics and is clinically used for left ventricle opacification, myocardial perfusion and liver lesion detection and characterization. Previous studies have demonstrated the possibility of achieving 20,000 frames per second with ultrafast imaging techniques, over 500-fold compared to conventional ultrasound imaging in a scanning protocol often referred to as ultrafast imaging. Combining ultrafast imaging with THI or CEUS may allow physicians to examine the subtle changes in tissues and tumors in order for better diagnosis. In this chapter, the previous work and current barriers of combining ultrafast imaging with THI or CEUS will be covered. Additionally, the overall research aim of the project and the summary of this thesis will be presented.

1.1 NONLINEAR ULTRASOUND IMAGING

1.1.1 *Tissue harmonic imaging- Nonlinear propagation in tissue*

At low mechanical index (MI<0.1), tissue behaves in a linear fashion and the propagation of ultrasound waves is often assumed to be a linear process. In this case the compressional and rarefactional phase of the wave travel at a constant velocity, maintain the shape of the wave as they propagate [1]. Harmonic signals at higher frequencies ($n*f_0$, where n is an integer) than the central frequency (f_0) of ultrasound wave will not be generated as ultrasound wave linearly propagates in the tissue. However, At high MI (MI>0.1), tissue behaves in a nonlinear fashion [1, 2]. As a result, the propagation speed of the ultrasound wave is not constant, and the compressional phase of the wave travels faster than the rarefactional phase of the wave. [3-5]. This difference in propagation speed distorts the ultrasound wave and generates a finite amount of harmonics (**Fig. 1.1**) [6]. Although the amount of harmonics that tissue generates at any given instant remains small, the harmonics build as the ultrasound wave propagates in tissue [7]. The significance of nonlinear propagation with medical ultrasound was predicted by Muir et al. in a previous study [8]. In addition, some of the first measurements of nonlinear propagation through tissue were performed by Starritt et al. in a previous study [9]. However, earlier studies believe that tissue can be modeled as linear. It was not until 1997 when researchers who studied the harmonic components microbubble echoes realized that tissue could also produce diagnostically useful harmonic components and used it for imaging [10].

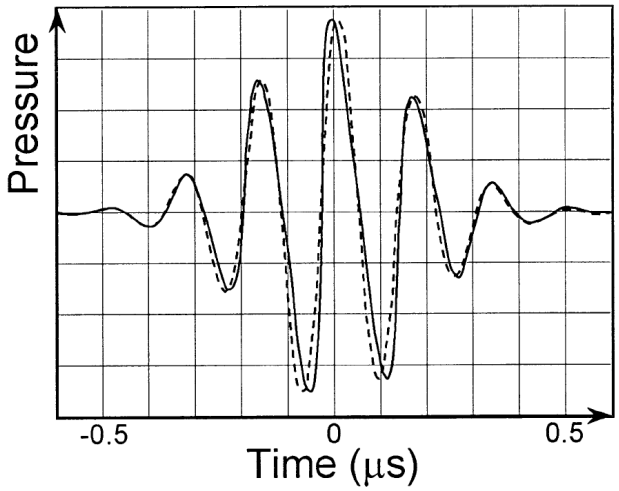

Fig. 1.1. Distortion of the acoustic pulse during propagation within the tissue. The dotted line represents the pulse at 0 cm and the solid line this pulse at 10 cm. Figure adapted from [2].

1.1.2 *Tissue harmonic imaging- advantages of using THI*

The advantages of THI include: Improved signal-to-noise ratio (SNR) and contrast-to-noise ratio (CNR). Images produced with THI [**Fig. 1.2** (b)] often have better SNR and CNR compared to conventional B-mode ultrasound images [**Fig. 1.2** (a)] of cysts and abnormalities that contain fat, calcium, or air [11, 12]. The primary cause of image noise and artifacts are beam distortion and multiple scattering from fat, skin layers and hydration level [2]. In addition, image artifacts may also be generated by side lobes, grating lobes, and body wall reverberations [13, 14]. Since nonlinear propagation is amplitude dependent, artifacts from side lobes, grating lobes, and multiple scattering that have weaker amplitude are greatly reduced in THI [15]. Moreover, since nonlinear components are gradually generated in tissue, body wall reverberation artifacts are dramatically reduced in THI [12, 15]. The spatial resolution is also improved. Since THI utilizes the 2^{nd} harmonic component, the narrowing of the lateral beamwidth improves the lateral resolution [12]. In addition, The decrease of the wavelength of the return harmonic signal compared to the fundamental improves the axial resolution [2]. Finally, since phase aberration and repeated image artifacts throughout the depth are reduced in THI, the visualization of deep structures is improved in THI compared to that in conventional B-mode imaging [1, 2]. To further improve the visualization of tissue at deeper depth, a lower transmitted frequency than that in B-mode imaging could be used in THI [2]. Although a lower transmitted frequency is used in THI, the axial and lateral resolution in THI would still be better than that in B-mode imaging since THI form the images with harmonics signals.

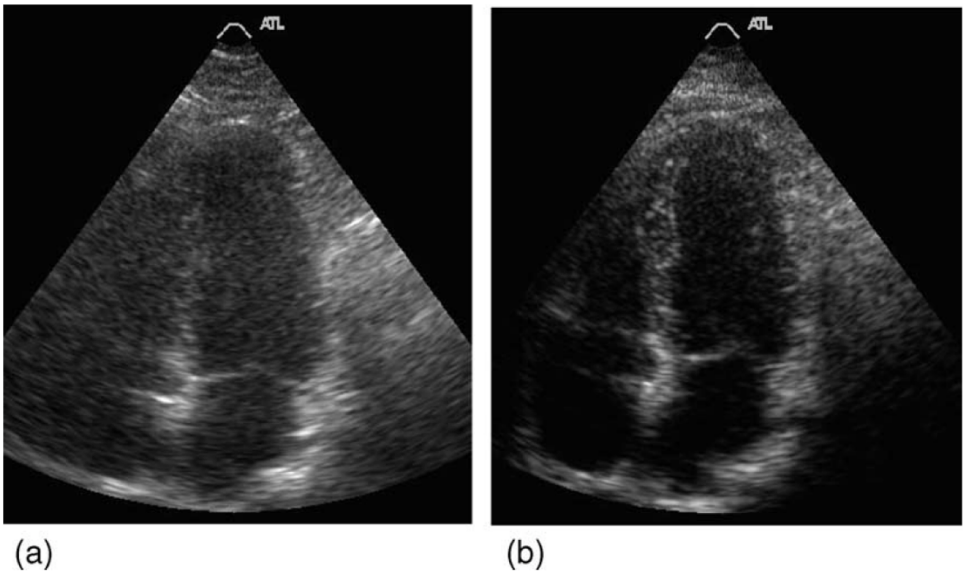

Fig. 1.2. A cardiac image showing a 4-chamber view of the heart in conventional B-mode imaging (a), and harmonic imaging (b). Figure adapted from [12].

1.1.3 *Contrast-enhanced ultrasound – nonlinear oscillation of microbubbles*

In the presence of an ultrasound wave, microbubbles undergo volumetric oscillations that generate signals for contrast enhancement [16]. When the local pressure is higher than ambient pressure, the microbubble contracts, whereas when the local pressure is lower than ambient pressure, the microbubble expands. Scattering by a microbubble is approximately linear if the incident ultrasound wave has a very low peak pressure amplitude (<0.03 MPa) [17]. However, if the pressure amplitude of the ultrasound wave is increased, the contraction and expansion of the microbubble become nonlinear. Since the movements of the microbubble wall are nonlinear, the echo is also nonlinear and the shape of the echo becomes asymmetric. As a result, microbubbles scatter the transmitted frequency (f_0) as well as harmonics of the transmitted frequency ($n*f_0$, where n is an integer) [17, 18].

Although many approaches have be proposed for contrast enhanced ultrasound (CEUS) imaging [19-21], optimal CEUS imaging is usually achieved at low MI ($\leq$0.1) which avoids microbubble destruction and at the same time limit the generation of tissue harmonics. At low MI, harmonic signals in CEUS are only produced by microbubbles, producing a microbubble-only image based on nonlinear backscattered signals. Performing CEUS imaging at low MIs reduces the generation

of tissue harmonics and thus enhances the contrast-to-tissue ratio (CTR), which is an essential parameter in quantifying the performance of contrast-specific imaging methods [18].

1.1.4 *Contrast-enhanced ultrasound – advantages of using CEUS*

Unlike MRI and CT, CEUS has high temporal resolution to capture the temporal enhancement of the lesion which is a feature often used for distinguishing benign from malignant pathology (**Fig. 1.3**). Such features of the enhancement pattern of lesions include the discontinuous peripheral nodular enhancement and centripetal fill-in seen with hemangiomas, or arterial phase hyperenhancement and delayed washout seen in hepatocellular carcinoma [22]. The blood pool nature of ultrasound contrast agents allows quantification of blood flow in both the macro- and microcirculation [18]. Blood flow in organ can be assessed within the image plane after the passage of a bolus injection of contrast agent administered into a peripheral vein. The technique consist of collecting a CEUS video loop after a bolus injection of microbubbles, placing a region of interest on the image and plotting the linearized image intensity as a function of time, referred to as the time-intensity curve (TIC) [18]. TIC provides important functional parameters of the vasculature [18, 23] and it is used in the diagnosis of renal and liver cancer [24, 25] or evaluating tumor response after treatment [26].

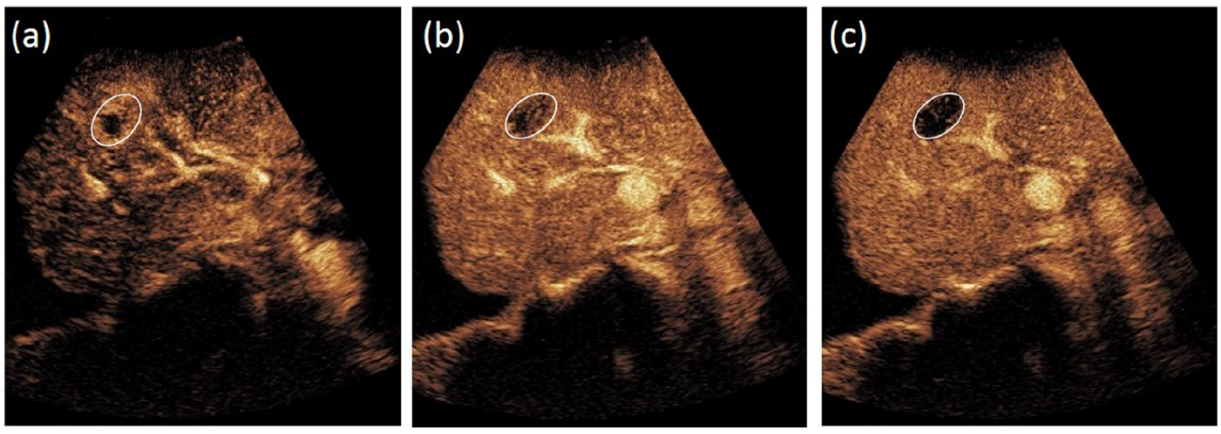

Fig. 1.3. CEUS images of a colorectal liver metastasis that show tumor enhancement in the different vascular phases. Images at the peak of the arterial phase (a), the peak of the portal venous phase (b) and the late portal phase (c). Figure adapted from [18].

1.1.5 *Nonlinear pulsing schemes*

Harmonic signals are isolated by filtering [10], or with nonlinear pulsing schemes such as pulse inversion (PI) [12], or amplitude modulation (AM) [27]. Earlier implementations relied on digital filtering techniques that isolate the harmonic component of the signal to form the image. However, this approach leads to poor axial resolution since it requires the use of longer pulses at lower frequencies (with narrower bandwidths) in order for the fundamental and the 2nd harmonic components to be separable in the frequency domain and still fit in the frequency bandwidth of the transducer [18]. Even then, the overlap between the fundamental and second harmonic components cannot be separated with filtering, thus contributing to tissue cluttering and the degradation of the image [17].

To overcome the limitations mentioned above, nonlinear pulsing schemes have been developed. In nonlinear pulsing schemes, the scattered echoes from a series of transmitted pulses are combined in a way that the linear signals are cancelled while the nonlinear signals are detected [18, 28]. The two most used nonlinear pulsing schemes today are PI and AM. PI involves transmitting 2 pulses with the second pulse being the inverse of the first pulse (they differ in phase by π). By adding the produced echoes, the fundamental and all odd harmonics are removed even without any RF-filtering operation and the second and all even harmonics are detected. The AM technique involves transmitting 2 pulses at different amplitudes. A widely used version of AM is one where the amplitude of the second pulse is half that of the first pulse; the linear signals are removed by scaling the echoes of the second pulse by a factor of 2 and then subtracting them from the echoes of the first. Both PI and AM avoid the limitations of filter-based techniques (i.e., poor axial resolution and imperfect separation of linear and nonlinear signals) but at the expense of reduced frame rate due to multiple firings.

Previous studies have shown that implementing AM with complimentary apertures improves tissue signal cancellation and requires less complex hardware [29]. Checkerboard apertures are used in some commercial ultrasound systems [18, 30]. This technique involves transmitting 3 pulses with the following sequence: p_{even}, p_{full}, and p_{odd}.With this technique, only even elements are used for transmitting p_{even}, only odd elements are used for p_{odd}, while all the elements are used for p_{full}. Since only half the elements are used for p_{even} and p_{odd}(when

considering AM with a factor of 2 between the two amplitudes), the pressure produced by either p_{even} or p_{odd}, is half of that produced by $p_{full.}$

1.2 ULTRAFAST IMAGING

1.2.1 *Gain and loss of using ultrafast imaging*

Conventional medical ultrasound images are acquired with a line-by-line scanning method, in which several elements of the array are excited in one transmit event to form a beam and insonify a portion of the field of view and this process is repeated until the full field of view is covered [31]. Although this scanning method provides good lateral resolution and suppression of off-axis scattering in the image, it also impacts the frame rate in requiring multiple transmits to form a complete ultrasound image [32]. Ultrafast imaging techniques such as plane wave imaging (PWI) and diverging wave imaging (DWI) excite a large number of the array elements to insonify the whole field of view in one transmit event while beamforming multiple lines on receive, allowing a significant improvement in frame rate. Previous studies have demonstrated the possibility of achieving 20,000 frames per second with PWI in imaging of a pigeon brain, over 500-fold compared to conventional ultrasound imaging [33, 34]. However, PWI/DWI compromises the quality of the image: first, lateral resolution is significantly degraded since PWI/DWI use the full aperture in one transmitting event [35, 36], but it can be partly recovered by coherent compounding [36, 37]. Second, the SNR is reduced in deeper areas of the image due to the unfocused nature of the transmitted beam and fixed elevation focus. In addition, phase aberrations caused by tissue inhomogeneity, and grating lobe and main lobe artifacts induced by steering plane or diverging waves may further compromise the contrast of the image [38, 39].

1.2.2 *Clinical utility of ultrafast imaging*

The high frame rate capability of ultrafast imaging has been utilized in shear wave elastography [40, 41], high sensitivity Doppler [42, 43], and functional ultrasound imaging of the brain [44, 45]. These innovations offer important diagnostic or prognostic information that might improve healthcare quality. Ultrafast imaging is used for various clinical applications discussed below.

- *Echocardiography*

The periods of the heart cycle requiring the highest temporal resolution are the periods during the isovolumic contraction/relaxation periods [46]. Isovolumic acceleration and the septal flash are

two important events that occur in these periods [47, 48]. Isovolumic acceleration is a measure of left ventricular contractility [47], while septal flash is a marker that is useful for cardiac resynchronization therapy [48]. Further study of these short-lived intervals with ultrafast imaging might provide additional data on prior to valve replacement. Another field potentially benefiting from ultrafast imaging is fetal echocardiography [46]where the optimal frame/volume rate for fetal tissue velocity imaging is around 150 to 200 Hz [49]. Finally, compared to conventional echocardiography, 4D echocardiography enables physicians to examine 3D cardiac structures in real-time and in a more complete manner. One of the major proven advantages of 4D echocardiography is the improved accuracy of the evaluation of cardiac chamber volumes [50] since it eliminates the need for geometric modeling and the errors caused by foreshortened views [51]. Ultrafast imaging may improve the volume rate of 4D echocardiography for better detection of subtle changes in cardiac motion and deformation pattern as well as in complex and transient myocardial events.

- *Diagnosing cancer*

One of the early changes that can differentiate cancer from normal tissues is malignant angiogenesis, which has been recognized as an important biomarker for cancer diagnostics [52]. Previous studies have utilized acoustic angiography to visualize the microvasculature and detect morphology abnormalities associated with tumor-induced angiogenesis in vivo [53]. However, the performance of this imaging technique suffered mainly from the limit of the spatial resolution constrained by the acoustic diffraction limit of the operating ultrasound frequency. Super-resolution imaging has allowed visualization of microvascular structures and flow beyond the diffraction limit through the localization of many spatially isolated microbubble signals [54, 55]. The spatial resolution of super-resolution imaging is down to a few microns [55]. Super-resolution imaging is capable of discriminating different tumor types based on the vasculature network [56] and longitudinally monitoring changes in the tumor microvascular network in response to the treatment [57].

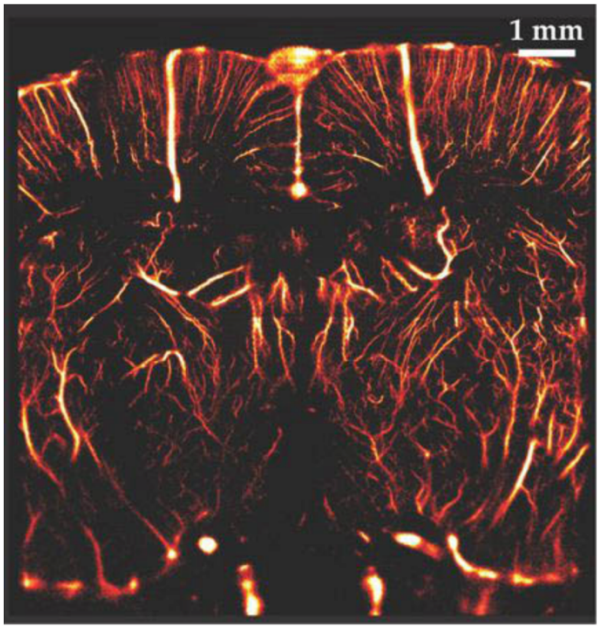

Fig. 1.4. An image of the vasculature network of a rat brain produced by super resolution imaging technique. Figure adapted from [55].

1.3 CHALLENGES OF COMBINING ULTRAFAST IMAGING AND THI

Combining PWI/DWI with THI (ultrafast THI) may offer improvements in CNR and SNR in ultrafast imaging. Although many studies believe it would be a challenge to produce sufficient harmonic components using plane/diverging waves [46, 58], no studies have reported acoustic field measurements or simulations of the nonlinear acoustic field produced by diagnostic arrays in PWI or DWI. Acoustic field measurements and simulations of the nonlinear acoustic fields produced by the diagnostic arrays are necessary to investigate the feasibility and trade-offs of combining PWI/DWI and THI.

1.4 CHALLENGES OF COMBINING ULTRAFAST IMAGING AND CEUS

Combining PWI/DWI and CEUS for ultrafast contrast imaging can provide high temporal resolution to accurately track the movement of the microbubbles [55] with advantages in visualizing low velocity flow in smaller coronary arteries [46, 59]. However, the crosstalk between transmitting and non-transmitting array elements in AM pulse sequences may compromise the degree of tissue signal suppression [18]. Moreover, the degree of crosstalk may be more severe in ultrafast CEUS compared to that in conventional focused ultrasound since larger apertures are used

for ultrafast imaging. Tissue signal suppression is important in CEUS to achieve good image contrast and microbubble specificity. Incomplete tissue signal cancellation may mask real enhancement caused by microbubbles or be incorrectly interpreted as real enhancement [18].

1.5 RESEARCH OBJECTIVES

Beamforming approaches for ultrafast THI are investigated in the first half of this work. The objective of the first half of this work is twofold: (1) to investigate the feasibility and trade-offs of combining ultrafast imaging and THI by quantifying the 2nd harmonic component generated by plane/diverging fields and (2) to utilize this knowledge to investigate the feasibility of implementing ultrafast THI in 4D echocardiography.

Beamforming approaches for ultrafast CEUS are investigated in the second half of this work. The objective of the second half of this work is threefold: (1) to investigate the linear signal cancellation performance in different nonlinear pulsing schemes to identify the optimal pulsing scheme for CEUS, (2) to study the microbubble dynamics and the phase response of the microbubbles in a nonlinear pulsing scheme, and (3) to utilize the knowledge in linear signal cancellation of the pulsing schemes and phase response of microbubbles to propose a beamforming approach that improves the tissue signal suppression in ultrafast CEUS.

1.6 THESIS STRUCTURE

In chapter 2, a numerical model based on KZK nonlinear parabolic wave equation is developed. The difference between the 2nd harmonic generated by conventional focused ultrasound and that generated by ultrafast imaging techniques is determined.

In chapter 3, we expanded our research to implement ultrafast imaging techniques in live 3D cardiac THI. We determined the trade-offs between produced 2nd harmonic level and volume rate when using different beamforming approaches for live 3D cardiac THI.

In chapter 4, the methodology for implementing PI and AM on a Verasonics research ultrasound scanner is presented. We determined the linear signal cancellation performance of a Verasonics scanner in PI or AM mode.

In chapter 5, we studied the dynamics of microbubble and investigated the degree of the phase difference between full and half amplitude pulses in AM pulse sequences generated by nonlinear propagation in tissue and nonlinear oscillation from free and shelled gas microbubbles

In chapter 6, we identified an aperture pattern for AM that improves the tissue signal cancellation for ultrafast CEUS. We also proposed and tested a new segmentation approach for ultrafast CEUS to further remove tissue signals.

Finally, chapter 7 briefly summarizes this thesis and discusses new applications and future directions of ultrafast THI and ultrafast CEUS.

1.7 REFERENCES

[1] A. Anvari, F. Forsberg, and A. E. Samir, "A primer on the physical principles of tissue harmonic imaging," *Radiographics,* vol. 35, no. 7, pp. 1955-1964, 2015.

[2] F. Tranquart, N. Grenier, V. Eder, and L. Pourcelot, "Clinical use of ultrasound tissue harmonic imaging," *Ultrasound in medicine & biology,* vol. 25, no. 6, pp. 889-894, 1999.

[3] J. D. Thomas and D. N. Rubin, "Tissue harmonic imaging: why does it work?," *Journal of the American Society of Echocardiography,* vol. 11, no. 8, pp. 803-808, 1998.

[4] F. A. Duck, "Nonlinear acoustics in diagnostic ultrasound," *Ultrasound in medicine & biology,* vol. 28, no. 1, pp. 1-18, 2002.

[5] V. F. Humphrey, "Nonlinear propagation in ultrasonic fields: measurements, modelling and harmonic imaging," *Ultrasonics,* vol. 38, no. 1-8, pp. 267-272, 2000.

[6] W. Law, L. Frizzell, and F. Dunn, "Determination of the nonlinearity parameter B/A of biological media," *Ultrasound in medicine & biology,* vol. 11, no. 2, pp. 307-318, 1985.

[7] W. S. Gan, *Acoustical imaging: techniques and applications for engineers*. John Wiley & Sons, 2012.

[8] T. Muir and E. Carstensen, "Prediction of nonlinear acoustic effects at biomedical frequencies and intensities," *Ultrasound in medicine & biology,* vol. 6, no. 4, pp. 345-357, 1980.

[9] H. Starritt, M. Perkins, F. Duck, and V. Humphrey, "Evidence for ultrasonic finite-amplitude distortion in muscle using medical equipment," *The Journal of the Acoustical Society of America,* vol. 77, no. 1, pp. 302-306, 1985.

[10] M. A. Averkiou, D. N. Roundhill, and J. E. Powers, "A new imaging technique based on the nonlinear properties of tissues," in *1997 IEEE Ultrasonics Symposium Proceedings. An International Symposium (Cat. No. 97CH36118)*, 1997, vol. 2, pp. 1561-1566: IEEE.

[11] S. Choudhry *et al.*, "Comparison of tissue harmonic imaging with conventional US in abdominal disease," *Radiographics,* vol. 20, no. 4, pp. 1127-1135, 2000.

[12] M. A. Averkiou, "Tissue harmonic ultrasonic imaging," *Comptes Rendus de l'Académie des Sciences-Series IV-Physics,* vol. 2, no. 8, pp. 1139-1151, 2001.
[13] T. Christopher, "Finite amplitude distortion-based inhomogeneous pulse echo ultrasonic imaging," *IEEE transactions on ultrasonics, ferroelectrics, and frequency control,* vol. 44, no. 1, pp. 125-139, 1997.
[14] D. Rubin *et al.*, "Why does tissue harmonic imaging improve image quality: a quantitative examination demonstrating side-lobe suppression," *Journal of the American College of Cardiology,* vol. 31, pp. 127-127, 1998.
[15] T. Whittingham, "Tissue harmonic imaging," *European radiology,* vol. 9, pp. S323-S326, 1999.
[16] K. Ferrara, R. Pollard, and M. Borden, "Ultrasound microbubble contrast agents: fundamentals and application to gene and drug delivery," *Annu. Rev. Biomed. Eng.,* vol. 9, pp. 415-447, 2007.
[17] T. A. Whittingham, "Contrast-specific imaging techniques: technical perspective," in *Contrast media in ultrasonography*: Springer, 2005, pp. 43-70.
[18] M. A. Averkiou, M. F. Bruce, J. E. Powers, P. S. Sheeran, and P. N. Burns, "Imaging methods for ultrasound contrast agents," *Ultrasound in medicine & biology,* vol. 46, no. 3, pp. 498-517, 2020.
[19] M. L. Main and P. A. Grayburn, "Clinical applications of transpulmonary contrast echocardiography," *American heart journal,* vol. 137, no. 1, pp. 144-153, 1999.
[20] T. Albrecht *et al.*, "Improved detection of hepatic metastases with pulse-inversion US during the liver-specific phase of SHU 508A: multicenter study," *Radiology,* vol. 227, no. 2, pp. 361-370, 2003.
[21] P. Burns, "Harmonic imaging with ultrasound contrast agents," *Clinical radiology,* vol. 51, pp. 50-55, 1996.
[22] P. G. Ranganath, M. L. Robbin, S. J. Back, E. G. Grant, and D. T. Fetzer, "Practical advantages of contrast-enhanced ultrasound in abdominopelvic radiology," *Abdominal Radiology,* vol. 43, no. 4, pp. 998-1012, 2018.
[23] C. Dietrich, M. Averkiou, J.-M. Correas, N. Lassau, E. Leen, and F. Piscaglia, "An EFSUMB introduction into Dynamic Contrast-Enhanced Ultrasound (DCE-US) for quantification of tumour perfusion," *Ultraschall in der Medizin-European Journal of Ultrasound,* vol. 33, no. 04, pp. 344-351, 2012.
[24] S. Aoki *et al.*, "Contrast-enhanced ultrasound using a time-intensity curve for the diagnosis of renal cell carcinoma," *BJU international,* vol. 108, no. 3, pp. 349-354, 2011.
[25] X. Pei *et al.*, "Quantitative analysis of contrast-enhanced ultrasonography: differentiating focal nodular hyperplasia from hepatocellular carcinoma," *The British journal of radiology,* vol. 86, no. 1023, p. 20120536, 2013.
[26] N. Lassau *et al.*, "Validation of dynamic contrast-enhanced ultrasound in predicting outcomes of antiangiogenic therapy for solid tumors: the French multicenter support for innovative and expensive techniques study," *Investigative radiology,* vol. 49, no. 12, p. 794, 2014.
[27] P. Jiang, Z. Mao, and J. Lazenby, "A new tissue harmonic imaging scheme with better fundamental frequency cancellation and higher signal-to-noise ratio," in *1998 IEEE Ultrasonics Symposium. Proceedings (Cat. No. 98CH36102)*, 1998, vol. 2, pp. 1589-1594: IEEE.

[28] M. A. Averkiou, C. Mannaris, M. Bruce, and J. Powers, "Nonlinear pulsing schemes for the detection of ultrasound contrast agents," *Journal of the Acoustical Society of America,* vol. 123, no. 5, p. 3110, 2008.
[29] C. Trembaly-Darveau, "Contrast-enhanced Doppler ultrasound imaging using plane waves," Ph.D. dissertation, Dept. Med. Biophys., Univ. Toronto, Toronto, ON, Canada, Jun. 2016.
[30] O. Couture, M. Fink, and M. Tanter, "Ultrasound contrast plane wave imaging," *IEEE transactions on ultrasonics, ferroelectrics, and frequency control,* vol. 59, no. 12, pp. 2676-2683, 2012.
[31] T. L. Szabo, *Diagnostic ultrasound imaging: inside out*. Academic press, 2004.
[32] P. R. Hoskins, K. Martin, and A. Thrush, *Diagnostic ultrasound: physics and equipment*. Cambridge University Press, 2010.
[33] M. Tanter and M. Fink, "Ultrafast imaging in biomedical ultrasound," *IEEE transactions on ultrasonics, ferroelectrics, and frequency control,* vol. 61, no. 1, pp. 102-119, 2014.
[34] R. Rau *et al.*, "3D functional ultrasound imaging of pigeons," *Neuroimage,* vol. 183, pp. 469-477, 2018.
[35] B. Lokesh and A. K. Thittai, "Spatial resolution improvement in Plane Wave Imaging using adaptive Sign Coherence Factor weighting," in *Ultrasonics Symposium (IUS), 2016 IEEE International*, 2016, pp. 1-4: IEEE.
[36] B. Denarie *et al.*, "Coherent plane wave compounding for very high frame rate ultrasonography of rapidly moving targets," *IEEE transactions on medical imaging,* vol. 32, no. 7, pp. 1265-1276, 2013.
[37] G. Montaldo, M. Tanter, J. Bercoff, N. Benech, and M. Fink, "Coherent plane-wave compounding for very high frame rate ultrasonography and transient elastography," *IEEE transactions on ultrasonics, ferroelectrics, and frequency control,* vol. 56, no. 3, pp. 489-506, 2009.
[38] J. Jensen, M. B. Stuart, and J. A. Jensen, "Optimized plane wave imaging for fast and high-quality ultrasound imaging," *IEEE transactions on ultrasonics, ferroelectrics, and frequency control,* vol. 63, no. 11, pp. 1922-1934, 2016.
[39] E. Tiran *et al.*, "Multiplane wave imaging increases signal-to-noise ratio in ultrafast ultrasound imaging," *Physics in medicine and biology,* vol. 60, no. 21, p. 8549, 2015.
[40] M. Dighe and M. Bruce, "Elastography of diffuse liver diseases," in *Seminars in roentgenology*, 2016, vol. 4, no. 51, pp. 358-366.
[41] J.-l. Gennisson *et al.*, "4-D ultrafast shear-wave imaging," *IEEE transactions on ultrasonics, ferroelectrics, and frequency control,* vol. 62, no. 6, pp. 1059-1065, 2015.
[42] M. Bruce, A. Hannah, C. Tremblay-Darveau, and P. Burns, "High frame-rate visualization of blood flow with ultrasound contrast agents," *The Journal of the Acoustical Society of America,* vol. 140, no. 4, pp. 3028-3028, 2016.
[43] M. Correia, J. Provost, M. Tanter, and M. Pernot, "4D ultrafast ultrasound flow imaging: in vivo quantification of arterial volumetric flow rate in a single heartbeat," *Physics in Medicine & Biology,* vol. 61, no. 23, p. L48, 2016.
[44] E. Macé, G. Montaldo, I. Cohen, M. Baulac, M. Fink, and M. Tanter, "Functional ultrasound imaging of the brain," *Nature methods,* vol. 8, no. 8, pp. 662-664, 2011.
[45] C. Demené *et al.*, "Spatiotemporal clutter filtering of ultrafast ultrasound data highly increases Doppler and fUltrasound sensitivity," *IEEE transactions on medical imaging,* vol. 34, no. 11, pp. 2271-2285, 2015.

[46] M. Cikes, L. Tong, G. R. Sutherland, and J. D'hooge, "Ultrafast cardiac ultrasound imaging: technical principles, applications, and clinical benefits," *JACC: Cardiovascular Imaging,* vol. 7, no. 8, pp. 812-823, 2014.

[47] M. Vogel *et al.*, "Noninvasive assessment of left ventricular force-frequency relationships using tissue Doppler–derived isovolumic acceleration: validation in an animal model," *Circulation,* vol. 107, no. 12, pp. 1647-1652, 2003.

[48] C. Parsai *et al.*, "Toward understanding response to cardiac resynchronization therapy: left ventricular dyssynchrony is only one of multiple mechanisms," *European heart journal,* vol. 30, no. 8, pp. 940-949, 2009.

[49] N. Elmstedt, B. Lind, K. Ferm-Widlund, M. Westgren, and L.-Å. Brodin, "Temporal frequency requirements for tissue velocity imaging of the fetal heart," *Ultrasound in obstetrics & gynecology,* vol. 38, no. 4, pp. 413-417, 2011.

[50] R. M. Lang, V. Mor-Avi, L. Sugeng, P. S. Nieman, and D. J. Sahn, "Three-dimensional echocardiography: the benefits of the additional dimension," *Journal of the American College of Cardiology,* vol. 48, no. 10, pp. 2053-2069, 2006.

[51] R. M. Lang, K. Addetia, A. Narang, and V. Mor-Avi, "3-Dimensional echocardiography: latest developments and future directions," *JACC: Cardiovascular Imaging,* vol. 11, no. 12, pp. 1854-1878, 2018.

[52] D. Hanahan and R. A. Weinberg, "The hallmarks of cancer," *cell,* vol. 100, no. 1, pp. 57-70, 2000.

[53] R. C. Gessner, C. B. Frederick, F. S. Foster, and P. A. Dayton, "Acoustic angiography: a new imaging modality for assessing microvasculature architecture," *International journal of biomedical imaging,* vol. 2013, 2013.

[54] K. Christensen-Jeffries *et al.*, "Microbubble axial localization errors in ultrasound super-resolution imaging," *IEEE transactions on ultrasonics, ferroelectrics, and frequency control,* vol. 64, no. 11, pp. 1644-1654, 2017.

[55] C. Errico *et al.*, "Ultrafast ultrasound localization microscopy for deep super-resolution vascular imaging," *Nature,* vol. 527, no. 7579, pp. 499-502, 2015.

[56] T. Opacic *et al.*, "Motion model ultrasound localization microscopy for preclinical and clinical multiparametric tumor characterization," *Nature communications,* vol. 9, no. 1, pp. 1-13, 2018.

[57] D. Ghosh *et al.*, "Monitoring early tumor response to vascular targeted therapy using super-resolution ultrasound imaging," in *2017 IEEE international ultrasonics symposium (Ius)*, 2017, pp. 1-4: IEEE.

[58] W. Guo, Y. Wang, and J. Yu, "Ultrasound Harmonic Enhanced Imaging Based on the Eigen Decomposition," *Journal of Medical Imaging and Health Informatics,* vol. 6, no. 5, pp. 1276-1281, 2016.

[59] V. Mor-Avi, E. G. Caiani, K. A. Collins, C. E. Korcarz, J. E. Bednarz, and R. M. Lang, "Combined assessment of myocardial perfusion and regional left ventricular function by analysis of contrast-enhanced power modulation images," *Circulation,* vol. 104, no. 3, pp. 352-357, 2001.

Chapter 2. MODELING OF THE ACOUSTIC FIELD PRODUCED BY DIAGNOSTIC ULTRASOUND ARRAYS IN PLANE AND DIVERGING WAVE MODES

Abstract

Combining plane and diverging wave imaging (PWI/DWI) with tissue harmonic imaging (THI) may offer improvements in image quality in applications such as 4D THI and harmonic color flow. However, no studies have reported simulations of the nonlinear acoustic fields produced by diagnostic arrays in either plane or diverging wave mode. The aim of this work is to model three typical diagnostic arrays that are used in clinical practice and research, the Verasonics L11-4v linear array, C5-2v convex array, and P4-2v phased array with the KZK equation. We showed in linear simulations that using such arrays for ultrafast contrast imaging produced pressures that are greater in the nearfield and lower in the farfield than those of focused beams, and thus may induce more nearfield bubble destruction. In nonlinear simulations, the second harmonic produced by ultrafast THI was found to be 2-16 dB lower than that of focused beams for all arrays considered when operated at the same MI. This moderate difference of the second harmonic between PWI/DWI and focused ultrasound suggests it is feasible to combine PWI/DWI and THI. We have also investigated harmonic generation produced by diagnostic matrix arrays for 4D THI and found that beamforming approaches with shallow foci produced the highest peak 2nd harmonic in tissue yet lowest volume rate. Beamforming approaches with deep foci produced the highest 2nd harmonic at imaging depth of 150 mm. The volume rate of 4D cardiac THI performed with focused ultrasound, PWI, and DWI is 1.7-20, 81, and over 1275 Hz, respectively.

2.1 INTRODUCTION

Conventional medical ultrasound images are acquired with a line-by-line scanning method, in which several elements of the array are excited in one transmit event to form a beam and insonify a portion of the field of view [1]. Although this scanning method provides good lateral resolution and suppression of off-axis scatters of the image, it also impacts the frame rate in requiring multiple transmits to form a complete ultrasound image [2].

High frame rate imaging techniques such as plane wave imaging (PWI) and diverging wave imaging (DWI) excite a large number of the array elements to insonify the whole field of view in one transmit event, allowing a significant improvement in frame rate. Previous studies have demonstrated the possibility of achieving 20,000 frames per second with PWI, over 500-fold compared to conventional ultrasound imaging [3]. This high frame rate capability has enabled innovations such as shear wave elastography [4], ultrafast Doppler capabilities [5], and functional ultrasound imaging of brain activities [6]. However, PWI/DWI compromises the quality of the image: first, lateral resolution is significantly degraded since PWI/DWI use the full aperture in one transmitting event [7, 8], but it can be partly recovered by coherent compounding [8, 9]. Second, the signal-to-noise ratio (SNR) is reduced in deeper areas of the image due to the unfocused nature of the beam and fixed elevation focus. In addition, phase aberrations caused by tissue inhomogeneity, and grating lobe and main lobe artifacts induced by steering plane/diverging waves may further compromise the contrast of the image [10, 11].

Tissue harmonic imaging (THI) improves image quality and reduces phase aberrations and reverberations in diagnostic ultrasound using focused beams [12]. As ultrasound waves propagate in tissue, harmonic components are gradually generated due to nonlinear propagation. THI utilizes the second or higher harmonic component to form the image by filtering, pulse inversion [12], or power modulation [13]. Since nonlinear propagation is pressure amplitude dependent, artifacts from side lobes, grating lobes, and multiple scattering that have weaker pressure amplitude are reduced in THI [14]. Moreover, since nonlinear components are gradually generated in tissue, body wall reverberation artifacts are dramatically reduced in THI [12, 14].

Combining PWI/DWI and THI for ultrafast THI may offer improvements in contrast-to-noise ratio (CNR) and signal-to-noise-ratio (SNR) in PWI/DWI. Although many studies believe it would be a challenge to produce sufficient harmonic components using plane/diverging waves [15, 16], recent studies have shown the possibility of combining PWI/DWI and THI, with reduced clutter by 13.8 dB [17, 18]. However, to the best of our knowledge, although a previous study has shown the simulation of linear acoustic field of PWI and DWI [19], no studies have reported acoustic field measurements or simulations of the nonlinear acoustic field produced by diagnostic arrays in either PWI or DWI. This is the first study to quantitatively investigate the axial beam profiles of PWI/DWI in comparison with typically used focused beams, as previous studies have concentrated more on azimuthal aspects. Acoustic field measurements and simulations are necessary to investigate the feasibility and trade-offs of combining PWI/DWI and THI.

Contrast-enhanced ultrasound (CEUS) is a real-time imaging technique that is capable of visualizing the vasculature and perfusion of organs and tumors [20, 21]. Combining PWI/DWI and CEUS for ultrafast contrast imaging can provide high temporal resolution to accurately track the movement of the microbubbles [22, 23] with advantages in visualizing low velocity flow in smaller coronary arteries [15]. However, a previous study has observed increased bubble destruction in ultrafast contrast imaging compared to conventional focused ultrasound [24]. The characteristics of the beam produced by diagnostic arrays such as the uniformity of the field and the spatial extent of the mechanical index (MI) of the pulse are therefore crucial to ultrafast contrast imaging to avoid bubble destruction, and further optimize its image quality.

The Khokhlov-Zabolotskaya-Kuznetsov (KZK) nonlinear parabolic wave equation has been used to study the nonlinear propagation of pulsed finite amplitude sound beams in thermoviscous fluids [25, 26]. The equation describes the combined effects of diffraction, thermoviscous absorption, and nonlinearity [27, 28]. Numerical solutions have been proposed to model the nonlinear sound propagation of axisymmetric sources (i.e., circular) by solving the KZK equation in either the frequency domain [29, 30] or the time domain [12, 31], and found good agreement with acoustic field measurements. Although numerical solutions for focused non-axisymmetric sources (i.e., rectangular) have been developed [32, 33], no solution has been proposed for modeling unfocused non-axisymmetric source, which is an essential piece for modeling the diagnostic array in plane

wave mode. In addition, diagnostic ultrasound arrays have an acoustic lens in the elevation dimension. Thus, a numerical solution that combines a focused (in elevation dimension) and unfocused (in azimuthal dimension) non-axisymmetric source would be helpful to accurately model diagnostic arrays in plane wave mode.

The aim of the present study was to model the 3 most commonly used arrays in diagnostic ultrasound, the Verasonics L11-4v linear array, C5-2v convex array, and P4-2v phased array, each targeting a specific imaging application, with the KZK nonlinear parabolic wave equation to explore the impact of using plane/diverging waves for both contrast and tissue harmonic imaging. The nonlinear field produced by these 3 arrays in plane/diverging modes has not been investigated in the past. We have 2 specific objectives: first, to investigate the penetration of the ultrafast contrast imaging, and whether there is increased bubble destruction due to the nature of the plane and diverging fields in low MI (MI<0.1) contrast imaging; and second, to investigate the feasibility of combining PWI and THI by quantifying the second harmonic component generated by these fields, and the penetration of the ultrafast THI.

2.2 MATERIALS AND METHODS

2.2.1 *Numerical solution*

The KZK equation for the focused diagnostic array can be numerically solved in dimensionless form by introducing five normalized variables [1, 2]:

$$\frac{\partial P}{\partial \sigma} = \int_{-\infty}^{\tau} \left(\frac{1}{4G_x}\frac{\partial^2 P}{\partial \chi^2} + \frac{d_{xy}}{4G_y}\frac{\partial^2 P}{\partial \psi^2}\right) d\tau' + A\frac{\partial^2 P}{\partial \tau^2} + NP\frac{\partial P}{\partial \tau}. \quad (2.1)$$

where, $P = p/p_0$, $\sigma = z/d_x$, $\chi = x/a_x$, $\psi = y/a_y$, $\tau = \omega_0 t'$, p and p_0 are the acoustic and source pressure, respectively, z is the propagation axis of the sound beam, d_x is the azimuthal focus of the array, and a_x and a_y are the half-apertures of the array in azimuthal and elevation direction, respectively. ω_0 is the characteristic angular frequency, and t' is the retarded time such that $t' = t - {}^{z}/_{c_0}$, where c_0 is the speed of sound. d_{xy} is the ratio between focal length in azimuthal and elevation dimension (i.e., $d_{xy} = d_x/d_y$ as shown in **Fig. 2.1**). x and y are the azimuthal and elevation coordinates, respectively.

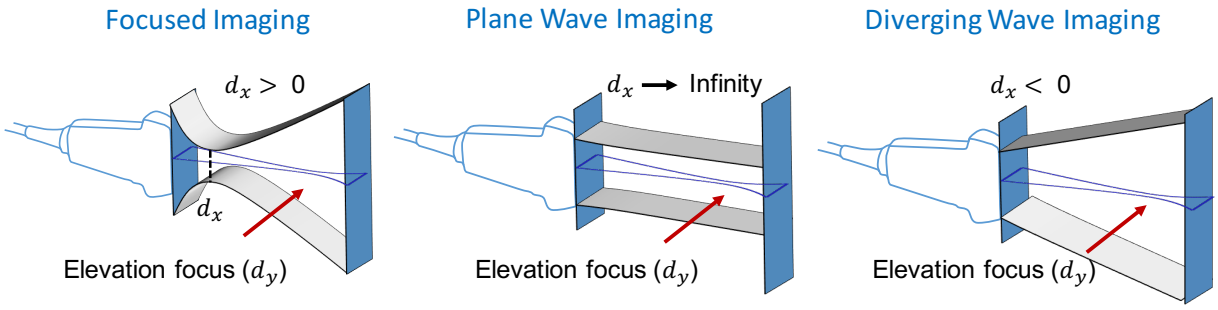

Fig. 2.1. Schematic of the azimuthal and elevation foci of a (a) conventional focused linear array, and a linear array with elevation focus operated in (b) plane wave mode, and (c) diverging wave mode.

The first term, second term, and third term on the right hand side of equation (2.1) account for diffraction, thermoviscous dissipation, and quadratic nonlinearity of the medium, respectively. Each term is described by a dimensionless parameter as follows:

$$G_x = z_0/d_x\,; \quad G_y = z_0/d_y; \quad (2.2)$$

$$A = \alpha_0 d_x. \quad (2.3)$$

$$N = d_x/\bar{z}. \quad (2.4)$$

G_x and G_y in equation (2.2) are the focusing gain in the azimuthal and elevation direction, respectively. z_0 is the Rayleigh distance, with $z_0 = \omega_0 a^2/2c_0$. A in equation (2.3) is the attenuation parameter, where α_0 is the thermoviscous attenuation coefficient, and $\alpha_0 = \delta{\omega_0}^2/2{c_0}^3$. N in equation (2.4) is the nonlinearity parameter, where $\bar{z}$ is the plane wave shock formation distance, and $\bar{z} = \rho_0 c_0^3/\beta\omega_0 p_0$, where β is the nonlinearity coefficient.

An appropriate boundary condition for the source at $\sigma = 0$ is:

$$P = f\left(\tau + G_x\chi^2 + G_y\psi^2\right)H(1-\chi)H(1-\psi). \quad (2.5)$$

The source function $f(\tau)$ used in present study was:

$$f(\tau) = \exp[-(\tau/N_c\pi)^{2m}]sin[\tau + \phi]. \quad (2.6)$$

where H is the Heaviside step function, and m and N_c indicate the shape of the envelope and number of cycle of the pulse, respectively. The pulse we used in the present study has 3.5 cycles ($N_c = 3.5$) with a hyper-Gaussian envelope ($m = 2$). This combination of m and N_c results in pulses that are very similar with what is being used in clinical diagnostic systems. The specific dimensions of the arrays and the parameters required by the numerical code are shown in **Table 2.1**. At the edges of numerical grid, the following boundary conditions were imposed: $P = 0$ at $= \chi_{max}$, $\psi = \psi_{max}$, $\tau = \tau_{min}$, and $\tau = \tau_{max}$. The values of τ_{min}, τ_{max}, χ_{max}, and ψ_{max} are shown in **Table 2.2** and were chosen carefully to minimize numerical errors coming from reflections from the boundary of the numerical grid. In the following section, we explain how the plane and diverging wave fields are modeled in the boundary condition through the term G_x.

Table 2.1: Specifications of imaging arrays.

Specifications of Imaging Arrays	**L11-4v**	**P4-2v**	**C5-2v**
Operating Frequency	4MHz	2MHz	2MHz
Element width	0.3 mm	0.3 mm	0.5 mm
Number of elements	128	64	128
Array width/radius	38.4 mm	19.2 mm	49.6 mm
Elevation	5 mm	14 mm	14 mm
Elevation focus	20 mm	60 mm	60 mm
Number of elements used in plane/diverging wave mode	128	64	128
Number of elements used in focused mode	30	64	36
Azimuthal focus in focused mode	30 mm	77 mm	77 mm

Table 2.2: Parameters for numerical solution.

Parameters for Numerical Solution (PWI/DWI)	**L11-4v**	**P4-2v**	**C5-2v**
Number of azimuthal steps (x) per aperture	100	150	500
Number of elevation steps (y) per aperture	40	40	40
Maximum azimuth coordinate (χ_{max})	10	10	5
Maximum elevation coordinate (ψ_{max})	10	5	5
Minimum time coordinate (τ_{min}) in cycles	-10	-10	-10
Maximum time coordinate (τ_{max}) in cycles	13	70	95
IBFD step size ($\Delta\sigma$)	1×10^{-9}	1×10^{-3}	5×10^{-4}
CNFD step size ($\Delta\sigma$)	4×10^{-9}	4×10^{-3}	2×10^{-3}

2.2.2 *Modeling diagnostic arrays in PWI and DWI*

For modeling the L11-4v array in PWI, the depth of view was 4 cm, consistent with a typical depth of view in vascular imaging (4 cm is the default depth in Carotid imaging on the Philips iU22 scanner). Since the unfocused source is equivalent to the focused source focused at infinity [3, 4],

we modeled the L11-4v array in plane wave mode by placing the azimuthal focus at infinity (10^3 m). This resulted in a very low focusing gain (G_x =0.003) that would essentially remove the time delay term in azimuthal dimension ($G_x\chi^2$) in equation (2.5).

For modeling the C5-2v and P4-2v arrays in DWI, the depth of view was 15 cm, consistent with a typical depth of view in abdominal and cardiac imaging. To model the arrays in DWI, a virtual negative azimuthal focus was placed behind each transducer as it is shown in **Fig. 2.2**. For C5-2v, the virtual azimuthal focus is defined by the array curvature. For P4-2v, the virtual azimuthal focus was chosen in order to produce a 75-degree sector. For P4-2v the virtual azimuthal focus was -12.5 and for C5-2v was -39.3 mm. These values define G_x in equation (2.5). The schematic configurations of the 3 arrays operating in plane and diverging wave mode are shown in **Fig. 2.1**.

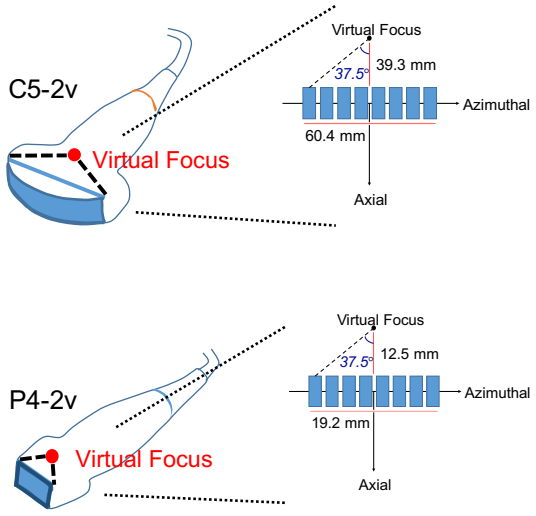

Fig. 2.2. The implementation of the virtual focus for numerical simulations for C5-2v and P4-2v arrays.

The Implicit Backward Finite Difference (IBFD) method and the Crank-Nicolson Finite Difference (CNFD) method were used to numerically solve the diffraction and absorption terms of equation (2.1) and an exact explicit solution was used for the nonlinear term [5, 6]. The discontinuity in the step function of the boundary condition produces numerical oscillations. The IBFD method is effective in damping these oscillations but since it is a first order approximation requiring a very small step size, it was only used for the first 100 steps. Beyond the oscillatory region, the CNFD method which is a second order approximation and allows for a much larger

step size, was used for the rest of the calculations. The step size used for IBFD and CNFD for each array are shown in **Table 2.1**. Since CNFD is more accurate (second order) and permits use of larger step sizes [5], the step size of CNFD was 4 times larger than the that of IBFD. For the temporal sampling of our waveforms, we have used different values according to the degree of nonlinearity. For the linear runs we sampled the waveforms at 20 points per cycle and for the nonlinear case 60 points per cycle. The discretization sizes of azimuthal and elevation steps were chosen based on previous studies [2, 5, 7] and by running benchmark cases for which analytical or exact solution is known.

2.2.3 *Linear Simulations-Ultrafast Contrast Imaging*

We first validated our proposed method (KZK) by comparing the simulations of PWI/DWI fields produced by the KZK with that produced by Field II, a widely used linear acoustic simulation capable of modeling the acoustic field of non-axisymmetric sources with arbitrary focusing, apodization, and attenuation [8, 9]. This comparison was necessary in order to evaluate the ability of KZK (which relies on the paraxial approximation) to calculate the diffraction integral for the types of sources we are considering in the present work. Field II which relies on the Rayleigh integral (superposition of point sources that comprise the boundary condition) is the exact linear solution, assuming adequate discretization. For the Field II simulations, each array was modeled with 200 MHz sampling frequency, 100 sub-division in element height, 100 sub-division in element width, and without kerf between each element on the array. Mean relative difference between KZK and Field II were calculated with the equation (2.7) below:

$$\sum_{i=1}^{n} \frac{|P_{Field\ II} - P_{KZK}|}{P_{Field\ II} \times n} \times 100\%, \quad (2.7)$$

where *i* indicates individual data point of the pressure in a plane, *n* indicates the total number of data points in the pressure contour, $P_{Field\ II}$ is the peak positive pressure produced by Field II, and P_{KZK} is the peak positive pressure produced by KZK.

Next, we compared the linear simulations (with Field II) of PWI/DWI fields with the focused beams (while taking into consideration of tissue attenuation) to investigate whether there is

increased bubble destruction in ultrafast imaging. The beamforming parameters used for focused beams are shown in **Table 2.1**. The 6 dB range of the axial field at the center of the arrays was calculated and used for comparing the spatial extent of the field produced in PWI/DWI and focused beams.

2.2.4 *Nonlinear Simulations-Ultrafast Tissue Harmonic Imaging*

Simulations of nonlinear propagation in water produced by the KZK were compared with hydrophone measurements in a water. The experimental set up is shown in **Fig. 2.3**. The L11-4v array was used. A membrane hydrophone (UC1604, Precision Acoustics, Dorset, UK), attached to the motion stage was used to measure the acoustic field produced by the diagnostic array in plane wave mode. We collected pressure contours on the azimuthal plane in MPa. The range of the motor stage was -20 to 20 mm in azimuth direction and 5 to 40 mm in axial direction. The step size of the motor stage was 0.5 mm in both azimuth and axial direction.

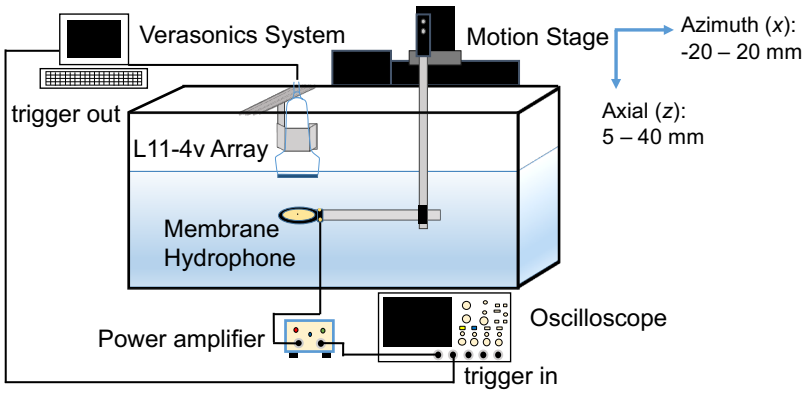

Fig. 2.3. Experimental set up for the acoustic field measurements.

We further compared the simulated tissue nonlinear field of PWI/DWI mode with conventional focused beam mode, in order to investigate harmonic generation and the feasibility of THI in PWI/DWI. We considered 3 azimuthal foci (shallow, moderate, and deep) for the focused beams when comparing their second harmonic with that of plane and diverging wave beams. **Table 2.3** shows the 3 focal depth configurations for the focused beams. The focal depth selections were driven by the clinical applications (vascular imaging for L11-4v, liver imaging for C5-2v, and

cardiac imaging for P4-2v). In all simulations, conditions were used such that a MI of 1.9 was achieved (maximum limit set by the Food and Drug Administration-FDA). The MI was calculated as the peak negative pressure in situ divided by the square root of the frequency. In both simulations and measurements, the MI was measured directly from the time domain waveform. The source pressure, fundamental component, and second harmonic produced by the arrays in PWI/DWI and focused mode were recorded for comparisons.

Table 2.3: Azimuthal focal depth configurations considered in focused ultrasound

Azimuthal focal depth configurations for focused ultrasound	**L11-4v**	**P4-2v**	**C5-2v**
Shallow focus	14 mm	40 mm	120 mm
Number of elements used in shallow focus	20	64	18
Moderate focus	22 mm	77 mm	77 mm
Number of elements used in moderate focus	26	64	36
Deep focus	30 mm	120 mm	120 mm
Number of elements used in deep focus	30	64	54

We used the following acoustic parameters for simulations in tissue: speed of sound $c_0 = 1540$ m/s, density $\rho_0 = 1000$ kg/m^3, nonlinearity coefficient $\beta = 5$, absorption coefficient $\alpha_0 =$ 0.3 dB/cm at 1 MHz. A quadratic relationship of absorption with frequency is assumed in the KZK predictions, despite the fact that tissue attenuation is typically linear with frequency. Thus, in our nonlinear simulations in tissue, the absorption at the higher harmonics is slightly overestimated. In linear simulations, we used $\beta = 0$. For simulations in water we used speed of sound $c_0 = 1500$ m/s, $\beta = 3.5$, and absorption coefficient $\alpha/f^2 = 25 \times 10^{-15}$ Np $\cdot$ s^2/m.

2.3 RESULTS

2.3.1 *Linear field simulation—comparison of KZK with Field II*

Contour plots of the linear field in tissue of the 3 diagnostic arrays (L11-4v, P4-2v, C5-2v) in the azimuthal and elevation plane produced with the KZK equation and Field II are shown in **Fig. 2.4**. Linear propagation would typically apply in low MI (MI<0.1) contrast applications. The color bar is in p/p_0. For L11-4v array, the width of the field of view was the same as the aperture width. For P4-2v array and C5-2v array, the width of the field of view was 10x and 5x the aperture width, respectively. The diverging nature of the field of P4-2v and C5-2v is appreciated in **Fig. 2.4**.

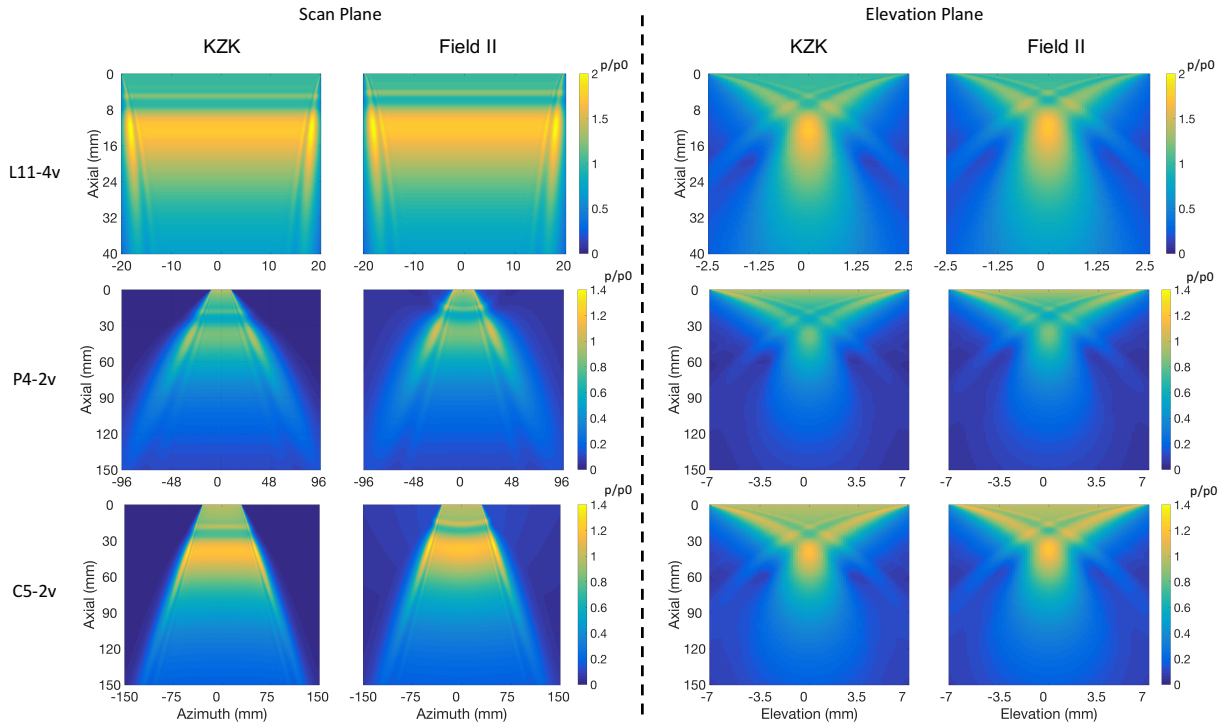

Fig. 2.4. Normalized pressure (with respect to source p_0) of the axial elevation and azimuthal planes calculated by by KZK and Field II for L11-4v, P4-2v, and C5-2v arrays in tissue.

Table 2.4: Mean relative difference between KZK and Field II in modeling 3 diagnostic arrays.

Azimuthal Plane	**L11-4v**	**P4-2v**	**C5-2v**	**Elevation Plane**	**L11-4v**	**P4-2v**	**C5-2v**
Mean relative difference (within 1x aperture)	3.8%	3.3%	4.5%	Relative difference (within 1x aperture)	4.5%	4.5%	4.4%
Mean relative difference (whole field)	3.8%	31%	41%	Relative difference (whole field)	4.5%	4.5%	4.4%

In qualitative comparisons, the KZK and Field II were in good agreement in terms of the pressure magnitude and overall beam structure, which is also reflected in the small difference shown in **Fig. 2.5** (a) and (b). The mean relative difference between KZK and Field II is shown in **Table 2.4**. When considering only an area extending to the edge of the aperture, the mean relative difference between KZK and Field II was less than 5% for both the azimuthal and the elevation plane. When considering a much wider area to accommodate the diverging nature of P4-2v and C5-2v, then the error was greater in the azimuthal plane and reached 40%, which is mainly attributed to the paraxial approximation of the KZK and it is discussed later in Section IV. However, as shown in **Fig. 2.5**

(c) and (d), the relative difference for most of the locations within the field of view were within 10%.

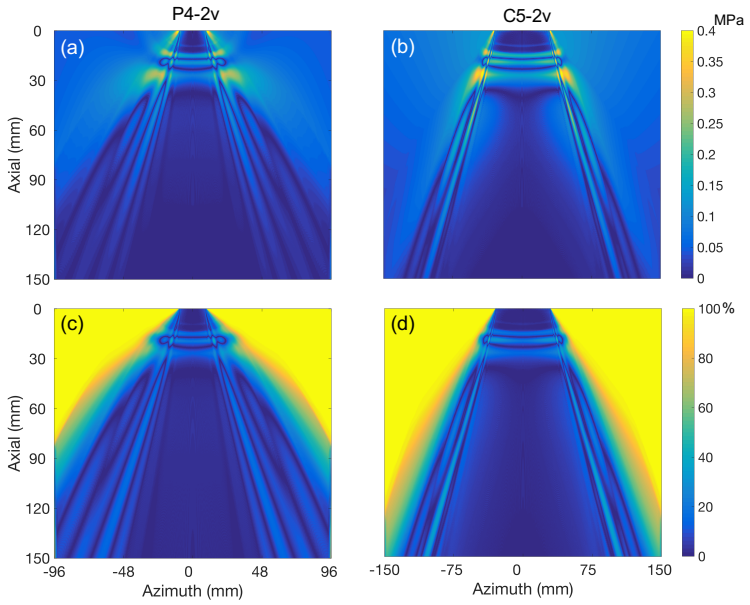

Fig. 2.5. Absolute pressure difference between Field II and KZK for linear simulation of P4-2v (a) and C5-2v (b) array. Relative % difference of the same arrays in (c) and (d).

2.3.2 *Spatial extent of linear field—bubble destruction*

The linear field simulations including tissue attenuation (produced with Field II) for 3 diagnostic arrays in plane/diverging wave mode and focused mode are shown in **Fig. 2.6** in logarithmic scale (dB) after normalizing with respect to the maximum value in each mode. For focused beams, where not all elements are used in each firing, the width of the contour was scaled appropriately in the figure. In the third column, the axial fields at the center of the array are shown (red for plane/diverging and blue for focused beams). For all 3 arrays, we see that in plane and diverging wave modes the pressure in the proximal half of the field is higher and in the distal half of the field lower than those of a focused beam and this will probably cause increased nearfield bubble destruction. Specifically, for the P4-2v, the maximum pressure is observed at the source, due to the highly divergent nature of the produced field.

The half amplitude (6 dB) axial field range for the 3 arrays in plane/diverging wave mode and focused mode are shown in **Fig. 2.6**. It is observed that the 6 dB range of the axial field is larger

in plane/diverging compared to focused beams by 3 to 20 mm, indicating the acoustic fields were more uniform when the arrays were in plane/diverging wave mode compare to focused beam. For all 3 arrays, it is noted that the elevation focus continues to have a strong effect and focuses the energy to that depth. However, most of the 6 dB range of plane/diverging fields were still within the nearfield. This is particularly obvious for P4-2v array and C5-2v array since the diverging wave quickly spreads out the energy.

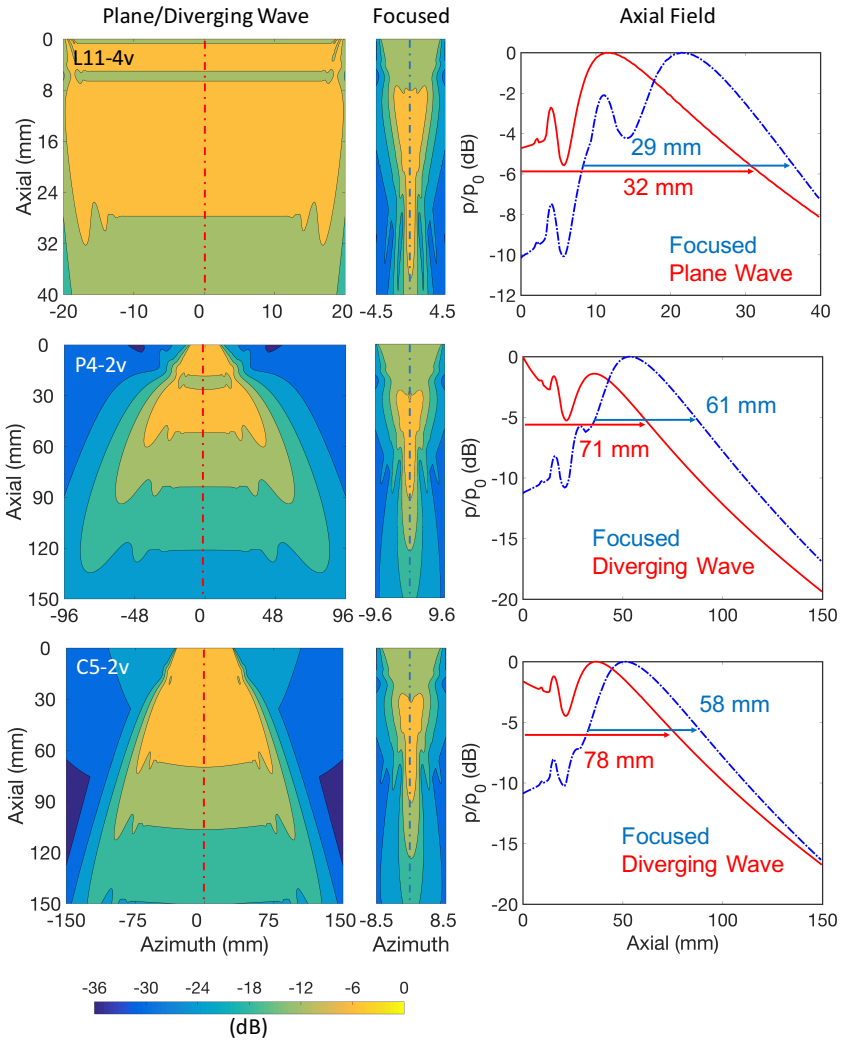

Fig. 2.6. Comparisons of the linear field produced by focused ultrasound (middle column) and PWI/DWI (left column) in tissue. Pressure is in dB normalized with respect to the maximum pressure in each field. The axial field of the plane/diverging (red/solid) and the focused beam (blue/dashed) is shown in the third column. The dashed lines in the contour plots indicate where the axial field in the third column is taken.

2.3.3 *Nonlinear field simulation—comparison of hydrophone measurements with KZK*

KZK simulations of the fundamental and second harmonic components of the acoustic field produced by the L11-4v array in plane wave mode are compared with hydrophone measurements in **Fig. 2.7**. It took 4 hours to collect the measurements of **Fig. 2.7**. The average pressure of the pressure contours of fundamental components, shown in **Fig. 2.7** (a) and (b) is 0.94 and 0.93 MPa, respectively. The average pressure of the pressure contours of second harmonic components, shown in **Fig. 2.7** (c) and (d) is 0.20 and 0.18 MPa, respectively.

There is a good qualitative agreement between the measurements and the simulations and this increases our confidence in the simulation results.

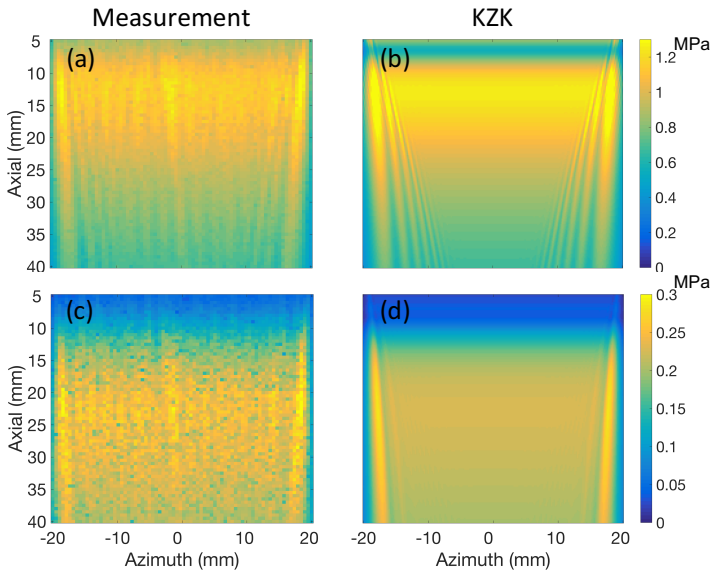

Fig. 2.7. Hydrophone measurements in water (left column) and KZK simulations (right column) of the fundamental (a)-(b) and second harmonic components (c)-(d), of the acoustic field produced by the L11-4v array in plane wave mode and KZK.

2.3.4 *Nonlinear field simulation— Harmonic generation in tissue*

Nonlinear field simulations for the 3 arrays in plane/diverging wave mode and focused mode, are shown in **Fig. 2.8**. The azimuthal focus that produced the largest second harmonic component in focused mode was selected. To achieve the same maximum MI in plane/diverging and focused beams, we used different source pressures in the simulations. The source pressure used for each

simulation is seen in the axial fields in **Fig. 2.9** and shown in **Table 2.5**. When operating at the same maximum MI (1.9), for L11-4v array, the peak second harmonic of the focused beam was 1.8 dB greater (**Fig. 2.9** (a)). For P4-2v, the peak second harmonic of the focused beam was 5.7 dB greater (**Fig. 2.9** (b)). For C5-2v, the peak second harmonic of the focused beam was 1.9 dB greater (**Fig. 2.9** (c)). It is noted that although the difference in the magnitude of peak second harmonic between plane/diverging wave and focused beam was moderate (less than 6 dB), the location of the maximum of the second harmonic was 10 and 15 mm closer to the source in plane and diverging wave, respectively, compared to ones in focused beam (**Table 2.5**).

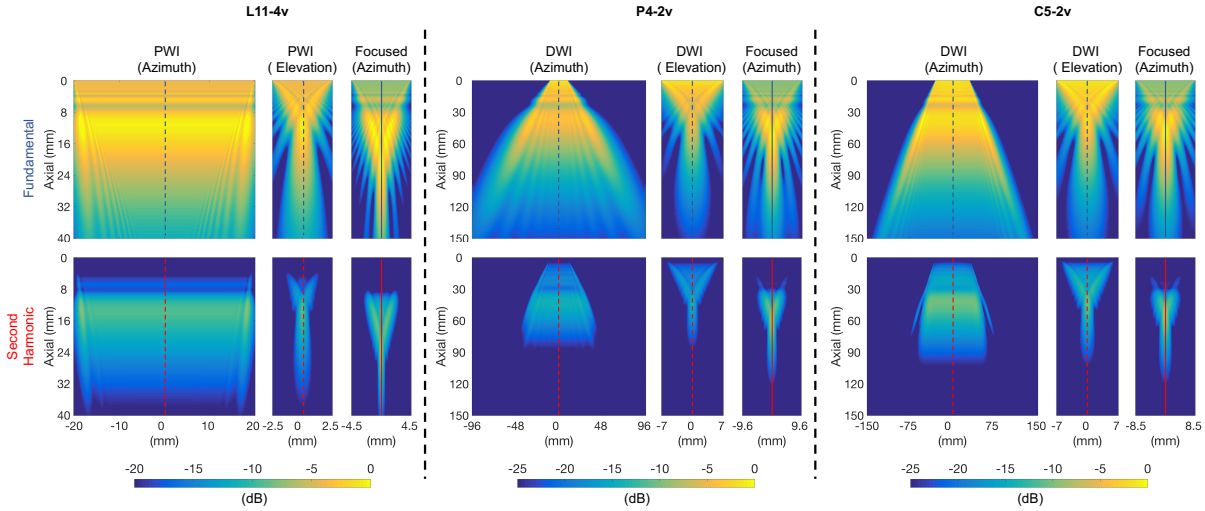

Fig. 2.8. Nonlinear field simulation of the L11-4v, P4-2v, and C5-2v array in plane/diverging wave mode and focused mode in tissue. The center of the aperture is shown with dashed lines for PWI/DWI and solid lines for focused beams.

Table 2.5: Source pressure and peak fundamental and second harmonic pressures for the cases considered in **Fig. 1.8**.

		Maximum depth (mm)	Source pressure (MPa)	Peak fundamental (MPa)	Peak second harmonic (Mpa)	Second harmonic at maximum depth (Mpa)	Location of peak second harmonic (mm)
L11-4v	Focused	40	1.77	4.22	1.79	0.63	23
	PWI		2.65	3.94	1.46	0.39	13
P4-2v	Focused	150	1.01	3.08	1.17	0.072	58
	DWI		2.69	2.69	0.61	0.027	43
C5-2v	Focused	150	1.04	3.13	1.17	0.076	54
	DWI		2.69	2.69	0.94	0.049	42

For more complete comparisons between plane/diverging and focused beams, we evaluated the effect of the azimuthal focus of focused beams on second harmonic generation. We considered 3 different azimuthal foci (shallow, moderate, and deep) and some of the results are shown in **Fig.**

2.9. For L11-4v, the second harmonic produced by PWI was larger than that of a focused beam with shallow azimuthal focus (**Fig. 2.9** (d)), everywhere along the axis. However, when deeper azimuthal foci are used, the second harmonic produced by focused beams was larger than that of PWI in the far field. Similarly, for the P4-2v and C5-2v arrays, although the second harmonic produced by DWI was generally larger than that of focused beam with shallow azimuthal focus throughout the depth, the second harmonic produced by focused beams with moderate or deep azimuthal focus was larger than that of DWI in the far field (**Fig. 2.9** (b)-(c) and (e)-(f)).

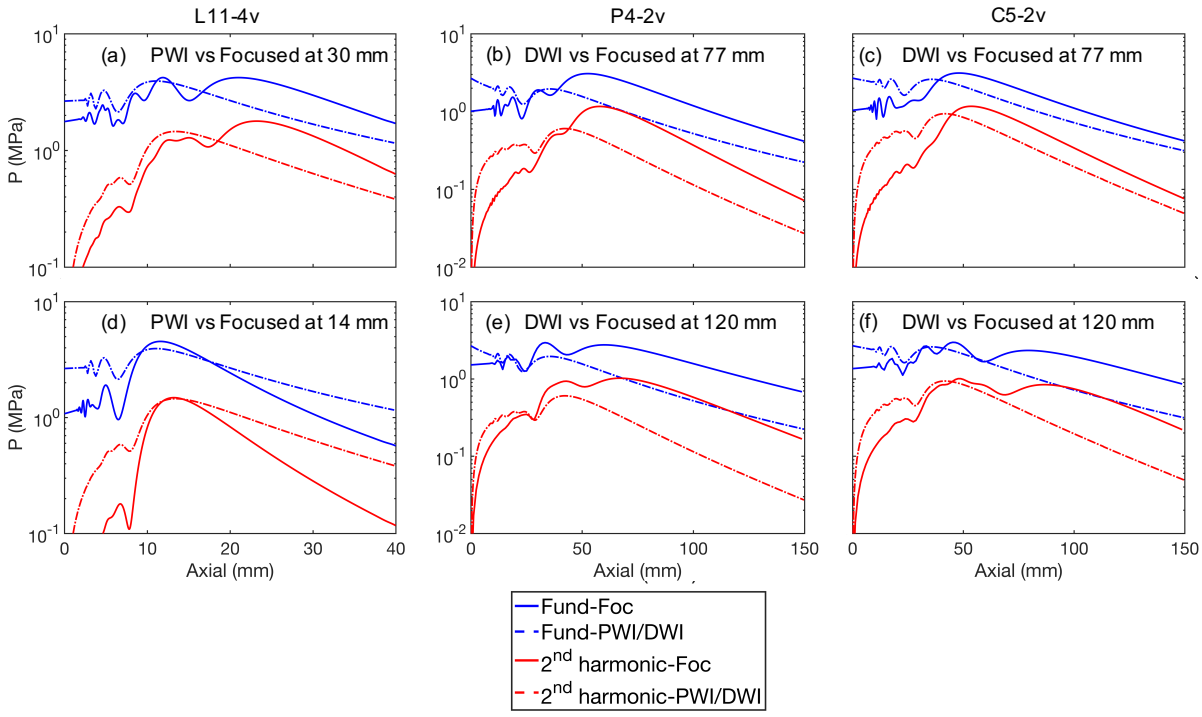

Fig. 2.9. Comparisons between the axial field produced by L11-4v, P4-2v, and C5-2v arrays in plane/diverging wave and focused mode at different azimuthal foci in tissue.

2.4 DISCUSSION

2.4.1 *Simulation and measurements*

The linear (low MI) and nonlinear (high MI) field of 3 diagnostic ultrasound arrays operating in plane and diverging wave mode was investigated in the present study. In contrast applications where MI<0.1, linear simulations like Field II are adequate for describing the transmitted field. In THI applications (without microbubbles), typically MI>1.0, a nonlinear simulation like the KZK is necessary. For the numerical solution, the step size in time (τ) is chosen solely on the degree of

nonlinearity. When the waveform distorts due to nonlinear propagation, small enough sampling time is required to capture the faster rise times of the pulse. In present study, we used 20 points per cycle for linear and 60 for nonlinear propagation. In addition, the step size in the transverse direction (x and y) is very important for the accuracy of the calculation. The conditions of validity of KZK require that $ka>>1$ [10] which reduces to $a>\lambda$. Since the code solves a non-dimensional form of the KZK equation, where all parameters have been grouped in the focusing gain in the respective dimensions, we discretized the aperture according to the value of the focusing gain. For the sources in present study, 40-500 points per half aperture dimension were used for discretization. However, finer spatial discretization greatly increases computational time. The KZK field simulation for the L11-4v array took around 4-12 hours (depending on field of view and nonlinearity) to finish. However, the simulation of P4-2v and C5-2v arrays, since not only a smaller step size in x was required to capture the curvature of the wave fronts, but a pulse with a longer tail was also necessary to correctly model the diffraction in regions far away from the main axis, the simulation took up to 48 hours to finish. In addition, the step size (in the propagation direction) for the finite difference schemes (IBFD and CNFD) also affected computational time. On the other hand, since Field II utilizes superposition of point sources to model the field, the computational time of Field II was around 1-2 hours, much faster than KZK. All simulations were performed on a workstation with 4.2 GHz Intel(R) Core(TM) i7-7700K and 32 GB of RAM running the Windows 10 operating system.

We first validated the KZK equation on its ability to accurately calculate the diffraction and absorption effects (without considering nonlinear effects) by comparing it with Field II. The KZK equation was in good agreement with Field II in an area in front of the source and extending to the edge of the aperture (mean relative differences less than 5%). However, the mean relative difference between KZK and Field II was up to 41% over the whole field which included areas that were at angles greater than 60°. These differences between the KZK and Field II are mainly due to the paraxial approximation in the calculation of diffraction that is used in the KZK [11]. As it is clearly demonstrated in **Fig. 2.5**, the large discrepancies took place away from the axis (angles larger than 60°). According to previous studies [10, 12], the range of validity of KZK is within a few source radii and up to 30° around the axis in the farfield due to paraxial approximation. However, those requirements were for spherically focused circular transducers and here we are

dealing with rectangular arrays with different foci in elevation and azimuthal directions. The elevation size of our aperture is short (only 2.5 to 7 mm in the case of the linear and curve linear arrays). In the azimuthal direction, we do not have a focus (plane or diverging geometry) and thus the paraxial limitations of [10, 12] may not directly apply here. It is evident from **Fig. 2.4** where we compared KZK and Field II that the overall agreement is very good even close to the source and at angles greater than 30°.

We've also observed a good qualitative agreement between our simulations and hydrophone measurements in water (**Fig. 2.7**). This validates our method of placing the azimuthal focus very far from the source to remove focusing in the azimuthal direction. More importantly, the second harmonic measured in water was in good agreement with our predictions. We have observed a slightly higher second harmonic in the measurements compared to the simulations and we believe that this may be due to a small amount of second harmonic produced by the Verasonics system and transmitted directly by the array. The pressure at the edge side lopes (angled lines around +/- 20 mm in **Fig. 2.7**) was higher in the simulation than the measurement, possibly due to a small misalignment error between the hydrophone and the array. In addition, the measurement seems to have more striations than the simulation, which may be attributed to the measurement discretization. To the best of our knowledge, this is the first comparison between acoustic field measurements and KZK simulations for plane wave diagnostic ultrasound arrays. This opens the door to further plane/diverging beam investigations evaluating the nonlinear field of diagnostic arrays operating in these modes.

2.4.2 *Observations and implications for imaging*

Fig. 2.6 illustrates the shape of the axial field, when using plane/diverging waves, is dominated by the elevation focus. The main difference between plan/diverging and focused beams is the required higher source pressure in order to reach equivalent pressure amplitudes to generate nonlinear microbubble responses equivalent to focused beams (see **Fig. 2.6**). In addition, the depth of field (6 dB axial range) of plane/diverging beams is larger than that of the focused beams but only proximal to the array. However, the focused beams deliver a higher acoustic pressure in the farfield due to electronic focusing. In order to increase farfield penetration of plane/diverging beams, a higher source pressure may be used which may cause increased bubble destruction. In the cases

considered in **Fig. 2.6**, the C5-2v array with a divergent beam (where tissue attenuation was included) does not seem to suffer in any way when it comes to the delivered acoustic field and in relation to bubble destruction when compared to focused beams. Both the depth of field and the farfield pressure are comparable to the equivalent focused beam. Finally, it is also possible that plane/diverging beams may result in increased bubble destruction due to not only insonifying a much larger area of bubbles with every firing but also due to the very high frame rates that are possible in ultrafast contrast imaging. Moreover, a larger 6 dB range and wider field in PWI/DWI may explain why a previous study observed increased bubble destruction in DWI compared to focused beam as MI increased [13]. Although PWI/DWI suffers from a lower transmitted amplitude past the elevation focus and resulting penetration, these differences can be compensated by trading-off frame rate through additional acquisitions, as long as the microbubbles are still generating nonlinear signals.

In the nonlinear simulations of propagation in attenuative tissue (**Fig. 2.8** and **Fig. 2.9**), we used source pressures such that the maximum MI in the field was 1.9, in order to consider the highest possible amplitude for second harmonic generation. As it is shown in **Table 2.5**, PWI/DWI required a higher source pressure to reach the same MI as focused beams, and may potentially lead to higher skin temperature elevation due to higher scan-head surface temperature (SST). When the same source pressure is assumed, the focused beam would of course have higher MI than PWI/DWI due to its azimuthal focus. Since SST is heavily related to the source pressure of the probe and the pulse repetition frequency, we expect PWI/DWI to have similar SST to conventional spectral Doppler techniques. However, since PWI/DWI insonify the field with full aperture, the spatial-peak temporal-average intensity (ISPTA) should be different between PWI/DWI and focused beams. Recent developments in shear-wave elastography (SWE) have led to improvements in heat removal and deposition, that have addressed scan-head heating which may be relevant to ultrafast THI. In real imaging applications, PWI/DWI may never achieve MI 1.9 due to the limit of scan-head surface temperature. However, our objective was to investigate the conditions that would result in the highest harmonic generation in tissue for all types of array configuration, while still the limiting condition is the required by the FDA MI≤1.9.

The second harmonic beam is always narrower than the corresponding fundamental due to the fact that it is produced preferentially more in the areas of larger amplitude [14]. This effect is observed in all simulations in **Fig. 2.8** and is even more pronounced with diverging sound beams. Thus for ultrafast THI, using a large divergence angle may have limited improvement on the field of view. Another interesting point about diverging beams is that at deeper ranges (at 15 cm) the produced second harmonic pressure in DWI is considerably lower (4 and 9 dB for C5-2V and P4-2v array, respectively) than the equivalent focused beam pressure (**Fig. 2.9** (c) and (b)). Moreover, this difference further increased to 13 and 16 dB as deeper azimuthal focus was used for C5-2v and P4-2v array in focused mode, respectively (**Fig. 2.9** (f) and (e)). This implies that it may be more challenging to perform ultrafast THI with DWI as also mentioned by others [15]. However, the moderate difference of the second harmonic between PWI/DWI and focused beam elsewhere (besides deep locations) suggests it is still feasible to combine PWI/DWI and THI for ultrafast THI. In addition, the advantage of THI in removing clutter and reverberation artifacts both in the nearfield and farfield, may necessitate the use of ultrafast THI despite its lower second harmonic. Previous work has shown that ultrafast THI has better SNR with reduced clutter level up to 13.8 dB compared to conventional ultrafast imaging [18]. Reducing the sector width (degree of divergence) will increase penetration at the expense of a narrower field of view. Since the elevation focus still has a strong effect on the overall field for PWI/DWI despite the unfocused or defocused nature of the beam in the azimuthal plane, to increase second harmonic deeper we could design 1D arrays with deeper elevation focus. A more flexible approach would be the use of 1.X and 2D arrays enabling a combination of azimuthal and elevational transmit beam designs.

A potential way to increase SNR and CNR of ultrafast THI in deeper regions may be to utilize specifically designed pulsing schemes with coherent compounding techniques for ultrafast THI such as delay-encoded harmonic imaging demonstrated in the literature, which has shown a maximal SNR improvement of 7.9 dB compares to regular compounded harmonic images [17]. Or more simply as noted for contrast above, additional transmits are acquired to improve SNR at a rate of sqrt(N), where N is the number of transmits averaged for each displayed frame.

2.5 CONCLUSION

We have presented a numerical model based on the KZK equation for the calculation of the nonlinear field of 3 diagnostic ultrasound arrays, L11-4v, P4-2v, and C5-2v, when operated in PWI/DWI for ultrafast imaging. The model solves the KZK equation in the time domain and it is ideal for imaging applications. We have validated our numerical model with acoustic field measurements of the fundamental and second harmonic component in water and good agreement was found. With linear field simulations, we investigated the spatial extent of the imaging arrays when operated in PWI/DWI. In PWI/DWI the depth of field (6 dB down from max) is greater than in focused beams but only proximal to the source and hence some increased bubble destruction and limited penetration in contrast imaging is expected. With nonlinear field simulations, we evaluated second harmonic generation in tissue and the feasibility of THI in PWI/DWI. The second harmonic generated in tissue in PWI/DWI was found to be within 2-16 dB than that of focused beams, and hence ultrafast THI is possible. Our work also provides useful insight in understanding the depth of field of ultrafast contrast imaging and ultrafast THI, which has not been considered in previous studies. In future research, we will implement and evaluate THI in PWI/DWI and investigate how to increase penetration.

2.6 REFERENCES

[1] T. L. Szabo, *Diagnostic ultrasound imaging: inside out*. Academic Press, 2004.

[2] P. R. Hoskins, K. Martin, and A. Thrush, *Diagnostic ultrasound: physics and equipment*. Cambridge University Press, 2010.

[3] M. Tanter and M. Fink, "Ultrafast imaging in biomedical ultrasound," *IEEE transactions on ultrasonics, ferroelectrics, and frequency control,* vol. 61, no. 1, pp. 102-119, 2014.

[4] M. Dighe and M. Bruce, "Elastography of diffuse liver diseases," in *Seminars in roentgenology*, 2016, vol. 51, no. 4, pp. 358-366: Elsevier.

[5] M. Bruce, A. Hannah, C. Tremblay-Darveau, and P. Burns, "High frame-rate visualization of blood flow with ultrasound contrast agents," *The Journal of the Acoustical Society of America,* vol. 140, no. 4, pp. 3028-3028, 2016.

[6] E. Macé, G. Montaldo, I. Cohen, M. Baulac, M. Fink, and M. Tanter, "Functional ultrasound imaging of the brain," *Nature methods,* vol. 8, no. 8, pp. 662-664, 2011.

[7] B. Lokesh and A. K. Thittai, "Spatial resolution improvement in Plane Wave Imaging using adaptive Sign Coherence Factor weighting," in *Ultrasonics Symposium (IUS), 2016 IEEE International*, 2016, pp. 1-4: IEEE.

[8] B. Denarie *et al.*, "Coherent plane wave compounding for very high frame rate ultrasonography of rapidly moving targets," *IEEE transactions on medical imaging,* vol. 32, no. 7, pp. 1265-1276, 2013.

[9] G. Montaldo, M. Tanter, J. Bercoff, N. Benech, and M. Fink, "Coherent plane-wave compounding for very high frame rate ultrasonography and transient elastography," *IEEE transactions on ultrasonics, ferroelectrics, and frequency control,* vol. 56, no. 3, pp. 489-506, 2009.

[10] J. Jensen, M. B. Stuart, and J. A. Jensen, "Optimized plane wave imaging for fast and high-quality ultrasound imaging," *IEEE transactions on ultrasonics, ferroelectrics, and frequency control,* vol. 63, no. 11, pp. 1922-1934, 2016.

[11] E. Tiran *et al.*, "Multiplane wave imaging increases signal-to-noise ratio in ultrafast ultrasound imaging," *Physics in medicine and biology,* vol. 60, no. 21, p. 8549, 2015.

[12] M. A. Averkiou, "Tissue harmonic ultrasonic imaging," *Comptes Rendus de l'Académie des Sciences-Series IV-Physics,* vol. 2, no. 8, pp. 1139-1151, 2001.

[13] P. Jiang, Z. Mao, and J. Lazenby, "A new tissue harmonic imaging scheme with better fundamental frequency cancellation and higher signal-to-noise ratio," in *Ultrasonics Symposium, 1998. Proceedings., 1998 IEEE*, 1998, vol. 2, pp. 1589-1594: IEEE.

[14] T. Whittingham, "Tissue harmonic imaging," *European radiology,* vol. 9, no. 3, p. S323, 1999.

[15] M. Cikes, L. Tong, G. R. Sutherland, and J. D'hooge, "Ultrafast cardiac ultrasound imaging: technical principles, applications, and clinical benefits," *JACC: Cardiovascular Imaging,* vol. 7, no. 8, pp. 812-823, 2014.

[16] W. Guo, Y. Wang, and J. Yu, "Ultrasound Harmonic Enhanced Imaging Based on the Eigen Decomposition," *Journal of Medical Imaging and Health Informatics,* vol. 6, no. 5, pp. 1276-1281, 2016.

[17] P. Gong, P. Song, and S. Chen, "Delay-encoded harmonic imaging (DE-HI) in multiplane-wave compounding," *IEEE transactions on medical imaging,* vol. 36, no. 4, pp. 952-959, 2017.

[18] M. Correia, J. Provost, S. Chatelin, O. Villemain, M. Tanter, and M. Pernot, "Ultrafast harmonic coherent compound (UHCC) imaging for high frame rate echocardiography and shear-wave elastography," *IEEE transactions on ultrasonics, ferroelectrics, and frequency control,* vol. 63, no. 3, pp. 420-431, 2016.

[19] L. Tong, H. Gao, H. F. Choi, and J. D'hooge, "Comparison of conventional parallel beamforming with plane wave and diverging wave imaging for cardiac applications: A simulation study," *IEEE transactions on ultrasonics, ferroelectrics, and frequency control,* vol. 59, no. 8, pp. 1654-1663, 2012.

[20] C. P. Keravnou, I. De Cock, I. Lentacker, M.-L. Izamis, and M. A. Averkiou, "Microvascular Injury and Perfusion Changes Induced by Ultrasound and Microbubbles in a Machine-Perfused Pig Liver," *Ultrasound in Medicine and Biology,* vol. 42, no. 11, pp. 2676-2686, 2016.

[21] E. Fröhlich, R. Muller, X.-W. Cui, D. Schreiber-Dietrich, and C. F. Dietrich, "Dynamic Contrast-Enhanced Ultrasound for Quantification of Tissue Perfusion," *Journal of Ultrasound in Medicine,* vol. 34, no. 2, pp. 179-196, 2015.

[22] C. Errico *et al.*, "Ultrafast ultrasound localization microscopy for deep super-resolution vascular imaging," *Nature,* vol. 527, no. 7579, p. 499, 2015.

[23] M. Bruce, A. Hannah, Z. Khaing, C. Tremblay-Darveau, C. Hofstetter, and P. Burns, "Contrast enhanced ultrasound (CEUS) imaging of rat spinal cord injury," in *Ultrasonics Symposium (IUS), 2017 IEEE International*, 2017, pp. 1-1: IEEE.

[24] M. Toulemonde, R. J. Eckersley, and M.-X. Tang, "High frame rate contrast enhanced echocardiography: Microbubbles stability and contrast evaluation," in *Ultrasonics Symposium (IUS), 2017 IEEE International*, 2017, pp. 1-4: IEEE.
[25] M. A. Averkiou, Y. S. Lee, and M. F. Hamilton, "Self-demodulation of amplitude-and frequency-modulated pulses in a thermoviscous fluid," *The Journal of the Acoustical Society of America,* vol. 94, no. 5, pp. 2876-2883, 1993.
[26] M. A. Averkiou and M. F. Hamilton, "Measurements of harmonic generation in a focused finite-amplitude sound beam," *The Journal of the Acoustical Society of America,* vol. 98, no. 6, pp. 3439-3442, 1995.
[27] V. Kuznetsov, "Equation of nonlinear acoustics," *Sov. Phys. Acoust.,* vol. 16, no. 4, pp. 467-470, 1971.
[28] E. Zabolotskaya, "Quasiplane waves in the nonlinear acoustics of confined beams," *Sov. Phys. Acoust.,* vol. 15, pp. 35-40, 1969.
[29] S. Nachef, D. Cathignol, J. N. Tjo/tta, A. M. Berg, and S. Tjo/tta, "Investigation of a high intensity sound beam from a plane transducer. Experimental and theoretical results," *The Journal of the Acoustical Society of America,* vol. 98, no. 4, pp. 2303-2323, 1995.
[30] S. I. Aanonsen, T. Barkve, J. N. Tjo/tta, and S. Tjo/tta, "Distortion and harmonic generation in the nearfield of a finite amplitude sound beam," *The Journal of the Acoustical Society of America,* vol. 75, no. 3, pp. 749-768, 1984.
[31] Y. S. Lee and M. F. Hamilton, "Time-domain modeling of pulsed finite-amplitude sound beams," *The Journal of the Acoustical Society of America,* vol. 97, no. 2, pp. 906-917, 1995.
[32] A. C. Baker, A. M. Berg, A. Sahin, and J. N. Tjo/tta, "The nonlinear pressure field of plane, rectangular apertures: Experimental and theoretical results," *The Journal of the Acoustical Society of America,* vol. 97, no. 6, pp. 3510-3517, 1995.
[33] V. Khokhlova, A. Ponomarev, M. Averkiou, and L. Crum, "Nonlinear pulsed ultrasound beams radiated by rectangular focused diagnostic transducers," *Acoustical Physics,* vol. 52, no. 4, pp. 481-489, 2006.
[34] R. Thurston, A. D. Pierce, and E. P. Papadakis, *Reference for Modern Instrumentation, Techniques, and Technology: Ultrasonic Instruments and Devices I: Ultrasonic Instruments and Devices I*. Academic Press, 1998.
[35] J. A. Jensen, *Estimation of blood velocities using ultrasound: a signal processing approach*. Cambridge University Press, 1996.
[36] M. A. Averkiou and M. F. Hamilton, "Nonlinear distortion of short pulses radiated by plane and focused circular pistons," *The Journal of the Acoustical Society of America,* vol. 102, no. 5, pp. 2539-2548, 1997.
[37] J. A. Jensen and N. B. Svendsen, "Calculation of pressure fields from arbitrarily shaped, apodized, and excited ultrasound transducers," *IEEE transactions on ultrasonics, ferroelectrics, and frequency control,* vol. 39, no. 2, pp. 262-267, 1992.
[38] J. A. Jensen, "Field: A program for simulating ultrasound systems," in *10TH NORDICBALTIC CONFERENCE ON BIOMEDICAL IMAGING, VOL. 4, SUPPLEMENT 1, PART 1: 351--353*, 1996: Citeseer.
[39] J. N. Tjo/tta, S. Tjo/tta, and E. H. Vefring, "Effects of focusing on the nonlinear interaction between two collinear finite amplitude sound beams," *The Journal of the Acoustical Society of America,* vol. 89, no. 3, pp. 1017-1027, 1991.
[40] S. Qiao, E. Jackson, C. C. Coussios, and R. O. Cleveland, "Simulation of nonlinear propagation of biomedical ultrasound using pzflex and the Khokhlov-Zabolotskaya-

Kuznetsov Texas code," *The Journal of the Acoustical Society of America,* vol. 140, no. 3, pp. 2039-2046, 2016.

[41] J. Naze Tjo/tta, S. Tjo/tta, and E. H. Vefring, "Propagation and interaction of two collinear finite amplitude sound beams," *The Journal of the Acoustical Society of America,* vol. 88, no. 6, pp. 2859-2870, 1990.

[42]. M. A. Averkiou, D. N. Roundhill, and J. E. Powers, "A new imaging technique based on the nonlinear properties of tissues," in *Ultrasonics Symposium*, 1997, vol. 2, pp. 1561-1566: INSTITUTE OF ELECTRICAL & ELECTRONICS ENGINEERS INC.

Chapter 3. HARMONIC GENERATION IN TISSUE WITH A 2D MATRIX ARRAY FOR 4D CARDIAC THI

Abstract

Combining 4D echocardiography and tissue harmonic imaging (THI) may improve the quality of cardiac imaging and consequently the diagnosis of various heart diseases. In order to produce acceptable volume rates in 4D echocardiography, beamforming approaches that produce broader beams must be considered. However, to the best of our knowledge, there is no in-depth investigation of harmonic generation in tissue with a matrix array and while utilizing broad beam approaches such as plane wave imaging (PWI) and diverging wave imaging (DWI). In the present study we evaluated various beamforming approaches for 4D cardiac THI with a matrix array with a numerical model of nonlinear propagation based on the KZK equation. We considered the spatial extent and amplitude of the 2nd harmonic component in tissue together with the resulting volume rate of every beamforming approach used. We found that conventional focused beamforming produced the highest peak 2nd harmonic component in tissue (0.59 MPa) and the lowest volume rate (1 Hz). On the other hand, the peak 2nd harmonic component produced by PWI was found to be 9-20 dB lower than that produced by conventional focused beamforming approaches, but despite this difference it may still be feasible to use PWI for 4D cardiac THI. The volume rates for the beamforming approaches we have considered for 4D cardiac THI are in the range 1-8 Hz with conventional focused beamforming (depending on the focal depths), 44 Hz with PWI, and 444 Hz with DWI.

Manuscript in preparation

3.1 INTRODUCTION

Cardiovascular disease (CVD) is the leading cause of death globally, accounting for more than 17.9 million deaths worldwide per year in 2015, a number that is expected to grow to more than 23.6 million by 2030 [1]. Accurate diagnosis of CVD at its earlier stages is the key to better prognosis. However, accurate diagnosis may be difficult as patients often show different early signs and symptoms. Echocardiography reveals details of various cardiac structures and physiology, and has an immense impact on the diagnostic ability and the understanding of a variety of disease states. Echocardiography is the procedure of choice for detecting problems such as pericardial effusion, intracardiac masses, valvular and congenital heart disease, and primary myocardial disease [2].

Compared to conventional echocardiography, 4D echocardiography enables physicians to examine 3D cardiac structures in real-time and in a more intuitive manner. One of the major proven advantages of 4D echocardiography with matrix arrays is the improved accuracy of the echocardiographic evaluation of cardiac chamber volumes [3] as it eliminates the need for geometric modeling and the errors caused by foreshortened views [4]. Matrix arrays have rectangle elements in both the azimuth and elevation directions, allowing flexible beamforming strategies towards any direction [5]. However, current commercial 4D ultrasound systems typically rely on conventional beamforming techniques (line-by-line volume imaging by transmitting multiple tightly-focused beams along the azimuthal and elevation directions) to sample the volume and are thus limited to a few volumes per second. Therefore, 4D echocardiography with conventional beamforming lacks the temporal resolution and might not be able to adequately resolve or detect subtle changes in cardiac motion and deformation pattern as well as complex and transient myocardial events [6, 7].

Parallel receive beamforming (also referred to as “multiline”) is a widely used technique to improve the volume rate as it reconstructs multiple neighboring image lines simultaneously for each transmit beam [8, 9]. A broadened transmit beam is required for parallel receive beamforming to ensure adequate coverage of the region per transmit beam in order to form multiple receive lines. Recent developments in ultrafast imaging have improved the temporal resolution of 4D echocardiography to over 4000 volumes per second [10, 11] by sampling the volume with a single

plane or diverging wave imaging approach(PWI/DWI) followed by parallel receive beamforming. However, PWI/DWI may degrade image quality: first, the lateral resolution is significantly reduced due to the broad beam transmitted in PWI/DWI, although the compromise in resolution can be partly recovered by coherent compounding [12, 13]. Secondly, without focusing, the signal-to-noise ratio (SNR) is reduced especially in deeper regions of the image [14]. Moreover, phase aberrations caused by tissue inhomogeneity, and grating lobe and main lobe artifacts induced by steering plane or diverging beams may further compromise the contrast of the image [15, 16].

The development of tissue harmonic imaging (THI) [17] has dramatically improved the image quality of echocardiography on CVD patients, who are often overweight and difficult to image due to image artifacts. THI improves image quality and reduces image artifacts from phase aberrations and reverberations [18], which are often encountered in echocardiography. As ultrasound waves propagate in tissue, harmonic components are gradually generated due to nonlinear propagation. Bandpass filtering of the radio frequency (RF) signals can isolate the harmonic in the tissue echoes in early versions of THI [17], while pulse inversion (PI) is more common in more recent implementations [18]. Since nonlinear propagation is pressure amplitude dependent, artifacts from side lobes, grating lobes, and multiple scattering that have weaker pressure amplitude are reduced in THI [19]. Moreover, since nonlinear components are gradually generated in tissue, body wall reverberation artifacts are reduced in THI [18, 19].

In order to produce acceptable volume rates in 4D echocardiography broader beams and/or PWI and DWI approaches must be used. However, when such beams and approaches are used, the amount of second harmonic that is produced is considerably lower since the amplitude of the main beam is also lower. Despite this, some early reports suggest that it is possible to still have image improvements in 4D THI [20, 21]. However, to the best of our knowledge, there is no in-depth investigation of harmonic generation in tissue with a matrix array and while utilizing broad beam approaches. Beamforming considerations such as beam shape, the methodology of sampling the volume with ultrasound beams, and the magnitude of the 2nd harmonic component generated in tissue greatly affect the image quality and temporal resolution of 4D cardiac THI.

The Khokhlov-Zabolotskaya-Kuznetsov (KZK) equation has been used to study the nonlinear propagation of pulsed finite amplitude sound beams in thermoviscous fluids [22, 23]. The equation describes the combined effects of diffraction, thermoviscous absorption, and nonlinearity [24, 25]. In our previous work, we have expanded the KZK model to include rectangular apertures with azimuthal and elevation focusing and thus be able to model plane and diverging beams [21].

The aim of the present study was to investigate harmonic generation in tissue with a matrix array utilizing different beamforming approaches and under realistic conditions that take into consideration the matrix array specifications, the volume rate, and safety guidelines.

3.2 Materials and Methods

3.2.1 *Modeling of the Acoustic Field of a Matrix Array*

3.2.1.1 *Linear simulation*

The acoustic field produced by a Philips X5-1 matrix array (Philips Healthcare, Bothell, WA, USA) for cardiac imaging was modeled in the present study. The physical dimension of the X5-1 array is 23 mm × 18 mm (azimuthal × elevation). Two cycle pulses at 1.67 MHz were used in the simulations. The imaging depth was 15 cm and the field of view is 75° × 75° (azimuthal × elevation), consistent with a typical depth of view in cardiac imaging. Since the generation of harmonics is dependent on the amplitude of the fundamental component, we first evaluated the spatial extent and magnitude of the fundamental component of the field with respect to the different azimuthal/elevation foci (AF/EF). In this first part, we used Field II, a transducer field simulation based on the Rayleigh integral [26, 27], to document the spatial characteristics of the beamforming approaches considered. The peak positive pressure and the average -6dB beamwidth of the lateral fields on azimuthal and elevation plane were calculated for various azimuthal and elevation foci (75 mm - 250 mm in increments of 5 mm). For these simulations we used 200 MHz sampling frequency, 25 sub-division in element height, and 25 sub-division in element width.

3.2.1.2 *Nonlinear simulation-KZK*

We next evaluated the spatial extent and magnitude of the produced 2nd harmonic component for different beamforming approaches with KZK simulations. The parameters used for KZK

simulations are shown in **Table 3.1**, where $\sigma = z/d_x$, z is the propagation axis of the sound beam, and d_x is the azimuthal focus of the array. More details of the numerical model were presented previously [21]. Four beamforming approaches with different azimuthal-elevation foci combinations were considered: (1) 75-75 mm, (2) 250-75 mm, (3) 250-250 mm, and (4) unfocused ("plane wave") in both planes. A schematic of the beamforming approaches is shown in **Fig. 3.1**. For producing an unfocused beam for PWI with our existing numerical model, we place the focus at infinity (10^4 m) as shown in **Fig. 3.1**. We used different source pressures for each beamforming approach such that either the transducer surface temperature reached 43°C in air, or one of MI, I_{sppa}, or I_{spta} reached the maximum limit under the current safety guidelines. The details of the temperature measurements are described in the later section. To account for ultrasonic attenuation in the tissue, an absorption coefficient of 0.3 dB/cm at 1 MHz was assumed for both Field II and KZK simulations. The parameters used in the simulation for tissue are speed of sound $c = 1540$ m/s, density $\rho = 1000$ kg/m^3, and nonlinearity coefficient $\beta = 5$.

Table 3.1: Parameters used in the KZK simulation.

Parameters for numerical simulations	Focused ultrasound	PWI	DWI
Focus	75 or 250 mm	10^4 m	-12.5 mm
Azimuthal steps per aperture	100	100	500
Elevation steps per aperture	100	100	500
Step size of Implicit Backward Finite Difference method ($\Delta\sigma$)	5×10^{-4}	1×10^{-9}	5×10^{-4}
Step size of Crank-Nicolson Finite Difference method ($\Delta\sigma$)	2×10^{-3}	4×10^{-9}	2×10^{-3}

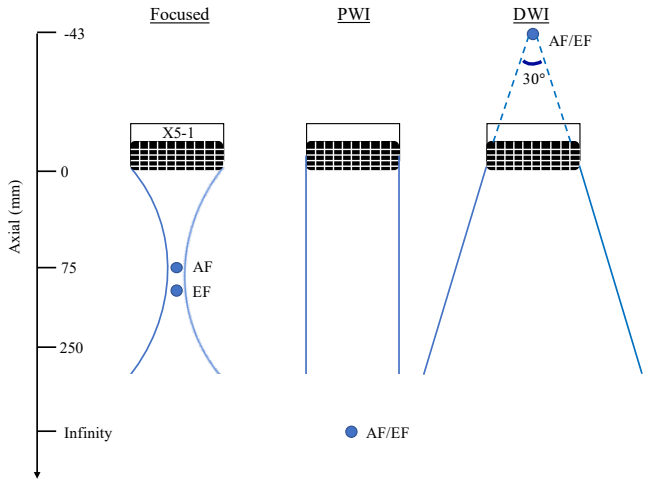

Fig. 3.1. Schematic of how conventional focused beamforming, PWI, and DWI were modeled in the numerical solution; Conventional focused beamforming has an azimuthal and an elevation focus, PWI has one focus at infinity, and DWI has a virtual (negative) focus behind the array.

3.2.2 *Volume rate of 4D cardiac THI*

3.2.2.1 *Approximating steered beams with rotated beams*

With the parallel receive beamforming technique, multiple neighboring image lines within the -6dB beamwidth of the acoustic field are reconstructed simultaneously [9]. To obtain a volumetric scan, beam steering in the azimuthal and elevation dimensions is required. However, the range of validity of KZK simulation is within a few source radii and up to 30° around the axis in the farfield due to paraxial approximation used in KZK [28, 29]. In the present study, we assumed that the steered beam is similar to the unsteered beam (0°) in terms of pressure. A steered beam can then be approximated by rotating the unsteered beam to a certain angle such that $P(x_r, y_r, z_r) = P(x_u, y_u, z_u)$. The transformations between the coordinates of the rotated and unsteered beam are given by [30]:

$$\begin{bmatrix} x_r \\ y_r \\ z_r \end{bmatrix} = \begin{bmatrix} \cos\psi_r & 0 & -\sin\psi_r \\ \sin\theta_r \sin\psi_r & \cos\theta_r & \sin\theta_r \cos\psi_r \\ \cos\theta_r \sin\psi_r & -\sin\theta_r & \cos\theta_r \cos\psi_r \end{bmatrix} \begin{bmatrix} x_u \\ y_u \\ z_u \end{bmatrix}, \tag{3.1}$$

where x_r, y_r and z_r are the coordinates of the rotated beam after transformation in azimuthal, elevation, and propagation direction, respectively. x_u, y_u and z_u are the coordinates of the

unsteered beam and ψ_r and θ_r are the direction of the rotated beam in azimuthal and elevation plane with respect to the propagation axis, respectively.

3.2.2.2 *Estimating the volume rate of different beamforming approaches*

Conventional 2D Cardiac imaging typically uses 64 transmit beams to sample the azimuthal imaging plane. In this paper, we used this 64-beam density as a point of reference. More specifically, for each of the beamforming approach considered, we estimated the minimum number of transmit beams in the azimuthal and elevation directions which provided an area coverage by the overlapping -6dB beamwidth equivalent to at least 90% of the area coverage provided by that of 64 transmit beams focused at 75mm in the azimuthal and elevational directions, respectively. The overlapping area of the -6dB beamwidths (yellow area pointed by the red arrow in **Fig. 3.2**) was recorded as the number of transmit beams increased from 36 to 64 beams. **Fig. 3.2** provides a graphical illustration of the approach explained above when considering the conventional beamforming approach with AF/EF=75mm. Further details can be found in **Section 3.3.4** and **Fig. 3.7**. The volume rate (Hz) of a beamforming approach was then calculated by dividing the pulse repetition frequency (PRF; 4000 Hz in this study) by the transmit pattern.

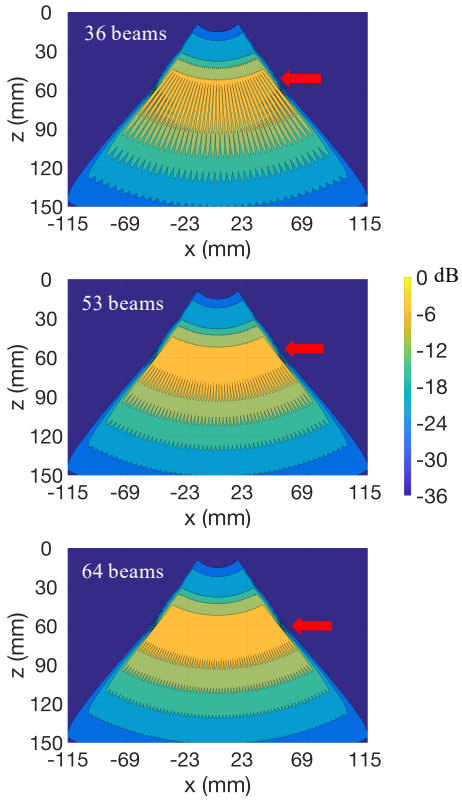

Fig. 3.2. The area of the overlapping -6dB beamwidths of each individual 2nd harmonic beam (yellow area pointed by the red arrow) increased as the number of transmit beams increased from 36 to 64 beams. Pressure is in dB scale normalized with respect to the maximum pressure.

3.2.3 *Amplitude limits*

3.2.3.1 *Amplitude limit due to transducer heating*

The transducer surface temperature increases when operating at higher amplitudes. Thus, sometimes the amplitude used in harmonic imaging may be limited by the maximum allowable transducer temperature [31]. The International Electrotechnical Commission Standard requires that the maximum surface temperature not exceed 43°C when measured under simulated use conditions using tissue mimicking material, and 50°C when measured in quiescent air temperature [32]. We have determined with measurements the highest source pressure of the X5-1 probe that produces 43°C in air and used it as the maximum source pressure in our simulations. The maximum source pressure was determined at 43°C instead of 50°C in air to avoid damages to the probe. The excitation voltage that raises the transducer surface temperature to 43°C in air was first identified by increasing the excitation voltage until the transducer surface temperature reached a steady state

at 43°C for 10 minutes. The transducer surface temperature was measured with a thermocouple (DTM 318, TECPEL Co., Taiwan). The temperature measurement was comparable to the temperature measurement recorded in the scanner acoustic power and intensity (API) measurements. The acoustic pressure across the surface of the probe at 5 mm (using the excitation voltage that raises the transducer surface temperature to 43°C in air) was measured in a water tank. A membrane hydrophone (UT1604, Precision Acoustics, Dorset, UK), attached to the motion stage was used for the acoustic field measurements. The average pressure across the surface of the transducer was then used as the source pressure in the KZK simulations.

3.2.3.2 *Acoustic output parameters*

The US Food and Drug Administration (FDA) imposes limitations on the maximum value of acoustic output parameters for clinical use of medical ultrasound to avoid adverse bioeffects: MI $\leq$ 1.9, $I_{sppa} \leq 190$ W/cm^2, and $I_{spta} \leq 720$ mW/cm^2 [33]. The MI was calculated as the peak negative pressure in situ divided by the square root of the frequency. The I_{sppa} is the maximum value of pulse-average intensity from different locations (*z)* in an acoustic field and is defined as:

$$I_{sppa} = \max_z \{\frac{1}{t_d}\int_0^{t_d} \frac{p^2(z,t)}{\rho c} dt\}, \tag{3.2}$$

where t_d is the pulse duration in seconds and was calculated as 1.25 times of the time period when pulse-pressure-square-integral reaches from 10% to 90% of its final value [34]. The I_{spta} is the maximum value of the temporal-average intensity in an acoustic field and is defined as [34]:

$$I_{spta} = \max_z \{VR \times \int_0^{VR^{-1}} \frac{p^2(z,t)}{\rho c} dt\}, \tag{3.3}$$

where *VR* is the volume rate in Hz.

3.3 RESULTS

3.3.1 *Spatial characteristics of the fundamental beam*

The peak pressures of the linear acoustic fields as both AF and EF increased from 75 to 250 mm are shown in **Fig. 3.3** (a). The peak pressure values in **Fig. 3.3** (a) are in a logarithmic scale (dB) after normalizing with respect to the peak pressure produced by AF=EF=75. As shown in the figure, AF=EF=75, which resulted in the smallest f-number, produced the highest peak pressure compared to when the AF and EF were greater. Focusing at the deepest depth (AF=EF=250) which results in the largest *f-number* produced the lowest peak pressure, which is 9.4 dB less than that of AF=EF=75. Field II simulations of the average -6dB beamwidth of the lateral fields as both AF and EF increased from 75 to 250 mm are shown in **Fig. 3.3** (b). As expected, AF=EF=250 produced a field that has the largest average -6dB beamwidth (5.7 mm) and AF=EF=75 produced a field that has the smallest (0.7 mm). In addition, it is observed in the figure that deep AF and centrally placed EF (AF=250/EF=75) produced a field that has slightly lower average -6dB beamwidth (4.3 mm), but higher peak pressure (3.3 dB) compared to that of AF=EF=250. On the other hand, the average -6dB beamwidth (1.7 mm) of the field produced by centrally placed AF and deep EF (AF=75/EF=250) was much lower than that of the field produced by AF=EF=250.

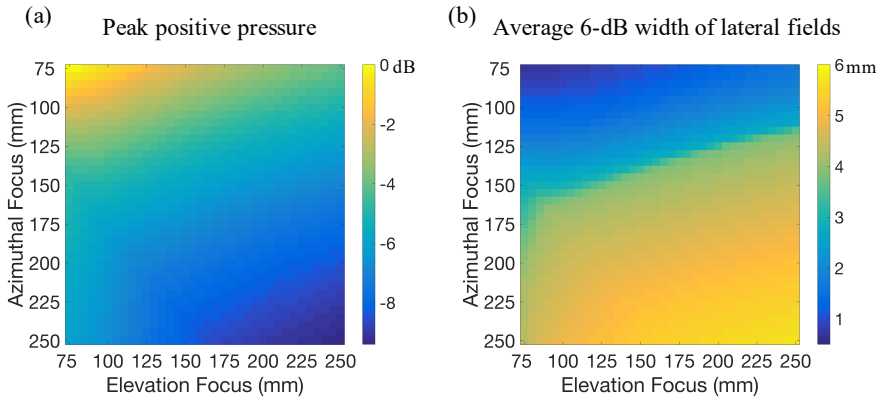

Fig. 3.3. Field II simulations of the (a) peak positive pressure and and (b) average -6dB beamwidth of lateral fields as AF-EF changes from 75 to 250 mm. Peak positive pressure values in (a) are in dB normalized with respect to the peak positive pressure value of AF=EF=75 mm. In (b) the values are the average from the -6dB beamwidth of the lateral fields on azimuthal and elevation plane from z=0 to 150 mm.

3.3.2 *Nonlinear simulations: the magnitude of the 2nd harmonic*

The source pressure of the X5-1 array across the azimuthal and elevation planes measured at 5 mm is shown in **Fig. 3.4**. We assumed that the source pressure does not change much in amplitude in

the first few mm. From these measurements we established that 0.6 MPa is the highest source pressure to be used in the simulation that does not result in transducer surface temperature greater than what FDA allows. Contour plots of the 2nd harmonic component produced by 4 AF/EF combinations are shown in **Fig. 3.5**. The contour plots are in logarithmic scale (dB) after normalizing with respect to the maximum value in AF=EF=75. As seen in the figure, the magnitude of the 2nd harmonic component is reduced as the azimuthal and elevation foci are increased. In **Table 3.2** we tabulate the important characteristics of the 2nd harmonic in the various cases considered. When AF=EF=75 mm, the amplitude of the 2nd harmonic was the highest despite using a lower source pressure since the I_{sppa} is at the safety limit. The 2nd harmonic along the propagation axis for each beamforming approach is shown in **Fig. 3.6** (a). The y-axis is in dB after normalizing with respect to the maximum value in AF=EF=75. As also shown in **Table 3.2**, PWI produced the lowest peak 2nd harmonic (0.06 MPa), which is ~20 dB lower than that produced by AF=EF=75. AF=EF=250 produced the second lowest peak 2nd harmonic (0.17 MPa), which is 10.8 dB lower than that produced by AF=EF=75. The peak 2nd harmonic produced by AF=250/EF=75 was 0.27 MPa, which is 6.8 dB lower than that of AF=EF=75. At the maximum imaging depth (150mm), AF=EF=250 produced the highest 2nd harmonic (0.13 MPa). AF=250/EF=75 produced the second highest 2nd harmonic (0.1 MPa), 2.3 dB lower than that of AF=EF=250. PWI and AF=EF=75 produced comparable 2nd harmonic (~0.04 MPa), which is 10.2 dB lower than that of AF=EF=250.

Table 3.2: Source pressure, characteristics of the 2nd harmonic beam, transmit pattern, and volume rate of different beamforming approaches.

Beamforming approaches (mm)	AF/EF =75	AF =250 EF = 75	AF/EF =250	PWI
Source pressure (MPa)	0.5	0.6	0.6	0.6
Peak 2nd harmonic (MPa)	0.59	0.27	0.17	0.06
2nd harmonic at 150 mm (MPa)	0.040	0.1	0.13	0.045
6-dB range of axial field (mm)	42	91	86	128
Average 6-dB width of lateral fields (mm)	0.3	1.64	1.58	5.4
Transmit pattern (azim×elev)	59×55	10×51	17×37	9×10
Volume rate (Hz)	1	8	6	44

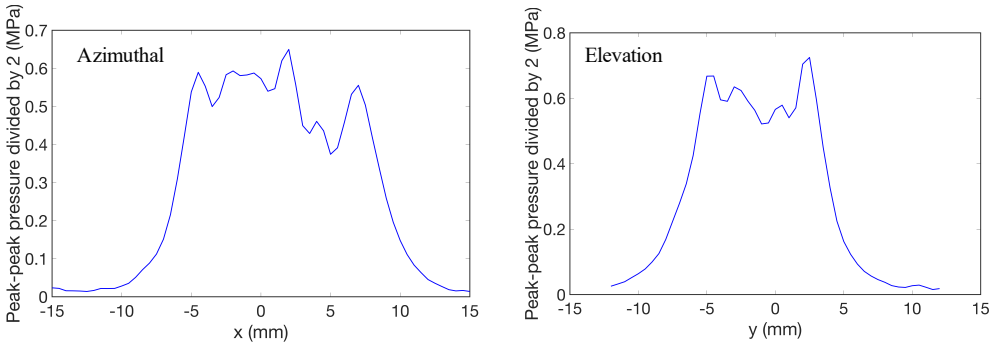

Fig. 3.4. The acoustic pressure across the azimuthal and elevation plane at z=5 mm produced by the X5-1 array using the excitation voltage that raises the transducer surface temperature to 43°C in air.

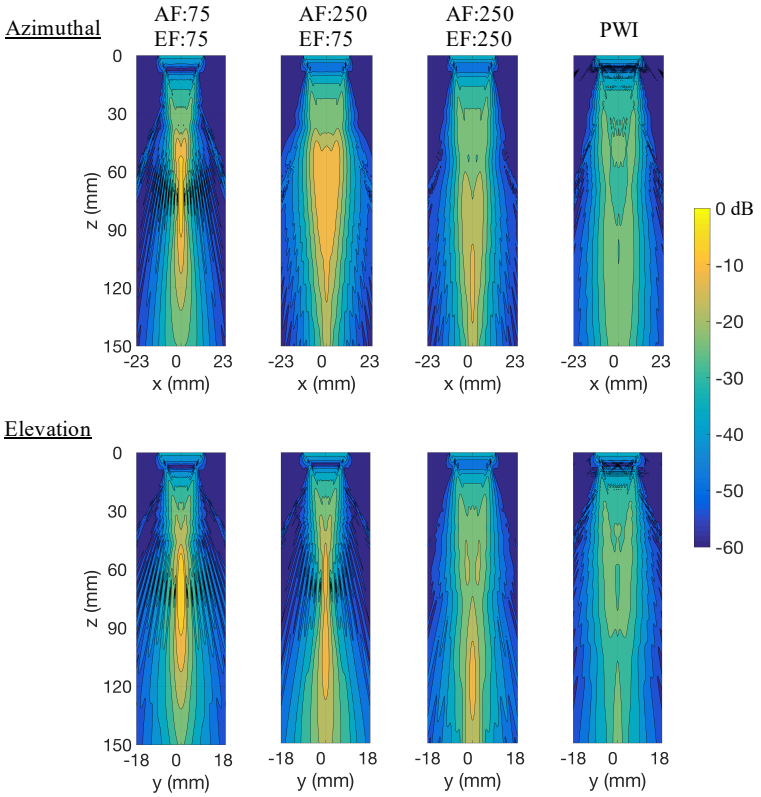

Fig. 3.5. Beam plots of the 2nd harmonic in the azimuthal and elevation plane produced by the matrix array with 4 beamforming approaches.

3.3.3 *Nonlinear simulations: spatial characteristics of the 2nd harmonic*

The average -6dB beamwidth of the lateral fields of each beamforming approach is shown in **Fig. 3.6** (b). PWI produced the widest 2nd harmonic beam and AF=EF=75 produced the narrowest. The average -6dB beamwidth of the 2nd harmonic beam produced by PWI was roughly 18 times wider than that produced by AF=EF=75 (5.4 vs 0.3 mm). Using a wider beam for 4D cardiac THI would cover more area in a single transmit event and thus improve the volume rate of 4D cardiac THI. 2nd harmonic beams produced by AF=250/EF=75 and AF=EF=250 have comparable average -6dB beamwidths (1.64 and 1.58 mm, respectively) which are roughly 5 times wider than that produced by AF=EF=75.

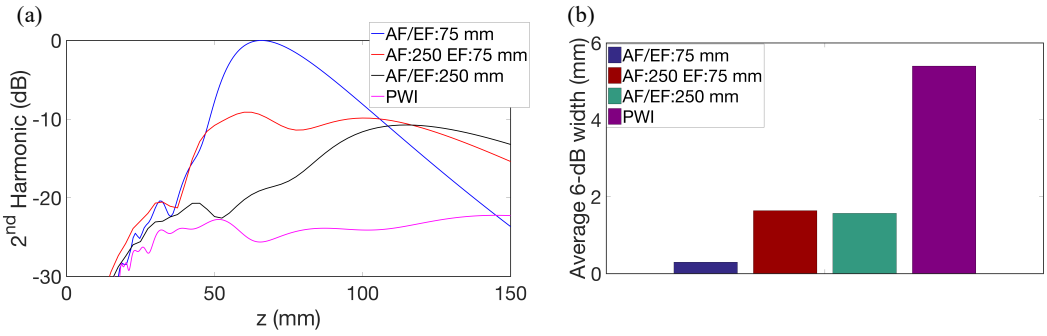

Fig. 3.6. (a) Amplitude of the 2nd harmonic along the axis of the array and (b) average -6dB beamwidth of the lateral fields produced by 4 beamforming approaches.

3.3.4 *Nonlinear simulations: Calculation of the volume rate*

The area covered by the -6dB beamwidth of the 2nd harmonic beam produced by AF=EF=75 as the number of transmit beams increased from 36 to 64 beams is shown in **Fig. 3.7**. At least 59 beams [**Fig. 3.7** (a)] and 55 beams [**Fig. 3.7** (b)] were required to sample 90% of the area sampled by transmitting 64 beams. Therefore, a transmit pattern of 59×55 beams was used for AF=EF=75 in 4D cardiac THI. The transmit patterns of other AF/EF combinations that cover an equal or larger area than that of AF=EF=75 are shown in **Fig. 3.8** and also listed in **Table 3.2**. The contour plots in **Fig. 3.8** are in a logarithmic scale (dB) after normalizing with respect to the maximum value in each approach. As shown in **Table 3.2**, the image volume is sampled with 59×55 beams with AF=EF=75 and 10×51 beams with AF=250/EF=75. The transmit pattern of AF=EF=75 and AF=250/EF=75 would result in a volume rate of 1 and 8 Hz, respectively. For PWI, the image volume is sampled with 9×10 beams and the volume rate is 44 Hz.

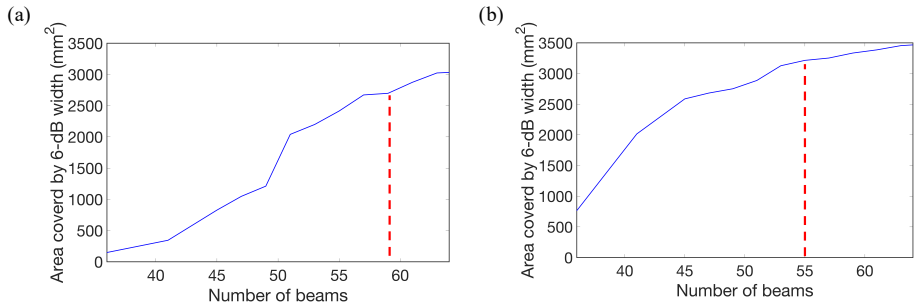

Fig. 3.7. The area covered by the overlapping -6dB beamwidth of the 2nd harmonic beam produced by AF/EF=75 mm in the (a) azimuthal and (b) elevation plane as the number of transmit beams increased. The red dashed line indicates the number of transmit beams required to sample 90% of the area sampled by 64 transmit beams.

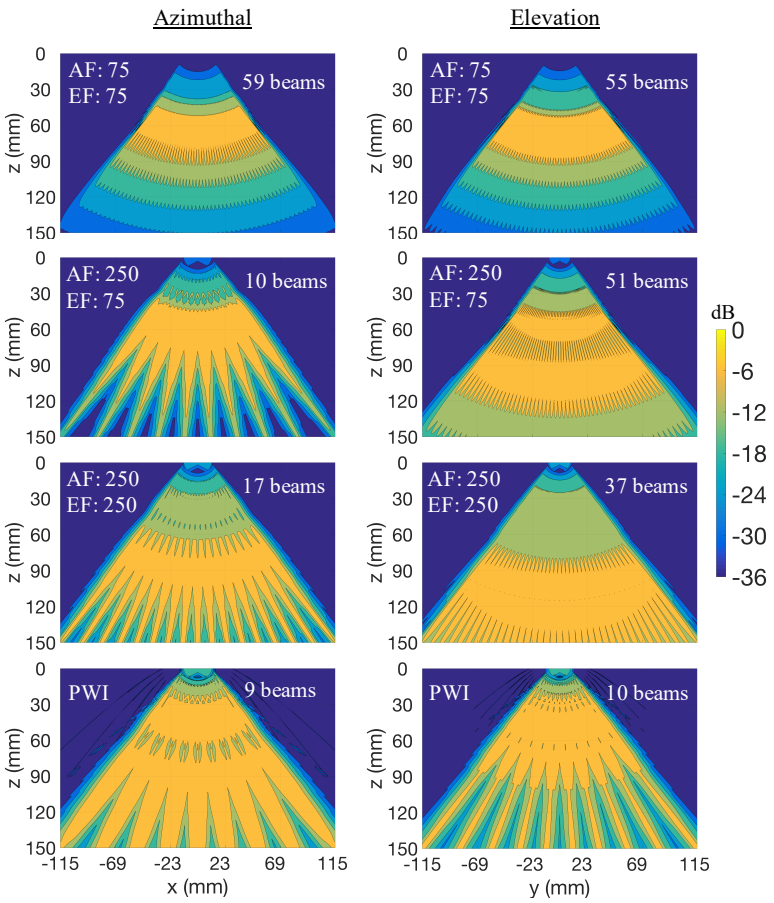

Fig. 3.8. Sampling of the azimuthal and elevation plane with individual beams for the various beamforming approaches considered. A single beam is steered in order to fill the volume in such a way that the area coverage of the overlapping -6dB beamwidths is equivalent to at least 90% of the area coverage by that of 64 transmit beams with AF/EF=75mm.

3.3.5 *Acoustic output*

The peak MI, I_{sppa}, and I_{spta} of each beamforming approach are shown in **Table 3.3**. As expected, with the highest focusing gain compared to other beamforming approaches, AF=EF=75 produced the highest peak MI of 1.4 and the highest I_{sppa} of 190 W/cm^2 in tissue, which is the safety limit. Without focusing in both the azimuthal and elevation planes, PWI produced the lowest peak MI of 0.5 and the lowest I_{sppa} of 17 W/cm^2 in tissue compared to the other beamforming approaches.

Table 3.3: Transducer surface temperature, I_{spta}, I_{sppa}, and peak MI produced by different beamforming approaches.

	AF/EF =75	AF =250 EF = 75	AF/EF = 250	PWI
Scan Head Temperature	38°C	43°C	43°C	43°C
I_{SPTA} ($^{mW}/_{cm^2}$)	1.3	5.9	3.7	8.7
I_{SPPA} ($^{W}/_{cm^2}$)	190	67	31	17
Peak MI	1.4	0.9	0.6	0.5

3.4 DISCUSSION

3.4.1 *Simulation*

The acoustic field produced by a Philips X5-1 matrix array was modeled with Field II and KZK in this study. A total of 1296 beamforming approaches with different AF/EF were modeled with Field II to evaluate the changes of spatial extent and magnitude of the fundamental component of the field as different AF and EF were used. Field II was used to model the linear field from a large number of beamforming approaches since it is much faster than KZK. The generation of the harmonic component is dependent on the pressure amplitude of the fundamental component of the field. Therefore, although Field II is not capable of modeling the nonlinear propagation of the sound beams, modeling the fundamental component of the field with Field II still provides insight into how acoustic fields are affected with different AF and EF combinations. This in turn allows a higher lever selection of specific beamforming approaches for further simulations of harmonic generation of the field with KZK. The KZK simulations are of course much more computationally intensive and required about 12 hours per case. In particular, for KZK simulation of DWI, since not only a smaller step size in both azimuthal and elevation dimension was required to capture the curvature of the wave fronts, but a pulse with a longer tail was also necessary to correctly model the diffraction in regions far away from the propagation axis, the simulation took up to 48 hours to finish. All Field II and KZK simulations were performed on a workstation with 4.2 GHz Intel(R) Core(TM) i7-7700K and 32 GB of RAM running the Windows 10 operating system.

To image the whole heart, beam steering for a 75° × 75° volume is typically required [35]. Although previous studies have modified the numerical model of KZK to model steered beams

[30, 36], such KZK simulations remain time-consuming. Therefore, steered 2nd harmonic beams at different angles were approximated by rotating an unsteered 2nd harmonic beam in the present study. To evaluate the validity of approximating steered 2nd harmonic beams with rotated beams, we instead evaluated the difference between the steered and rotated fundamental beams with Field II simulations since the generation of the harmonic beam is strongly dependent on the pressure amplitude of the fundamental beam. Field II simulations comparing the steered and rotated fundamental beams at 37.5° (the maximum angle used in this calculation) when using AF=EF=75 and PWI are shown in **Fig. 3.9**. It is observed that the difference between the steered and rotated beams is larger when the beam is more focused (**Fig. 3.9**). However, **Fig. 3.9** (c) and (f) show that the steered and rotated fundamental beams were still in a good agreement in terms of pressure. Since the difference between the steered and rotated beams increased at a larger angle, the fact that we observed good agreement between steered and rotated fundamental beams even at the largest angle (37.5°) increased our confidence in the validity of approximating steered 2nd harmonic beams with rotated 2nd harmonic beams.

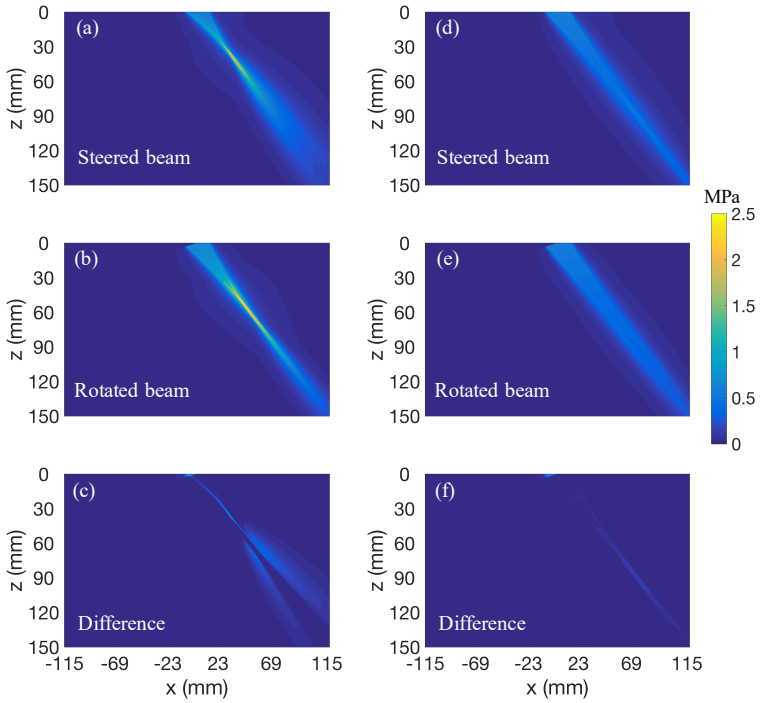

Fig. 3.9. Peak positive pressure of the steered beams at 37.5° produced by (a) AF=EF=75 and (d) PWI. Peak positive pressure of the unsteered beams rotated at 37.5° produced by (b) AF=EF=75 and (e) PWI. The absolute difference between steered and rotated beams of (c) AF=EF=75 and (f) PWI.

3.4.2 *Observations and implications for imaging*

Fig. 2.3 (a) demonstrated that the beamforming approaches with higher focusing gains (smaller *f-number*) produce higher peak positive pressures in tissue. The focusing gain of an aperture is defined as z_0/d, where z_0 is the Rayleigh distance and d is the focal length of the aperture, respectively. Since the Rayleigh distance of an aperture is proportional to the square of the aperture width, with a wider width in azimuthal compared to elevation dimension (23 vs 18 mm), the focusing gain of X5-1 in azimuthal plane is 1.28^2X higher than that in elevation plane when both have the same focal length. As a result, using AF=250/EF=75 for imaging would result in comparable focusing gains, creating a uniform field along the propagation as shown in **Fig. 3.6** (a). In contrast, in the case of AF=75/EF=250, since the focusing gain produced by AF is 6 times higher than that of EF, the field would be mostly focused towards 75 mm.

The 2nd harmonic component used in harmonic imaging is proportional to the source amplitude. From the nonlinear simulations, we identified that the transducer surface temperature is the main amplitude limiting factor, as opposed to the MI, I_{sppa}, or I_{spta}. The only exception is the case of a highly focused (lower *f-number*) beamforming approach (AF=EF=75), where I_{sppa} reached the safety limit (190 W/cm^2) before the transducer surface temperature reached 43°C in air. In our previous work where we assumed that the amplitude would be MI-limited without taking into consideration the transducer surface temperature, (MI=1.9), the peak 2nd harmonic produced by PWI was predicted to be only 4 dB lower than that of AF=EF=75 [37]. However, as transducer surface temperature and I_{sppa} in addition to MI were taken into consideration in the present work, the difference between the peak 2nd harmonic produced by AF=EF=75 and PWI increased to ~20 dB (**Table 3.2**). Recent developments in shear-wave elastography (SWE) have led to improvements in heat removal and deposition [38], which have mitigated the problem of transducer surface heating and may lead to the use of higher source pressures for 4D cardiac THI.

As demonstrated in **Fig. 3.5** and **Fig. 3.6**, AF=250/EF=75 produced the widest and the most uniform 2nd harmonic beam along the propagation axis compared to that produced by other conventional focused beamforming approaches (AF=EF=75 and AF=EF=250). In addition, the peak 2nd harmonic component produced by AF=250/EF=75 was only 6.8 dB lower than that

produced by AF=EF=75. As a result, using deep AF and centrally placed EF such as AF=250/EF=75 for 4D cardiac THI may be an option for imaging applications that need fast volume rate and good SNR at all depth. On the other hand, although PWI produced the lowest peak 2nd harmonic component compared to that produced by other beamforming approaches, the peak 2nd harmonic component produced by PWI was found to be 9-20 dB lower than that produced by conventional focused beamforming approaches (**Table 3.2**). Despite this being a considerable reduction of the harmonic level, it may still be feasible to use PWI for 4D cardiac THI.

As shown in **Fig. 3.8** and **Table 3.2**, the volume rate of the AF/EF combinations we have considered for 4D cardiac THI are in the range of 1-8 Hz with conventional focused beamforming and 44 Hz with PWI. In calculating the volume rate, we assume that each harmonic component is isolated with digital filtering [17] and does not require additional transmit events such as PI which further reduces the volume rate by half [39].

To further increase the volume rate, a narrower field of view may be used for 4D imaging. For example, in "zoom mode" of 4D imaging, the field of view may be reduced to 30° × 30° [3], increasing the volume rate 6x compared to that when imaging a 75° × 75° volume. In addition, multi-line transmit (MLT) is a technique that can increase volume rate by simultaneously transmitting multiple beams into different directions [35, 40]. With MLT, the transmit delays applied to the array elements to generate subsequent beams are superimposed to simultaneously transmit multiple beams [41]. A previous study has achieved a 4 time higher frame rate without significantly compromising spatial resolution with an ultrasound open platform which transmits 4 focused beams simultaneously [40]. However, the SNR would be compromised when using MLT for 4D cardiac THI since a lower source pressure must be used to transmit multiple beams simultaneously without exceeding the safety limit. Finally, DWI significantly improves the volume rate by insonifying a large area with every transmit [11]. As shown in **Fig. 3.10**, DWI requires only 3×3 beams to sample the volume. This results in a volume rate of ~444 Hz which is much faster than that of other beamforming approaches. However, the peak 2nd harmonic component produced by DWI is 23 dB lower than that of AF=250/EF=75. At the maximum imaging depth (150mm), the 2nd harmonic component produced by DWI is 40 dB lower than that of AF=250/EF=75. It is much more difficult to produce enough 2nd harmonic component with DWI since the amplitude is

very low due to the diverging nature of the wavefronts. Increasing the divergence of the field may further increase the volume rate, while producing even lower 2nd harmonic component. Further studies are needed to investigate whether coherent compounding [12, 13] and delay-encoded harmonic imaging techniques [42] are able to recover the SNR of DWI.

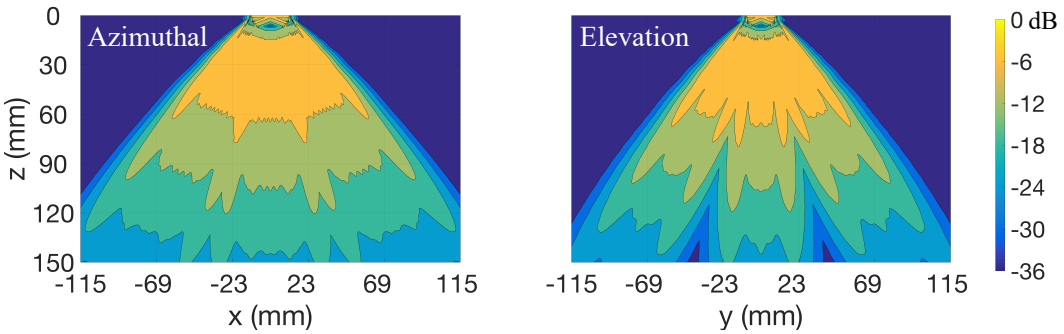

Fig. 3.10. Sampling of the azimuthal and elevation plane with individual beams of DWI. A single beam is steered in order to fill the volume in such a way that the area coverage of the overlapping -6dB beamwidths is equivalent to at least 90% of the area coverage by that of 64 transmit beams with AF/EF=75mm.

3.5 CONCLUSION

We have investigated the harmonic generation of a matrix array for 4D cardiac THI with a nonlinear propagation simulation model based on the KZK equation. We evaluated how beamforming approaches affect the transmitted acoustic field and considered different azimuthal/elevation focus combinations as well as PWI and DWI approaches. We found that centrally placed foci produced the highest peak 2nd harmonic component in tissue (0.59 MPa) and required the lowest volume rate to fill the volume. The peak 2nd harmonic component produced by PWI was found to be 9-20 dB lower than that produced by conventional focused beamforming approaches. Despite this reduction it may still be feasible to use PWI and DWI for 4D cardiac THI, but this needs to be confirmed by experimental studies. The volume rates for the beamforming approaches we have considered for 4D cardiac THI are in the range 1-8 Hz with conventional focused beamforming (depending on the focal depths), 44 Hz with PWI, and 444 Hz with DWI. Our work provides useful insight into the compromise between the magnitude and the spatial extent of the 2nd harmonic produced by different beamforming approaches, and outlines an analytical framework for identifying optimal beamforming approaches for specific applications.

3.6 ACKNOWLEDGEMENTS

The research reported in this study was partially supported by the National Institute of Biomedical Imaging and Bioengineering of the National Institutes of Health under Award Number T32EB001650 and College of Engineering Fellowship from the James Chao-Yao Koh and Maria Lee Koh Endowed Fellowship fund.

3.7 REFERENCES

[1] E. J. Benjamin *et al.*, "Heart disease and stroke statistics—2018 update: a report from the American Heart Association," *Circulation,* vol. 137, no. 12, pp. e67-e492, 2018.

[2] H. Feigenbaum, "Evolution of echocardiography," *Circulation,* vol. 93, no. 7, pp. 1321-1327, 1996.

[3] R. M. Lang, V. Mor-Avi, L. Sugeng, P. S. Nieman, and D. J. Sahn, "Three-dimensional echocardiography: the benefits of the additional dimension," *Journal of the American College of Cardiology,* vol. 48, no. 10, pp. 2053-2069, 2006.

[4] R. M. Lang, K. Addetia, A. Narang, and V. Mor-Avi, "3-Dimensional echocardiography: latest developments and future directions," *JACC: Cardiovascular Imaging,* vol. 11, no. 12, pp. 1854-1878, 2018.

[5] N. M. Daher and J. T. Yen, "2-D array for 3-D ultrasound imaging using synthetic aperture techniques," *IEEE transactions on ultrasonics, ferroelectrics, and frequency control,* vol. 53, no. 5, pp. 912-924, 2006.

[6] M. Cikes, L. Tong, G. R. Sutherland, and J. D'hooge, "Ultrafast cardiac ultrasound imaging: technical principles, applications, and clinical benefits," *JACC: Cardiovascular Imaging,* vol. 7, no. 8, pp. 812-823, 2014.

[7] H. Kanai and Y. Koiwa, "Myocardial rapid velocity distribution," *Ultrasound in medicine & biology,* vol. 27, no. 4, pp. 481-498, 2001.

[8] D. P. Shattuck, M. D. Weinshenker, S. W. Smith, and O. T. von Ramm, "Explososcan: A parallel processing technique for high speed ultrasound imaging with linear phased arrays," *The Journal of the Acoustical Society of America,* vol. 75, no. 4, pp. 1273-1282, 1984.

[9] O. T. Von Ramm, S. W. Smith, and H. G. Pavy, "High-speed ultrasound volumetric imaging system. II. Parallel processing and image display," *IEEE transactions on ultrasonics, ferroelectrics, and frequency control,* vol. 38, no. 2, pp. 109-115, 1991.

[10] J. Provost *et al.*, "3D ultrafast ultrasound imaging in vivo," *Physics in Medicine & Biology,* vol. 59, no. 19, p. L1, 2014.

[11] M. Correia, J. Provost, M. Tanter, and M. Pernot, "4D ultrafast ultrasound flow imaging: in vivo quantification of arterial volumetric flow rate in a single heartbeat," *Physics in Medicine & Biology,* vol. 61, no. 23, p. L48, 2016.

[12] B. Denarie *et al.*, "Coherent plane wave compounding for very high frame rate ultrasonography of rapidly moving targets," *IEEE transactions on medical imaging,* vol. 32, no. 7, pp. 1265-1276, 2013.

[13] G. Montaldo, M. Tanter, J. Bercoff, N. Benech, and M. Fink, "Coherent plane-wave compounding for very high frame rate ultrasonography and transient elastography," *IEEE*

transactions on ultrasonics, ferroelectrics, and frequency control, vol. 56, no. 3, pp. 489-506, 2009.

[14] L. Demi, "Practical guide to ultrasound beam forming: Beam pattern and image reconstruction analysis," *Applied Sciences,* vol. 8, no. 9, p. 1544, 2018.

[15] J. Jensen, M. B. Stuart, and J. A. Jensen, "Optimized plane wave imaging for fast and high-quality ultrasound imaging," *IEEE transactions on ultrasonics, ferroelectrics, and frequency control,* vol. 63, no. 11, pp. 1922-1934, 2016.

[16] E. Tiran *et al.*, "Multiplane wave imaging increases signal-to-noise ratio in ultrafast ultrasound imaging," *Physics in Medicine & Biology,* vol. 60, no. 21, p. 8549, 2015.

[17] M. A. Averkiou, D. N. Roundhill, and J. E. Powers, "A new imaging technique based on the nonlinear properties of tissues," in *1997 IEEE Ultrasonics Symposium Proceedings. An International Symposium (Cat. No. 97CH36118)*, 1997, vol. 2, pp. 1561-1566: IEEE.

[18] M. A. Averkiou, "Tissue harmonic ultrasonic imaging," *Comptes Rendus de l'Académie des Sciences-Series IV-Physics,* vol. 2, no. 8, pp. 1139-1151, 2001.

[19] T. Whittingham, "Tissue harmonic imaging," *European radiology,* vol. 9, pp. S323-S326, 1999.

[20] M. Correia, J. Provost, S. Chatelin, O. Villemain, M. Tanter, and M. Pernot, "Ultrafast harmonic coherent compound (UHCC) imaging for high frame rate echocardiography and shear-wave elastography," *IEEE transactions on ultrasonics, ferroelectrics, and frequency control,* vol. 63, no. 3, pp. 420-431, 2016.

[21] T. Lai, M. Bruce, and M. Averkiou, "Modeling of the Acoustic Field Produced by Diagnostic Ultrasound Arrays in Plane and Diverging Wave Modes," *IEEE transactions on ultrasonics, ferroelectrics, and frequency control,* 2019.

[22] M. A. Averkiou and M. F. Hamilton, "Measurements of harmonic generation in a focused finite-amplitude sound beam," *The Journal of the Acoustical Society of America,* vol. 98, no. 6, pp. 3439-3442, 1995.

[23] M. A. Averkiou, Y. S. Lee, and M. F. Hamilton, "Self-demodulation of amplitude-and frequency-modulated pulses in a thermoviscous fluid," *The Journal of the Acoustical Society of America,* vol. 94, no. 5, pp. 2876-2883, 1993.

[24] V. Kuznetsov, "Equations of nonlinear acoustics," *Sov. Phys. Acoust.,* vol. 16, pp. 467-470, 1971.

[25] E. Zabolotskaya, "Quasi-plane waves, in the nonlinear acoustics of confined beams," *Sov. Phys. Acoust.,* vol. 15, pp. 35-40, 1969.

[26] J. A. Jensen and N. B. Svendsen, "Calculation of pressure fields from arbitrarily shaped, apodized, and excited ultrasound transducers," *IEEE transactions on ultrasonics, ferroelectrics, and frequency control,* vol. 39, no. 2, pp. 262-267, 1992.

[27] J. A. Jensen, "Field: A program for simulating ultrasound systems," in *10TH NORDICBALTIC CONFERENCE ON BIOMEDICAL IMAGING, VOL. 4, SUPPLEMENT 1, PART 1: 351--353*, 1996: Citeseer.

[28] J. N. Tjo/tta, S. Tjo/tta, and E. H. Vefring, "Effects of focusing on the nonlinear interaction between two collinear finite amplitude sound beams," *The Journal of the Acoustical Society of America,* vol. 89, no. 3, pp. 1017-1027, 1991.

[29] J. Naze Tjo/tta, S. Tjo/tta, and E. H. Vefring, "Propagation and interaction of two collinear finite amplitude sound beams," *The Journal of the Acoustical Society of America,* vol. 88, no. 6, pp. 2859-2870, 1990.

[30] M. Voormolen, *3d harmonic echocardiography*. 2007.

[31] F. Duck, H. Starritt, G. ter Haar, and M. Lunt, "Surface heating of diagnostic ultrasound transducers," *The British journal of radiology,* vol. 62, no. 743, pp. 1005-1013, 1989.
[32] I. Standard, "Particular requirements for the safety of ultrasonic medical diagnostic and monitoring equipment," Vol. Tech. Rep. Geneva, Switzerland: International Electrotechnical Committee2011.
[33] Food and D. Administration, "Information for manufacturers seeking marketing clearance of diagnostic ultrasound systems and transducers," *Guidance for Industry and FDA Staff,* 2008.
[34] P. Santos, L. Tong, A. Ortega, L. Løvstakken, E. Samset, and J. D'hooge, "Acoustic output of multi-line transmit beamforming for fast cardiac imaging: a simulation study," *IEEE transactions on ultrasonics, ferroelectrics, and frequency control,* vol. 62, no. 7, pp. 1320-1330, 2015.
[35] A. Ortega Castrillon, "Novel beamforming methods for fast volumetric cardiac imaging using ultrasound," 2016.
[36] P. D. Fox, A. Bouakaz, and F. Tranquart, "Computation of steered nonlinear fields using offset KZK axes," 2005.
[37] T.-Y. Lai, S. Kou, M. Bruce, T. Loupas, and M. A. Averkiou, "Harmonic Generation in Tissue with Matrix Arrays for 4D Cardiac THI," in *2019 IEEE International Ultrasonics Symposium (IUS)*, 2019, pp. 1834-1837: IEEE.
[38] W. Qiu *et al.*, "A scanning-mode 2D shear wave imaging (s2D-SWI) system for ultrasound elastography," *Ultrasonics,* vol. 62, pp. 89-96, 2015.
[39] T. A. Whittingham, "Contrast-specific imaging techniques: technical perspective," in *Contrast media in ultrasonography*: Springer, 2005, pp. 43-70.
[40] L. Tong, A. Ramalli, R. Jasaityte, P. Tortoli, and J. D'hooge, "Multi-transmit beam forming for fast cardiac imaging—Experimental validation and in vivo application," *IEEE transactions on medical imaging,* vol. 33, no. 6, pp. 1205-1219, 2014.
[41] L. Tong, H. Gao, and J. D'hooge, "Multi-transmit beam forming for fast cardiac imaging-a simulation study," *IEEE transactions on ultrasonics, ferroelectrics, and frequency control,* vol. 60, no. 8, pp. 1719-1731, 2013.
[42] P. Gong, P. Song, and S. Chen, "Delay-encoded harmonic imaging (DE-HI) in multiplane-wave compounding," *IEEE transactions on medical imaging,* vol. 36, no. 4, pp. 952-959, 2016.

Chapter 4. LINEAR SIGNAL CANCELLATION OF NONLINEAR PULSING SCHEMES IN A VERASONICS RESEARCH SCANNER

Abstract

Contrast enhanced ultrasound (CEUS) is a real-time imaging technique that allows the visualization of organ and tumor microcirculation by utilizing the nonlinear response of microbubbles. Nonlinear pulsing schemes are used exclusively in CEUS imaging modes in modern scanners. One important aspect of nonlinear pulsing schemes is the near-complete elimination of the linear signals that originate from tissue. Up until now, no study has investigated the performance of Verasonics scanners in eliminating the linear signals during CEUS and, by extension, the optimal pulsing sequences for performing CEUS. The aim of the present study was to investigate linear signal cancellation of the Verasonics scanner performing nonlinear pulsing schemes with 2 different probes (L7-4 linear array and C5-2 convex array). We have considered 2 pulsing schemes: pulse inversion (PI) and amplitude modulation (AM). We have also compared our results from the Verasonics scanner with a clinical scanner (Philips iU22). We found that the linear signal cancellation of the transmitted pulse by Verasonics scanner was ~40 dB in AM mode and ~30 dB in PI mode when operated at 0.06 MI. The linear signal cancellation performance of Verasonics scanner was comparable to Philips iU22 scanner in focused AM mode and on average 4 dB better than Philips iU22 scanner in focused PI mode.

4.1 INTRODUCTION

Contrast-enhanced ultrasound (CEUS) is a real-time imaging technique that allows visualization of the perfusion of organs and tumors [18, 19] by utilizing the nonlinear echoes from microbubbles [20]. Optimal CEUS imaging is usually achieved at low mechanical indices (MI $\leq$0.1) due to decreased microbubble destruction and reduced generation of tissue harmonics. In fact, excessive microbubble destruction could lead to spurious signal loss that may mimic lesion washout in real time CEUS imaging [21]. Meanwhile, tissue harmonics (generated by nonlinear propagation of ultrasound in the tissue and more pronounced at higher MIs) may interfere with or mask the presentation of bubble signals in CEUS images [22].

Earlier methods rely on digital filtering techniques that isolate the harmonic component of the signal to form the image [14, 23]. However, this approach leads to poor axial resolution since it requires the use of longer pulses (with narrower bandwidths) in order for the fundamental and the second harmonic components to be separable in the frequency domain and still fit in the frequency bandwidth of the transducer [24]. In addition, the overlap between the fundamental and second harmonic components cannot be separated with filtering, thus contributing to tissue cluttering and the degradation of the image [25].

To overcome the limitations mentioned above, nonlinear pulsing schemes have been developed. In nonlinear pulsing schemes, the scattered echoes of a series of transmitted pulses are combined in a way that the linear signals are cancelled while the nonlinear signals are detected [24, 26]. The two most used nonlinear pulsing schemes today are pulse inversion (PI) [27] and amplitude modulation (AM) [28, 29]. PI involves transmitting 2 pulses with the second pulse being the inverse of the first pulse (different in phase by π). By adding the produced echoes, the fundamental (and all odd harmonics) are removed even without any RF-filtering operation and the second (and all even) harmonics are detected. The AM technique involves transmitting 2 pulses at different amplitudes. A widely used version of AM is one where the amplitude of the second pulse is half that of the first pulse; the linear signals are removed by scaling the echoes of the second pulse by a factor of 2 and then subtracting them from the echoes of the first. Both PI and AM avoid the limitations of filter-based techniques (i.e., poor axial resolution and imperfect separation of linear and nonlinear signals) but at the expense of reduced frame rate.

However, hardware limitations of the ultrasound system may affect the precision of pulse inversion or amplitude change of the transmitted pulses, resulting in incomplete cancellation of the linear component of the echoes. The result is a "pseudo-enhancement" of nonlinear signals that can possibly mask real enhancement caused by bubbles or be incorrectly interpreted as real enhancement [24].

The Verasonics research ultrasound system (Verasonics, Inc., Kirkland, WA, USA) [30] has been widely adopted by research labs to investigate novel imaging techniques for CEUS [31-33]. The linear signal cancellation (LSC) performance of various ultrasound scanners has been investigated. Previous studies have shown that the LSC performance of Aixplorer scanner (Supersonic Imagine, Aix-en-Provence, France) was ~40 dB in plane AM mode [34] and the LSC performance of Sonoline Allegra Advanced system (Siemens Medical Systems, Inc., Issaquah, WA, USA) was ~30 dB in focused PI mode [35]. However, to the best of our knowledge, no study has yet investigated the ability of the Verasonics scanner to accurately transmit pulses for nonlinear pulsing schemes or the degree of LSC. Assessing the LSC performance of the Verasonics scanner in PI and AM mode is crucial in identifying the optimal nonlinear pulsing scheme for performing contrast imaging with the Verasonics scanner.

The aim of the present study was to investigate the LSC performance of the Verasonics scanner when imaging with 2 commonly used arrays (L7-4 linear array and C5-2 convex array). We have 2 specific objectives: first, to investigate the LSC of the Verasonics scanner in PI and AM mode; and second, to compare the LSC performance of Verasonics scanner with that of the Philips iU22 clinical ultrasound scanner (Philips Healthcare, Bothell, WA, USA).

4.2 MATERIALS AND METHODS

4.2.1 *Nonlinear pulsing schemes*

Here we describe the nonlinear pulsing schemes (PI and AM) and how we calculate the LSC. As shown in **Fig. 4.1** (a), PI was implemented by transmitting 2 pulses ($p_1(t)$ and $p_2(t)$) consecutively, where $p_2(t) = -p_1(t)$, and adding their respective echoes according to equation 4.1.

$$PS_{PI} = \frac{1}{2}p_{1s} + \frac{1}{2}p_{2s}, \qquad (4.1)$$

where p_{1s} and p_{2s} are echoes produced with p_1 and p_2, respectively. Since p_1 and p_2 differ by π, their respective odd harmonic components (n = 1, 3, 5, …) differ by nπ and are inverses of one another. Therefore, odd harmonics are canceled in PI whereas the even harmonic components (n=2, 4, 6, …) are doubled since they differ by 2nπ [1, 24].

On the other hand, AM typically consists of transmitting 2 pulses ($p_1(t)$ and $p_2(t)$), where the second pulse is half the amplitude of the first pulse ($p_2(t) = \frac{1}{2}p_1(t)$), and subtracting the respective echoes according to equation 4.2.

$$PS_{AM} = \frac{1}{3}p_{1s} - \frac{2}{3}p_{2s}, \quad (4.2)$$

where p_{1s} and p_{2s} are the backscattered signals of p_1 and p_2, respectively. However, transmitting two identical pulses with an exact amplitude ratio at different voltages is challenging due to nonlinearities in the signal generation and power amplifier. To avoid this issue, a technique often referred to as "checkerboard apertures" was developed [24, 28, 36, 37]. As shown in **Fig. 4.1** (b), this technique involves transmitting 3 pulses with the following sequence: p_{even}, p_{full}, and p_{odd}. With this technique, the transmit voltage and transmit beamforming delays are never changed among p_{even}, p_{full}, and p_{odd}, yet only even elements are used for transmitting p_{even}, only odd elements are used for p_{odd}, while all the elements are used for p_{full}. As a result, the effective beam shape used to form the sum of p_{even} and p_{odd} is identical to that used to form p_{full}. Moreover, since only half the elements are used for p_{even} and p_{odd}, the pressure produced by p_{even} and p_{odd} are half that produced by $p_{full.}$ A previous study reported that checkerboard apertures improves LSC and requires less hardware complexity [34]. In this study, AM was implemented on both Verasonics scanner and Philips iU22 scanner according to equation 4.3,

$$PS_{AM} = \frac{1}{3}ps_{full} - \frac{1}{3}ps_{even} - \frac{1}{3}ps_{odd}, \qquad (4.3)$$

where ps_{even}, ps_{full}, and ps_{odd} are the backscattered signals of p_{even}, p_{full}, and p_{odd}, respectively.

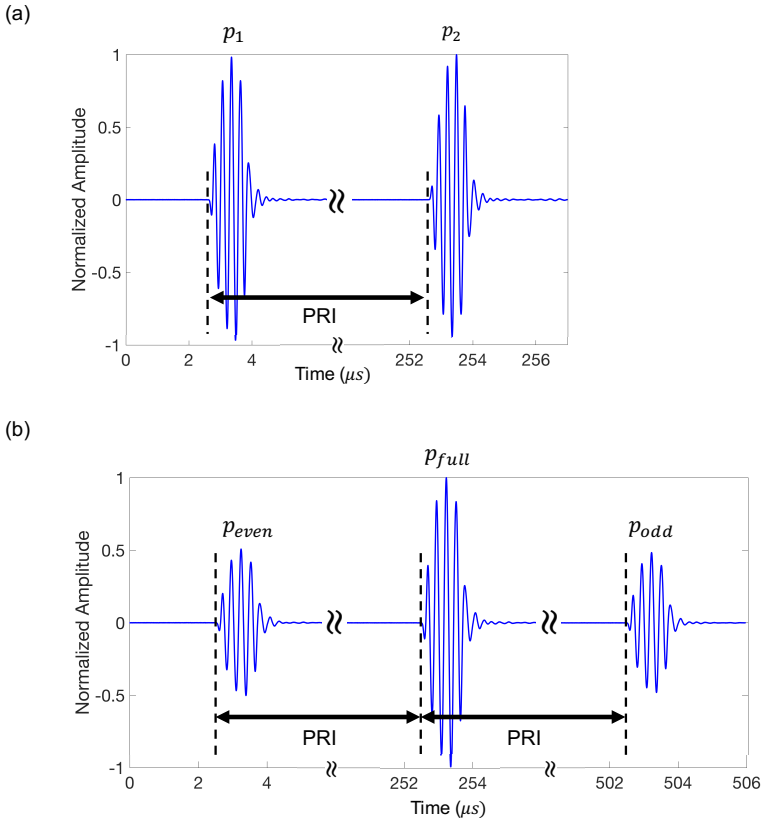

Fig. 4.1. Schematic of the pulsing sequence in PI (a) and in AM (b). In (a), each transmit event, p_1 and p_2 are separated by 1 PRF, and the amplitude of p_1 is identical to that of p_2. In (b), each transmit event, p_{even}, p_{full}, and p_{odd} are separated by 1 or 2 PRF, and p_{even} and p_{odd} are both at half amplitude of the p_{full}.

4.2.2 *Imaging parameters for Verasonics and Philips iU22 scanner*

In the present study, we evaluated LSC of the Verasonics scanner when using the L7-4 or C5-2 array and the LSC of Philips iU22 scanner with the L9-3 or C5-1 array. For the Verasonics scanner, we considered both conventional focused beamforming and plane/diverging wave mode. We used the same transmit frequency and number of cycles for the focused and plane/diverging wave modes. For all arrays, we used 2.5 cycle pulses. The imaging depth for the L7-4 array was 4 cm with a focus at 3 cm, and the imaging depth for the C5-2 array was 14 cm with a focus at 7 cm. The transmit frequencies of the L7-4 and C5-2 arrays were 3.5 MHz and 1.7 MHz, respectively, which were selected based on the measured individual frequency response of each array (**Fig. 4.2**).

For Philips iU22 scanner, we only evaluated LSC while in conventional focused mode since it did not support plane/diverging wave mode. The transmit frequency of the L9-3 and the C5-1 array in the default contrast modes was 3.1 MHz and 1.7 MHz, respectively. A windowed 4 cycle pulse was used in the C5-1 array, and windowed 3 and 4 cycle pulses for the L9-3 in PI and AM mode, respectively. The imaging depth for the L9-3 array was 4 cm with a focus at 3 cm, and the imaging depth for C5-1 array was 14 cm with a focus at 7 cm.

4.2.3 *Frequency response of the L7-4 and C5-2 array*

The frequency response of the array was obtained with the broadband impulse technique [38]. Briefly, the arrays were excited with a 20 MHz half-cycle pulse. **Fig. 4.2** shows the frequency spectrum of the transmitted pulse at the focus of each array measured with a 0.5 mm needle hydrophone (2842, Precision Acoustics, Dorset, UK), which was also used for all measurements in water.

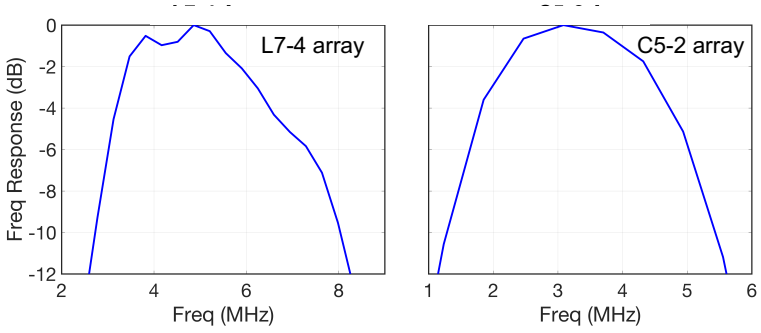

Fig. 4.2. Frequency spectra of L7-4 (a) and C5-2 (b).

4.2.4 *Hydrophone measurements of transmitted pulses in water*

The experimental set up for the hydrophone measurements is shown in **Fig. 4.3** (a). Hydrophone waveforms were recorded with a 0.5 mm needle hydrophone, and digitized with an oscilloscope (DPO7000C, Tektronix, Beaverton, OR, USA) at a sampling frequency of 500 MHz. All measurements were repeated 256 times and the average was recorded. The hydrophone was placed at a depth of 3 cm for linear array and 7 cm for convex array, consistent with the imaging foci of the arrays. In addition, in order to evaluate the effect of MI on the linear signal cancellation, we considered various input voltages that result in MI of 0.06, 0.10, 0.19, and 0.32 at the imaging

focus. The MI was calculated as the peak negative pressure in situ divided by the square root of the frequency. With these measurements, we only evaluate the transmit path. In a later section, we evaluate both transmit and receive paths with radio frequency (RF) data.

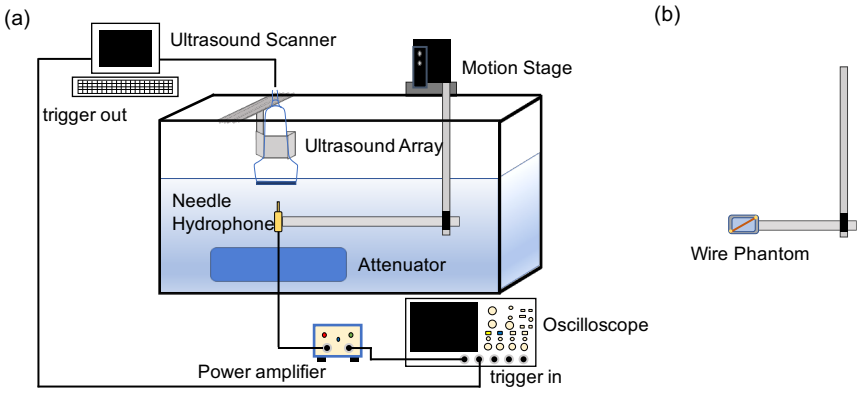

Fig. 4.3. (a) Experimental setup for measuring the ultrasound pulses of pulsing schemes in water. (b) We replace the needle hydrophone with a wire phantom for collecting RF data.

To measure the LSC of PI, the whole nonlinear pulsing sequence at the imaging focus was recorded [P in **Fig. 4.1** (a)]. The interruption in **Fig. 4.1** (a) indicates that the time between p_1 and p_2 is actually much longer. p_1 and p_2 in the pulsing sequence can be described in discrete form by equation (4.4) and (4.5), respectively.

$$p_1[n] = \sum_{k=p1_{start}}^{p1_{end}} P[k]\,\delta[n-k] \qquad (4.4)$$

$$p_2[n] = \sum_{k=p2_{start}}^{p2_{end}} P[k]\,\delta[n-k] \qquad (4.5)$$

where n is the nth sample of p_1 or p_2 and k is the kth sample of P. δ is the Dirac delta function. $p1_{start}$ and $p1_{end}$ is the first and last sample of p_1, respectively, and $p2_{start}$ and $p2_{end}$ is the first and last time point of p_2, respectively. Since p_1 and p_2 are separated by the pulse repetition interval (PRI), the relation between the time points of p_1 and p_2 can be described by equation (4.6).

$$p2_{start/end} = p1_{start/end} + PRI \qquad (4.6)$$

Once the time points of p_1 are selected, the accurate time points of p_2 can be identified based on equation (4.6). PI was calculated by adding p_1 and p_2 according to equation (4.1) and the linear signal cancellation of PI is defined as:

$$20 \times log_{10} \frac{max(|p_1|)}{max(|PI|)} \qquad (4.7)$$

For measuring LSC of AM, the whole nonlinear pulsing sequence at the imaging focus was recorded [P in **Fig. 4.1** (b)]. The interruption in **Fig. 4.1** (b) again indicates that the time between pulses is actually much longer. p_{even}, p_{full}, and p_{odd} in the pulsing sequence can be described in discrete form by equation (3.8), (3.9) and (3.10), respectively.

$$p_{even}[n] = \sum_{k=peven_{start}}^{peven_{end}} P[k]\,\delta[n-k] \qquad (4.8)$$

$$p_{full}[n] = \sum_{k=pfull_{start}}^{pfull_{end}} P[k]\,\delta[n-k] \qquad (4.9)$$

$$p_{odd}[n] = \sum_{k=podd_{start}}^{podd_{end}} P[k]\,\delta[n-k] \qquad (4.10)$$

As shown in **Fig. 4.1** (b), the relation between the time points of p_{even} and p_{full} can be described by equation (4.11) and the relation between the time points of p_{even} and p_{odd} can be described by equation (4.12).

$$pfull_{start/end} = peven_{start/end} + PRI \quad (4.11)$$

$$podd_{start/end} = peven_{start/end} + 2PRI \quad (4.12)$$

Once the time points of p_{even} are selected, the accurate time points of p_{full} and p_{odd} can be identified based on equation (4.11) and (4.12), respectively. AM was calculated by subtracting p_{even}, p_{full}, and p_{odd} according to equation (4.3) and the LSC of AM is defined as:

$$20 \times log_{10} \frac{max(|p_{full}|)}{max(|AM|)} \qquad (4.13)$$

Since the PRI was used to identify the precise time points (e.g., $p2_{start}$ and $p2_{end}$) of the transmitting event in a nonlinear pulsing sequence, it is necessary to know the precise PRI used in each system. However, we have observed a slight time shift (14-22 ns) between the programmed PRI in our Verasonics pulsing scheme and the corresponding PRI derived from the hydrophone measurements. An additional time shift was then applied on the programmed PRI to achieve maximum LSC. An example of how the time shift was identified is shown in **Fig. 3.4**, where (a) and (b) are waveforms without and with additional time shift on PRI, respectively, and (c) is the LSC of Verasonics scanner in PI mode as the time shift value changes. As shown in (c), additional time shift on the PRI allows higher LSC. The time shift value identified at 0.06 MI in each mode was used throughout other measurements at higher MI (0.10, 0.19, and 0.32). The PRI programmed for Verasonics scanner with L7-4 array in PI and AM mode were 150 μs; the PRI was 500 μs when imaging with C5-2 array. Our approach requires the PRI value to accurately isolate each transmit event from the pulsing sequence to calculate LSC. The time shift on PRI for L7-4 array in focused mode was 0.014 μs for both PI and AM, and 0.014 and 0.016 μs in plane wave mode for PI and AM, respectively. The time shift on PRI for C5-2 array in focused mode was 0.02 μs for both PI and AM, and 0.02 and 0.022 μs in diverging wave mode for PI and AM, respectively.

For the Philips scanner, we did not need to make any time shift adjustments as we were able to obtain an accurate PRI readout through a proprietary research interface. As seen in **Fig. 3.4** the maximal signal cancellation occurs at the zero time shift. This finding also holds when Philips iU22 scanner was operated in AM mode or with the C5-1 array.

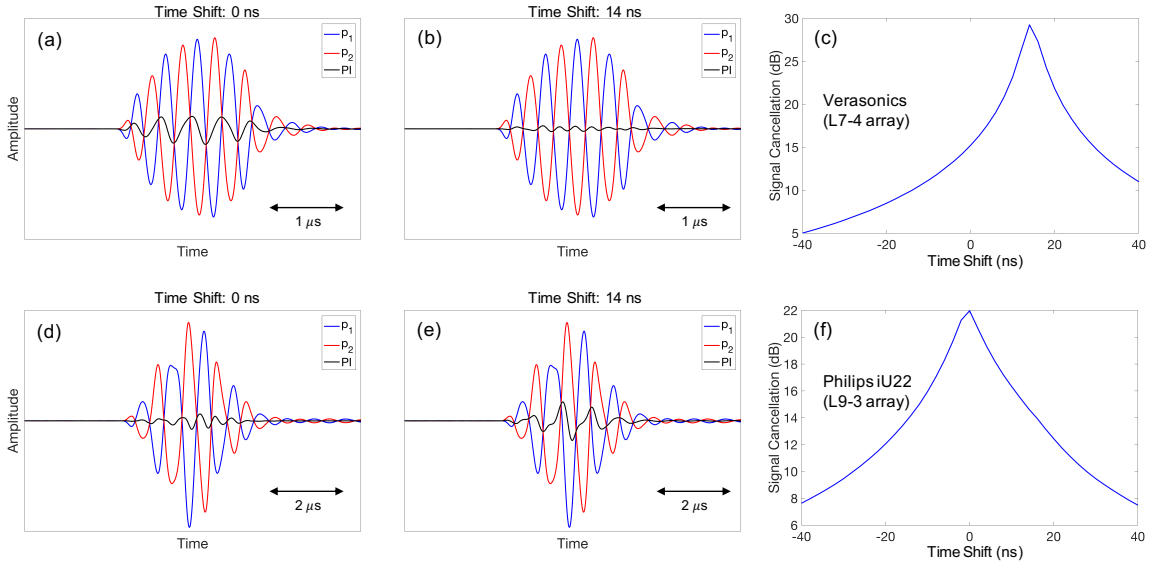

Fig. 4.4. Time shifting of the second PI pulse (blue) in order to correct for digitization errors due to asynchronous sampling clocks of the Verasonics and the oscilloscope. (a) Zero time shift, (b) 14 ns time shift, and (c) signal cancellation for all time shifts for the Verasonics and L7-4. (d) Zero time shift, (e) 14 ns time shift, and (f) signal cancellation for all time shifts for the Philips iU22 and L9-3.

4.2.5 *LSC from beamformed RF data*

With the hydrophone measurements, we are only able to evaluate the transmitted pulses and how well they cancel the linear signal in PI and AM. In order to evaluate the overall LSC (both while transmitting and while receiving), we tested the pulsing schemes on a simple wire phantom. The phantom consisted of a 19-gauge copper wire fixed across the sides of a rectangular container filled with water as shown in **Fig. 4.3** (b). While collecting RF data, we simply replaced the hydrophone with the wire phantom. The location of the wire in the image was adjusted by the motion stage and was placed at the imaging focus of the array. RF data from images were collected at the same imaging settings and MIs used when we collected the hydrophone data of the transmitted pulses as described in the previous section.

For both scanners, we collected and analyzed beamformed data and we were able to separate in the RF data the individual firings that were used for the pulsing schemes. Thus, PI and AM were calculated by adding and subtracting the beamformed echoes according to equation (4.1) and (4.3), respectively. The LSC of PI and AM were calculated according to equation (4.7) and (4.13) with the beamformed echoes, respectively.

4.3 RESULTS

4.3.1 *LSC derived from the hydrophone measurements of the pulses transmitted by the Verasonics*

The LSC of the pulse transmitted by the Verasonics scanner in water is shown in **Fig. 4.5**, where (a) and (b) show the results from the linear array in PI and AM mode and (c) and (d) the convex array. In blue we show the results when operating in conventional focused beamforming mode and in green in plane/diverging wave mode, for the 4 different MIs (voltages) considered. CEUS settings typically use low MIs (0.06-0.1) to avoid bubble destruction. At higher MI, not only there is more bubble destruction but there is also nonlinear propagation which distorts the pulses and reduces the signal cancellation due to the presence of nonlinear components. We are primarily interested in LSC at low MI's for practical purposes, but we also present LSC at higher MI's in our figures for the readers' reference. At the lower MIs (0.06-0.1), the highest LSC of PI is consistently lower than that of AM (29 vs. 40 dB). Also, the LSC was consistently slightly lower in plane/diverging wave mode.

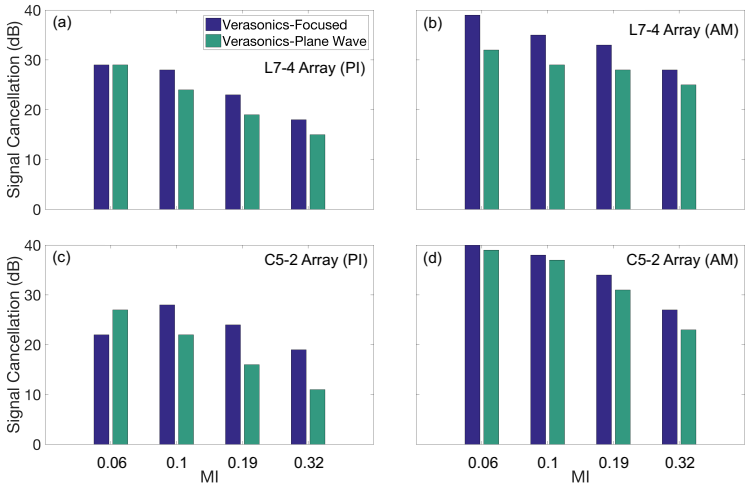

Fig. 4.5. Linear signal cancellation with a Verasonics scanner operating in either conventional focused (blue) or plane/diverging wave (green) mode from measured pulses in water transmitted by an L7-4 array for PI (a) and AM (b), and by a C5-2 array for PI (c) and AM (d).

4.3.2 *Comparing LSC from hydrophone measurements of the Verasonics with Philips iU22 scanner*

Next, we compared LSC between the Verasonics scanner and the Philips iU22 scanner both operating in conventional focused beamforming mode. We remind the reader that it is not possible to operate in plane/diverging wave mode on the Philips iU22 scanner. In **Fig. 4.6** we show in blue LSC with the Verasonics scanner and in red with the Philips iU22 scanner, for a linear array in PI (a), and in AM (b), and for a convex array in PI (c), and in AM (d). Paying attention only to the low MIs (0.06-0.1) where CEUS is performed and tissue harmonics are minimal, we observed that in PI the Philips iU22 scanner has a slightly lower LSC than the Verasonics scanner (22 vs 29 dB) for the linear array, but for the rest of the cases their LSC is very similar (difference is within 3 dB). We also note that the blue bars in **Fig. 4.6** are the same as the blue bars in **Fig. 4.5**. Finally, both scanners are able to perform AM with high LSC (typically around 40 dB) at low MI, as one can see from both **Fig. 4.5** and **Fig. 4.6**.

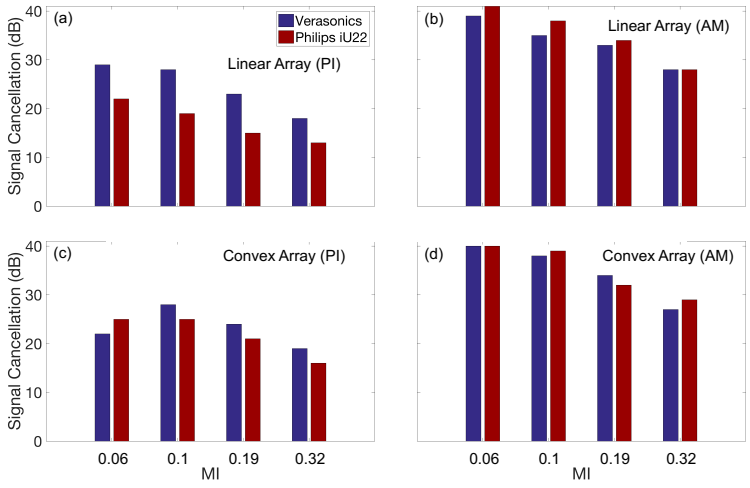

Fig. 4.6. Linear signal cancellation with a Verasonics (blue) and a Philips iU22 scanner (red) from measured pulses in water transmitted by a linear array in PI (a) and AM (b), and by a convex array in PI (c) and AM (d).

4.3.3 *LSC derived from the RF data of the Verasonics*

We also assessed the LSC from the combined transmit-receive process by collecting and analyzing RF data. **Fig. 4.7** (a) and (b) show the LSC with a linear array in PI and AM mode, respectively, and (c) and (d) with the convex array in PI and AM, respectively. In dotted blue, we show the

results from conventional focused beamforming mode, and in dotted green the results from plane/diverging wave mode. We observe that at low MI's (0.06 - 0.1) the highest LSC for PI is consistently lower than AM (37 vs. 43 dB for the linear array and (28 vs 46 dB) for the convex array. The LSC was also consistently slightly lower in plane/diverging wave mode.

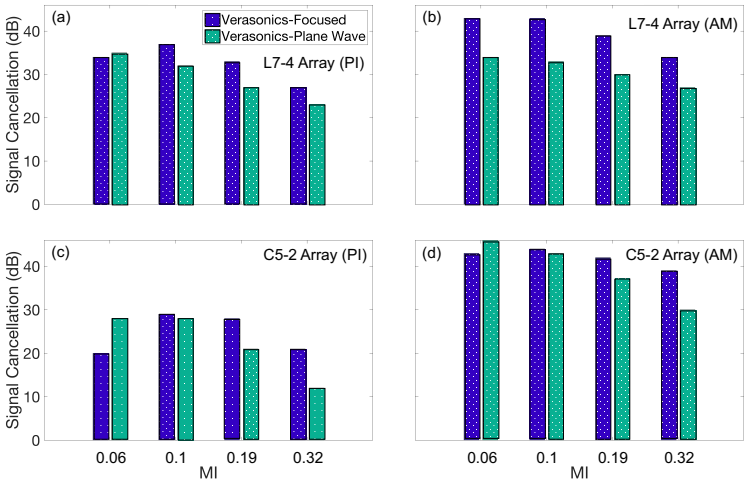

Fig. 4.7. Linear signal cancellation with a Verasonics scanner operating in either conventional focused (dotted blue) or plane/diverging wave (dotted green) mode from RF data collected with an L7-4 array for PI (a) and AM (b), and with a C5-2 array for PI (c) and AM (d).

4.3.4 *Comparing LSC from RF data of the Verasonics with Philips iU22 scanner*

In **Fig. 4.8** we compare the LSC from RF data between the Verasonics scanner (dotted blue) and the Philips iU22 (dotted red) scanner in conventional focused beamforming mode. **Fig. 4.8** (a)-(b) show the LSCs for the linear arrays in PI and AM, respectively, and **Fig. 4.8** (c)-(d) the convex array counterpart. It is evident from this figure that at lower MI's (0.06 - 0.1), the LSC of PI is lower for Philips iU22 scanner than the Verasonics (19 vs 37 dB) when using the linear array (**Fig. 4.8** (c)). For the rest of the cases, the two scanners have very similar LSC performance. Of note, we observed a similar trend in **Fig. 4.8**.

Based on the results in **Fig. 4.7** and **Fig. 4.8**, both scanners perform AM with a higher LSC than PI, as also supported by our hydrophone measurements.

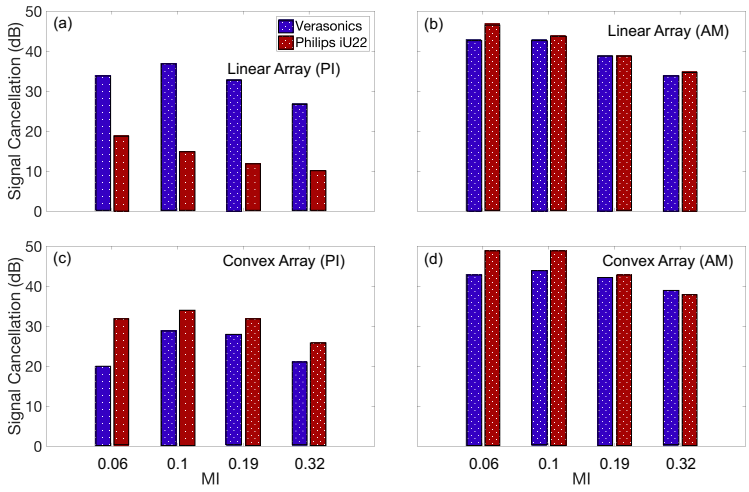

Fig. 4.8. Linear signal cancellation with a Verasonics (dotted blue) and a Philips iU22 scanner (dotted red) from RF data collected with a linear array in PI (a) and AM (b), and with a convex array in PI (c) and AM (d).

4.4 DISCUSSION

4.4.1 *Considerations for measuring linear signal cancellation*

To accurately measure the LSC performance of a scanner, it is necessary to measure their transmitted pulses in a setting that closely resembles a normal scan sequence. Therefore, instead of recording the individual transmit events in the nonlinear pulsing sequence (e.g., p_1 in PI) with separate triggers, the whole nonlinear pulsing sequence was recorded with a single trigger. Each transmit event in the nonlinear pulsing sequence was then isolated with the method described in Methods. Additionally, all lines of a frame were transmitted [39] to resemble a real imaging scenario instead of transmitting the same line repeatedly, which is possible with the Verasonics.

Another key aspect for measurements is to identify the time shift on the PRI of the scanner in each mode to accurately separate each transmit event in the nonlinear pulsing sequence. Philips iU22 scanner outputs the precise value of the PRI through a research interface. The PRI of the Verasonics was always slightly different (by 14-22 *n*s) from what is programmed in the script, which could potentially affect the LSC results significantly. The time shift was identified at the lowest MI (0.06) because the waveform is less distorted by nonlinear propagation compared to the waveform at higher MIs. The time shift values were consistent throughout the various imaging modes and were mainly dependent on the type of array that was used for imaging. The time shift

values were around 14 *ns* for the L7-4 array and 20 *n*s for the C5-2 array. The fact that no time shift was necessary for RF data and the LSC values were roughly the same between hydrophone measurements and RF data, suggests that the need of the time shift is justified and the time shift may be caused by the measurement process.

4.4.2 *Assessing linear signal cancellation in transmitted pulses*

The LSC of the pulse transmitted by the Verasonics scanner is 3-18 dB higher in AM mode than in PI mode, as shown in **Fig. 4.5**. This may be attributed to the fact that PI requires high precision from the function generator of the scanner to invert the pulse so that there is no asymmetry between inverted pulses [24]. However, AM is less demanding on the hardware than PI since it only requires the elements to be turned on and off in each transmit. As a result, it is reasonable and expected that the LSC is higher for AM than PI. The higher LSC in AM also suggests that AM may be preferred over PI in CEUS cases where more complete elimination of tissue is necessary, for example capturing complete washout of a liver tumor.

Comparing the LSC performance of focused beamforming mode to the LSC performance of plane/diverging wave mode, we observed that the LSC was consistently slightly lower in plane/diverging wave mode. According to a previous study, the cross talk between on and off array elements may compromise the degree of LSC in AM mode [24]. Since more array elements were used for each transmit in plane/diverging wave mode, the LSC in plane/diverging wave mode may be lower than that in focused beamforming mode. However, these factors are highly dependent on the array that is used, which explains why the L7-4 array is more susceptible to cross talk than C5-2 array.

It was important to observe that the LSC of the Verasonics and the Philips iU22 was very similar. Both scanners achieved comparable LSC in focused AM mode. At the lowest MI, both scanners achieved high LSC around 40 dB with either of the arrays. When the Verasonics scanner was operated in focused PI mode, the highest LSC it achieved was 28-29 dB (dependent on which array was used), comparable to the LSC values observed in other scanners in PI mode [34, 35] and the LSC value achieved by a focused single-element transducer with a function generator programed for a PI sequence [40]. In addition, the LSC of the transmitted pulse by the Verasonics scanner

was on average 4 dB higher than that of the Philips iU22 scanner in focused PI mode. This difference in LSC performance may be attributed to the difference in the ability of the two scanners' built-in function generators to form pulses. Since AM is less hardware-demanding than PI, it was expected that the difference in the LSC between the two scanners was less in AM than in PI mode.

4.4.3 *Assessing linear signal cancellation from received RF data*

As shown in **Fig. 4.5**-**Fig. 4.8**, the LSC calculated from the RF data has a trend similar to the LSC derived from the hydrophone measurements, where the LSC for the AM mode is consistently higher than the PI mode. Interestingly, we observed that the LSC from the RF data was on average slightly higher than the hydrophone measurements. This difference may be a result of the frequency response of the array that was used for receiving. To test this hypothesis, two Parks-McClellan bandpass filters [41] that matched the frequency response of the L7-4 or C5-2 array were designed. The waveforms from the hydrophone measurement were filtered with the Parks-McClellan bandpass filters to adjust the amplitude in frequency domain for recalculation of the LSC. For simplicity, we only show the frequency weighted LSC for L7-4 array in focused PI mode in **Fig. 4.9**, where it shows the difference of the LSC between the hydrophone measurement and the RF data is clearly reduced after filtering. **Fig. 4.9** indicates that the difference of the LSC between the hydrophone measurement and RF data may be partly due to the frequency response of the array that was used for receiving. Despite the small differences, the LSC values observed from the RF data are still comparable to that from the hydrophone measurements.

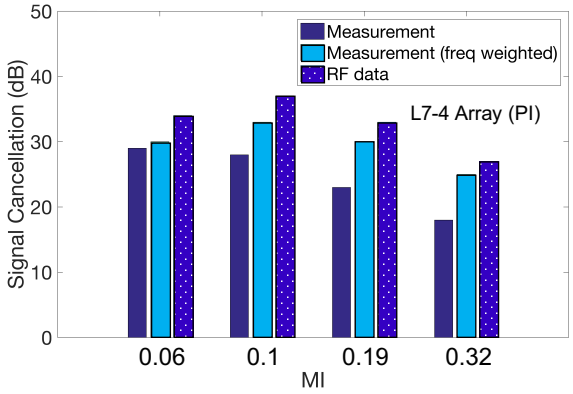

Fig. 4.9. Linear signal cancellation from hydrophone measurement (blue), hydrophone measurement after frequency adjustment (light blue), and RF data (dotted blue) of a Verasonics scanner with a L7-4 array in focused PI mode.

A possible study limitation is the variability from a scanner to scanner (of the same type) which we have not performed. Another possible limitation is that the total number of arrays that were measured in this study was small.

4.5 CONCLUSION

We have investigated the LSC performance of the Verasonics scanner and compared it with that of a clinical scanner (Philips iU22). The LSC performance of each scanner was assessed separately for the transmit path by measuring the transmitted pulses in water and for the combined transmit-receive path by analyzing the beamformed RF data. At low MI (≤0.1), both scanners had a greater LSC in AM (~40 dB) than PI (~29 dB). For the Verasonics scanner, the LSC was generally lower in plane/diverging wave mode than in conventional focused mode. At higher MIs, the LSC was reduced as a result of nonlinear propagation. The Verasonics scanner and the Philips iU22 scanner achieved comparable LSC in focused AM mode at low MI. In PI, the Verasonics scanner achieved on average 4 dB better LSC than the Philips iU22 scanner. AM may be preferred over PI when the clinical application requires high bubble specificity due to having a lower LSC.

4.6 ACKNOWLEDGEMENTS

The research reported in this study was supported by the National Institute of Biomedical Imaging and Bioengineering of the National Institutes of Health under Award Number T32EB001650. We would like to thank Dr. Alicia Clark and Eric Juang for their comments on the manuscript.

4.7 REFERENCES

[1] H. Becher and P. N. Burns, *Handbook of contrast echocardiography: Left ventricular function and myocardial perfusion*. Springer Science & Business Media, 2012.

[2] S. R. Wilson, P. N. Burns, D. Muradali, J. A. Wilson, and X. Lai, "Harmonic hepatic US with microbubble contrast agent: initial experience showing improved characterization of hemangioma, hepatocellular carcinoma, and metastasis," *Radiology,* vol. 215, no. 1, pp. 153-161, 2000.

[3] T. Leighton, *The acoustic bubble*. Academic press, 2012.

[4] C. F. Dietrich *et al.*, "How to perform contrast-enhanced ultrasound (CEUS)," *Ultrasound international open,* vol. 4, no. 01, pp. E2-E15, 2018.

[5] M. F. Hamilton and D. T. Blackstock, *Nonlinear acoustics*. Academic press San Diego, 1998.

[6] P. Burns, "Harmonic imaging with ultrasound contrast agents," *Clin Radiol,* vol. 51, pp. 50-55, 1996.

[7] M. A. Averkiou, D. N. Roundhill, and J. E. Powers, "A new imaging technique based on the nonlinear properties of tissues," in *Ultrasonics Symposium*, 1997, vol. 2, pp. 1561-1566: INSTITUTE OF ELECTRICAL & ELECTRONICS ENGINEERS INC.

[8] M. A. Averkiou, M. F. Bruce, J. E. Powers, P. S. Sheeran, and P. N. Burns, "Imaging Methods for Ultrasound Contrast Agents," *Ultrasound in Medicine & Biology,* 2019.

[9] T. A. Whittingham, "Contrast-specific imaging techniques: technical perspective," in *Contrast media in ultrasonography*: Springer, 2005, pp. 43-70.

[10] M. A. Averkiou, C. Mannaris, M. Bruce, and J. Powers, "Nonlinear pulsing schemes for the detection of ultrasound contrast agents," *Journal of the Acoustical Society of America,* vol. 123, no. 5, p. 3110, 2008.

[11] D. H. Simpson, C. T. Chin, and P. N. Burns, "Pulse inversion Doppler: a new method for detecting nonlinear echoes from microbubble contrast agents," *IEEE transactions on ultrasonics, ferroelectrics, and frequency control,* vol. 46, no. 2, pp. 372-382, 1999.

[12] G. A. Brock-Fisher, M. D. Poland, and P. G. Rafter, "Means for increasing sensitivity in non-linear ultrasound imaging systems," ed: Google Patents, 1996.

[13] V. Mor-Avi, E. G. Caiani, K. A. Collins, C. E. Korcarz, J. E. Bednarz, and R. M. Lang, "Combined assessment of myocardial perfusion and regional left ventricular function by analysis of contrast-enhanced power modulation images," *Circulation,* vol. 104, no. 3, pp. 352-357, 2001.

[14] E. Boni, C. Alfred, S. Freear, J. A. Jensen, and P. Tortoli, "Ultrasound open platforms for next-generation imaging technique development," *IEEE transactions on ultrasonics, ferroelectrics, and frequency control,* vol. 65, no. 7, pp. 1078-1092, 2018.

[15] P. Song *et al.*, "Improved super-resolution ultrasound microvessel imaging with spatiotemporal nonlocal means filtering and bipartite graph-based microbubble tracking,"

IEEE transactions on ultrasonics, ferroelectrics, and frequency control, vol. 65, no. 2, pp. 149-167, 2017.

[16] C. H. Leow, E. Bazigou, R. J. Eckersley, C. Alfred, P. D. Weinberg, and M.-X. Tang, "Flow velocity mapping using contrast enhanced high-frame-rate plane wave ultrasound and image tracking: Methods and initial in vitro and in vivo evaluation," *Ultrasound in medicine & biology,* vol. 41, no. 11, pp. 2913-2925, 2015.

[17] C. Tremblay-Darveau *et al.*, "The role of microbubble echo phase lag in multipulse contrast-enhanced ultrasound imaging," *IEEE transactions on ultrasonics, ferroelectrics, and frequency control,* vol. 65, no. 8, pp. 1389-1401, 2018.

[18] C. Tremblay-Darveau, "Contrast-enhanced Doppler ultrasound imaging using plane waves," 2016.

[19] P. Jiang, Z. Mao, and J. Lazenby, "A new tissue harmonic imaging scheme with better fundamental frequency cancellation and higher signal-to-noise ratio," in *1998 IEEE Ultrasonics Symposium. Proceedings (Cat. No. 98CH36102)*, 1998, vol. 2, pp. 1589-1594: IEEE.

[20] M. A. Averkiou, "Tissue harmonic ultrasonic imaging," *Comptes Rendus de l'Académie des Sciences-Series IV-Physics,* vol. 2, no. 8, pp. 1139-1151, 2001.

[21] O. Couture, M. Fink, and M. Tanter, "Ultrasound contrast plane wave imaging," *IEEE transactions on ultrasonics, ferroelectrics, and frequency control,* vol. 59, no. 12, pp. 2676-2683, 2012.

[22] P. Phillips and E. Gardner, "Contrast-agent detection and quantification," *European radiology,* vol. 14, pp. P4-10, 2004.

[23] G. Harris, S. Maruvada, and P. Gammell, "Two efficient methods for measuring hydrophone frequency response in the 100 kHz to 2 MHz range," in *Journal of Physics: Conference Series*, 2004, vol. 1, no. 1, p. 26: IOP Publishing.

[24] T. L. Szabo, *Diagnostic ultrasound imaging: inside out*. Academic Press, 2004.

[25] A. N. Pouliopoulos, M. T. Burgess, and E. E. Konofagou, "Pulse inversion enhances the passive mapping of microbubble-based ultrasound therapy," *Applied physics letters,* vol. 113, no. 4, p. 044102, 2018.

[26] T. W. Parks and C. S. Burrus, *Digital filter design*. Wiley-Interscience, 1987.

Chapter 5. INVESTIGATION OF THE PHASE OF NONLINEAR ECHOES FROM MICROBUBBLES DURING AMPLITUDE MODULATION

Sara B. Keller, Ting Yu Lai, Lance De Koninck, Michalakis A. Averkiou

Abstract

Contrast-enhanced ultrasound imaging relies on distinguishing between microbubble and tissue echoes. Amplitude modulation, a nonlinear pulsing scheme, has been developed to take advantage of amplitude-dependent nonlinearity of microbubble echoes. However, with amplitude modulation, tissue can also generate harmonics that can degrade image contrast. Segmentation of contrast-enhanced ultrasound images based on amplitude-dependent phase difference in the echoes, defined in the present manuscript as $\Delta\Phi_{AM}$, has been proposed as an additional method of enhancing contrast-to-tissue ratio as tissue is not expected to create the same degree of $\Delta\Phi_{AM}$; however, this has not been robustly investigated. In this work, we evaluate the source of $\Delta\Phi_{AM}$ through simulations of unshelled versus shelled microbubble oscillation and simulations of nonlinear propagation in tissue. We then validate the simulated $\Delta\Phi_{AM}$ results with experimental $\Delta\Phi_{AM}$ measurements during *in vitro* scattering and imaging in a flow phantom. We show that shelled and unshelled microbubbles resulted in a $\Delta\Phi_{AM}$ with similar overall magnitude with some differences in trends, and that tissue echoes have a small yet detectable degree of $\Delta\Phi_{AM}$ due to nonlinear propagation. The results from this work can help inform optimal parameter selection for phase segmentation and implementation on clinical scanner.

Adapted from Keller, SB et al. "Investigation of the Phase of Nonlinear Echoes from Microbubbles during Amplitude Modulation." IEEE Trans. Ultrason. Ferroelectr. Freq. Control., In review

5.1 INTRODUCTION

Contrast enhanced ultrasound (CEUS) has emerged as an important tool for evaluating vascular beds. Microbubble ultrasound contrast agents are similar in size to red blood cells which allows them to provide contrast enhancement in both capillaries and large blood vessels [1], [2] . Due to their unique nonlinear scattering properties, microbubble signal can be distinguished from tissue signal, and therefore make an excellent diagnostic tool for observing real-time vascular structure and blood perfusion [1], [3], [4].

Microbubble contrast during CEUS is a result of microbubble echoes being nonlinear and containing harmonic components in their spectra while tissue echoes are mostly linear [1], [5]. The degree of nonlinearity is dependent on the amplitude of the ultrasound wave; higher amplitudes result in a greater nonlinear response [6]. In order to isolate the unique frequency components of microbubble echoes, nonlinear pulsing schemes including pulse inversion (PI), amplitude modulation (AM), and amplitude modulated pulse inversion (AMPI) have been developed [1], [5], [6]. Tissue signal suppression is important in CEUS to achieve good image contrast and microbubble specificity [7]. Incomplete tissue signal cancellation may mask real enhancement caused by microbubbles or be incorrectly interpreted as real enhancement [1]. Previous studies have shown that due to hardware issues AM has better tissue signal suppression than PI [1], [8], [9]. For this work, we focus on AM, a nonlinear pulsing scheme that involves transmitting 2 or more pulses at different amplitudes. A widely used version of AM is one where the amplitude of the second pulse (p_{half}) is half that of the first pulse (p_{full}). The linear response in the echoes is removed by scaling the echoes of p_{half} by a factor of 2 and then subtracting them from the echoes of p_{full} [1].

The image quality of CEUS is also limited by the tissue harmonics generated from the nonlinear propagation of sound waves in tissue. Optimal CEUS imaging is performed at low mechanical index (MI $\leq$0.1) to avoid microbubble destruction and the generation of tissue harmonics, which may interfere with or mask the microbubble signals in CEUS images [10]. However, even at low Mis and especially at higher frequencies, tissue still generates some nonlinear response, which degrades the overall contrast-to-tissue ratio (CTR) of CEUS [11], [12]. Recently, it has been

proposed that utilizing other unique microbubble echo signal properties could be used as an additional method of tissue signal suppression during AM imaging. Particularly, it has been shown that microbubble echoes not only exhibit amplitude-dependent nonlinearity, but also an amplitude-dependent difference in phase during AM imaging. We refer to this phase difference as $\Delta\Phi_{AM}$, which is the difference in phase between the echoes of p_{full} and p_{half}. Using a pre-determined $\Delta\Phi_{AM}$ as a threshold for image segmentation has been used to improve the CTR of CEUS images, as AM sequences in tissue are not expected to result in the same degree of $\Delta\Phi_{AM}$ [13]. Tremblay-Darveau, et al. posited that $\Delta\Phi_{AM}$ is a result of the buckling dynamics of shelled microbubbles, which was demonstrated with the Marmottant model [13], [14]. Additionally, they found that $\Delta\Phi_{AM}$ was generally negative, indicating the phase of the echo from p_{full} lags that of p_{half} [13]. According to Tremblay-Darveau, since $\Delta\Phi_{AM}$ is attributed to the bubble shell, it is not expected to occur in tissue or in unshelled bubbles.

We hypothesize, however, that $\Delta\Phi_{AM}$ may also occur to some degree during nonlinear propagation in tissue and nonlinear oscillations of the gas core itself in addition to the impact of shell properties. To the best of our knowledge, $\Delta\Phi_{AM}$ resulting from nonlinear propagation and echoes from unshelled microbubbles (derived from simulations) have not yet been reported. We believe that a robust analysis of the source of $\Delta\Phi_{AM}$ could help derive optimal conditions for phase segmentation. We evaluate this through simulations of unshelled versus shelled microbubble oscillation with the Rayleigh-Plesset [15] and Marmottant equations [14], respectively and simulations of nonlinear propagation in tissue with the Khokhlov-Zabolotskaya-Kuznetsov (KZK) equation [16], [17]. We then validate the simulated $\Delta\Phi_{AM}$ results with experimental $\Delta\Phi_{AM}$ measurements during *in vitro* scattering and AM imaging in a flow phantom. We performed these experiments on three commercially available ultrasound contrast agents: Optison, Sonazoid, and Sonovue, to evaluate the impact of various microbubble formulations on $\Delta\Phi_{AM}$. The results from this work further elucidate the source of $\Delta\Phi_{AM}$ which can both improve phase segmentation to increase CTR during AM imaging and even raise the possibility of implementing phase segmentation on imaging applications outside of CEUS.

5.1 THEORY

5.1.1 *Phase calculations*

All simulated and experimentally captured waveforms were analyzed using the following methodology. For the echoes from the p_{full} and p_{half} pair (referred to as an AM echo pair), the waveforms were first filtered using an FIR bandpass filter centered around the center frequency of the transmit pulse, as we chose to evaluate phase at the fundamental frequency [13]. The filtered pulses were then converted to their analytic signal using a Hilbert Transform, which resulted in waveforms that contained both real and imaginary components. Phase at each time point for each waveform in the AM pair was then calculated as follows,

$$\Phi_{full}(t) = \angle ps_{full}(t) \text{ (5.1)}$$

$$\Phi_{half}(t) = \angle ps_{half}(t), \text{ (5.2)}$$

where $\angle$ is the "angle" operator on the analytic signals. $ps_{full}(t)$ and $ps_{half}(t)$ are the echoes of p_{full} and p_{half} at each time point, respectively. The difference in phase, $\Delta\Phi_{AM}(t)$, between the AM pair was calculated at each time point,

$$\Delta\Phi_{AM}(t) = \Phi_{full}(t) - \Phi_{half}(t) \text{ (5.3)}$$

and then averaged over the pulse duration to get a single value of $\Delta\Phi_{AM}$ for each AM pair. This signal processing method for calculating $\Delta\Phi_{AM}$ was used for all subsequent phase analyses.

5.1.2 *Rayleigh-Plesset model for unshelled bubbles*

Unshelled bubble nonlinear oscillation was modeled with the Rayleigh-Plesset equation [18],

$$\rho_L\left(R\ddot{R} + \tfrac{3}{2}\dot{R}^2\right) = \left(P_0 + \tfrac{2\sigma_W}{R_0}\right)\left(\tfrac{R_0}{R}\right)^{3\kappa}\left(1 - \tfrac{3\kappa\dot{R}}{c}\right) - \tfrac{2\sigma_W}{R} - \tfrac{4\mu_L\dot{R}}{R} - P_0 - P_A(t), \text{ (5.4)}$$

where $R(t)$ is the microbubble radius, ρ_L is the liquid density, P_0 is the static fluid pressure, σ is the surface tension, R_0 is the equilibrium radius, κ is the polytropic gas constant, c is the speed of sound, μ_L is the liquid viscosity and $P_A(t)$ is the applied pressure (ie, the ultrasound pressure).

Microbubble radial oscillation from unshelled bubbles insonified with a 1.7 MHz, 4-cycle pulse with pressures ranging from 0.005 to 0.2 MPa was modeled. The simulation parameters were as follows: ρ_L = 1000 kg/m^3, P_0 = 100 kPa, σ_w = 0.0725 N/m, κ = 1.1, c = 1486 m/s, μ_L = 0.001 Pa·s for microbubble radii (R_0) spanning from 0.5 to 3 μm. Radial oscillation was converted to scattered pressure (p_s) using the following equation:

$$p_s = \frac{\rho_L R}{r}(2\dot{R} + R\ddot{R}). \quad (5.5)$$

Finally, $\Delta\Phi_{AM}$ of all AM pairs was calculated using the methodology described in **Section 5.1.1**.

5.1.3 *Marmottant Model for Shelled Bubbles*

Shelled microbubble oscillation was modeled with the Marmottant Equation, which is merely the Rayleigh-Plesset equation with added surface tension terms [14]:

$$\rho_L\left(R\ddot{R} + \tfrac{3}{2}\dot{R}^2\right) = \left(P_0 + \tfrac{2\sigma(R_0)}{R_0}\right)\left(\tfrac{R_0}{R}\right)^{3\kappa}\left(1 - \tfrac{3\kappa\dot{R}}{c}\right) - \tfrac{2\chi}{R}\left(\tfrac{R^2}{{R_0}^2} - 1\right) - \tfrac{4\mu_L\dot{R}}{R} - \tfrac{4\kappa_S\dot{R}}{R^2} - P_0 - P_A(t) \quad (5.6)$$

Where κ_s is the shell viscosity, χ is the shell elasticity, and $\sigma(R)$ is the spatially varying surface tension at the bubble wall, is defined by [14]

$$\sigma(R) = \begin{cases} 0, & R < R_{buck} \\ \chi_0\left(\frac{R^2}{R_{buck}} - 1\right), & R_{buck} < R < R_{break} \\ \sigma_w, & R > R_{break} \end{cases}, \quad (5.7)$$

where R_{buck} and R_{break} define the buckle and rupture radius of the microbubble shell, respectively.

The same parameters were used to simulate the shelled bubbles as the free gas bubbles, with the addition of κ_s = 1.5 × 10^{-8} kg/s and χ = 1.55. R_{buck} and R_{break} were defined to be 99% and 102% of

the starting radius, respectively. $\Delta\Phi_{AM}$ of all AM pairs was calculated using the methodology described in **Section 5.1.1**.

5.1.4 *Nonlinear parabolic wave equation (KZK equation)*

The KZK nonlinear parabolic wave equation has been used to model the nonlinear propagation of finite amplitude pulses from focused sound beams in thermoviscous fluids [19]–[21]. $\Delta\Phi_{AM}$ due to nonlinear propagation was evaluated by considering the phases of the propagated pulses at different amplitudes and assuming that the tissue echoes would be similar due to linear tissue scattering. More details of the numerical model were presented previously [22].

The assumed source in the simulations was a focused circular source with a radius of 8.6 mm and a focal length of 70 mm. A 4-cycle pulse at 2 MHz was transmitted with source pressures ranging from 0.04 to 1.2 MPa. The nonlinearly propagated pulses at three different axial locations, defined in relation to the focal length, σ (0.5σ, 1σ, and 1.5σ) were recorded for each AM pair. We used the following acoustic parameters for nonlinear simulations in tissue: speed of sound $c = 1540\ \mathrm{m/s}$, density $\rho = 1000\ \mathrm{kg/m^3}$, absorption coefficient of 0.3 dB/cm at 1 MHz, and nonlinearity coefficient $\beta = 5$.

$\Delta\Phi_{AM}$ of all AM pairs was calculated using the methodology described in **Section 5.1.1**. To highlight the dependence of axial distance on harmonic phase content, the absolute phase (not $\Delta\Phi_{AM}$) of a pulse, with a source pressure of 1.2 MPa, as it propagates along the source axis was calculated from the FFT of the waveform.

5.2 MATERIALS AND METHODS

In order to validate the theoretical results, $\Delta\Phi_{AM}$ was measured both using single element transducers in an in vitro scattering experiment and a clinical scanner while scanning microbubbles flowing in a tissue flow phantom. For all experiments, Sonovue (Bracco Suisse SA, Geneva, Switzerland), Sonazoid (GE Healthcare, Chicago, IL, USA), and Optison (GE Healthcare, Chicago, IL, USA) were resuspended according to the manufacturer's instructions. Microbubble

concentration from the vials was estimated from our previous study to be between 1-5 × 10^8 microbubbles/mL for all formulations [23].

5.2.1 In vitro *microbubble scattering*

The experimental setup used for microbubble scattering experiments can be seen in **Fig. 5.1**. A Tektronix AFG 3102C Arbitrary Waveform Generator was used to generate each AM pair. This was accomplished by utilizing both Channel 1 for p_{full} and Channel 2 connected to the 'Add Input' connection on the back of the oscilloscope for p_{half}. The p_{half} was sent after a 500 µs time delay to mimic an average pulse repetition frequency of imaging systems. The p_{full} and delayed p_{half} were sent through an ENI 2200L RF Amplifier (ENI, Rochester, NY). This signal was then sent to a focused transducer (V304, diameter = 2.54 cm, focal distance = 7.6 cm, center frequency = 2.25 MHz, Olympus NDT, Waltham, MA, USA), which was used as the source of microbubble excitation. This transducer was operated at a frequency of 1.7 MHz. A focused transducer (C304, diameter = 2.54 cm, focal distance = 7.6 cm, center frequency = 2.25 MHz, Olympus NDT, Waltham, MA, USA) was confocally aligned at a 90° angle with the V304 and recorded scattered microbubble echoes.

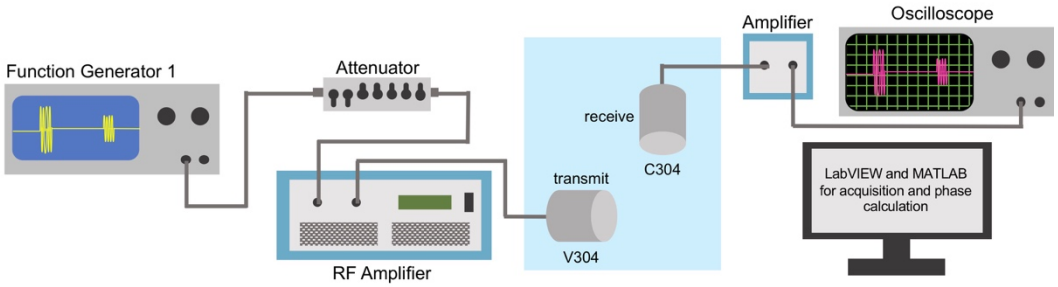

Fig. 5.1: Experimental setup for in vitro scattering.

Microbubbles were added directly into the water tank at a concentration of 10^4 microbubbles/mL, consistent with our prior work [23]. For each experiment, a new vial of microbubbles was used, and microbubble presence was confirmed through observation of scattered signal. The p_{full} and p_{half} pulse sequences were sent through the V304 at acoustic pressures ranging from 40 kPa (the smallest p_{half}) to 160 kPa (the largest p_{full}). The signals were then received by the C308, amplified by 20 dB using a variable gain pulser-receiver (Panametrics, Waltham, MA, USA), and

digitized using a DPO7054C Oscilloscope (Tektronix Inc., Beaverton, OR) with a sampling frequency of 500 MHz. A custom LabVIEW program was used to acquire 20 echoes per pressure setting. Calculation of $\Delta\Phi_{AM}$ was performed in MATLAB (The MathWorks, Inc., Natick, MA, USA) as described in **Section 5.1.1**; however, only scattered pulses with an amplitude three times above noise were evaluated, in order to ensure sufficient signal-to-noise ratio. Noise in this case was defined as the average amplitude between a section of the received voltage signal in which scattering was not occurring. For comparison against a control, a 0.5 mm x 0.5 mm metal reflector was placed at the confocal area of both transducers. Reflection of sound off the reflector is not expected to generate $\Delta\Phi_{AM}$ at low excitation pressures.

5.2.2 *RF data acquisition in a flow phantom*

A Doppler flow phantom (Model 5230A-modified, ATS Laboratories, Bridgeport, CT) was connected to a flow system in a closed-loop setup, as seen in **Fig. 5.2**. A 1 L beaker filled with deionized water was connected to the system via ¼ inch inner diameter tygon silicon tubing that ran through a peristaltic pump system consisting of a Masterflex L/S Variable Drive (Model 07528, Cole Parmer, Vernon Hills, IL) and Easy-Load II pump head (Model 77200-62, Cole Parmer). The beaker was placed on a stir-plate with magnetic stirrer (ThermoFisher Scientific, Waltham, MA) to ensure appropriate microbubble mixing. Sonovue, Sonazoid, and Optison were added into the beaker at a dilution factor of 1:100,000. Two imaging transducers, the C5-1 and L12-5, operated by the Philips iU22 (Philips Healthcare, Bothell, WA) were coupled to the tissue phantom with ultrasound gel. The C5-1 and L12-5 transducers were operating in an AM contrast mode, using 3 pulses at a center frequency of 1.7 MHz and 4.1 MHz, respectively. Mechanical indexes (MIs) ranging from 0.06 to 0.21 were used. RF data were acquired using specialized research settings. For each microbubble formulation and pressure, three RF frames were taken. The microbubbles were allowed to flow between each frame acquisition to limit microbubble destruction after one frame; however, the microbubbles were stationary during the acquisition to limit phase shift due to motion.

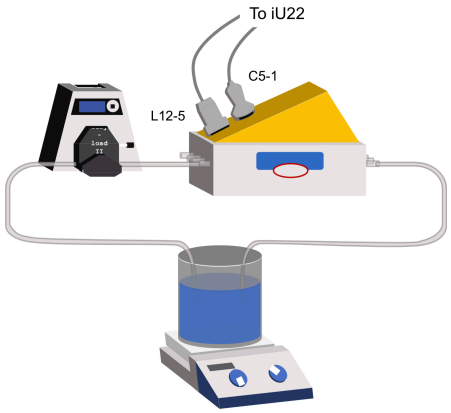

Fig. 5.2: Experimental setup for RF data acquisition of microbubbles in a flow phantom.

The RF data were imported into MATLAB for offline processing. RF data consist of post-beamformed imaging lines acquired prior to envelope detection and log-compression. Two regions of interest (ROIs) were created to evaluate $\Delta\Phi_{AM}$: one ROI within the tube (indicating microbubble signal) and one ROI above the tube (indicating tissue signal). $\Delta\Phi_{AM}$ was first calculated between a start and end time index (describing the depth of the ROI) as described in **Section 5.1.1** and then averaged over a start and end line index (describing the width of the ROI). Finally, $\Delta\Phi_{AM}$ was averaged over three frames for each MI tested.

5.3 RESULTS

5.3.1 $\Delta\Phi_{AM}$ *from unshelled and shelled bubbles*

Example radius- and scattered pressure-versus-time curves for unshelled bubbles generated by the Rayleigh-Plesset equation and for shelled bubbles generated by the Marmottant equation may be seen in **Fig. 5.3**. These results are from a 1, 2, and 3 μm radius bubble excited at 1.7 MHz. Just 0.04 and 0.08 MPa excitations are shown for simplicity. In **Fig. 5.4** we show the $\Delta\Phi_{AM}$ resulting from these bubble radii with all the pressure cases considered. Both shelled and unshelled bubbles exhibit a negative $\Delta\Phi_{AM}$, consistent with prior work. Furthermore, both shelled and unshelled bubbles show a $\Delta\Phi_{AM}$ with magnitude exceeding what has been previously used for phase segmentation (0.1-0.3 rad) [13]. However, where the $\Delta\Phi_{AM}$ of the unshelled bubble seems mostly dependent on pressure, the $\Delta\Phi_{AM}$ from the shelled bubble seems to be more heavily dependent on bubble radius, and indeed shows that lower acoustic pressures and larger bubble radii give a greater

$\Delta\Phi_{AM}$. These results may also be visualized in the 2D plots shown in **Fig. 5.5**, in which a range of bubble radii were evaluated. In these maps, a greater magnitude $\Delta\Phi_{AM}$ is indicated by a yellow color. Notably, the resonance size of a free bubble excited at 1.7 MHz is about 1.5 μm in radius, calculated using the Minnaert formula [24]. This is consistent with the free bubble results showing that midrange radii have the largest $\Delta\Phi_{AM}$ (a) but are otherwise dependent on acoustic pressure. The $\Delta\Phi_{AM}$ resulting from shelled bubbles seems more prominent at larger radii and small acoustic pressures for this driving frequency (b), as in **Fig. 5.4**, which we attributed to the fact that shelled microbubbles are resonant at larger radii.

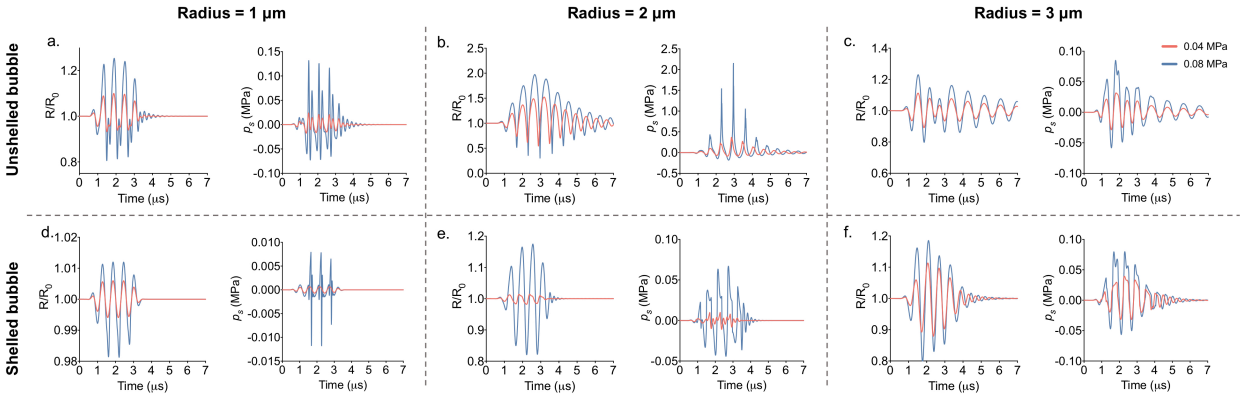

Fig. 5.3: Example radius- and scattered pressure (p_s)-versus time curves from 1, 2, and 3 μm radius unshelled or shelled bubbles with 0.04 and 0.08 MPa pressures. Visible $\Delta\Phi_{AM}$ can be observed in several cases, such as (b) and (f).

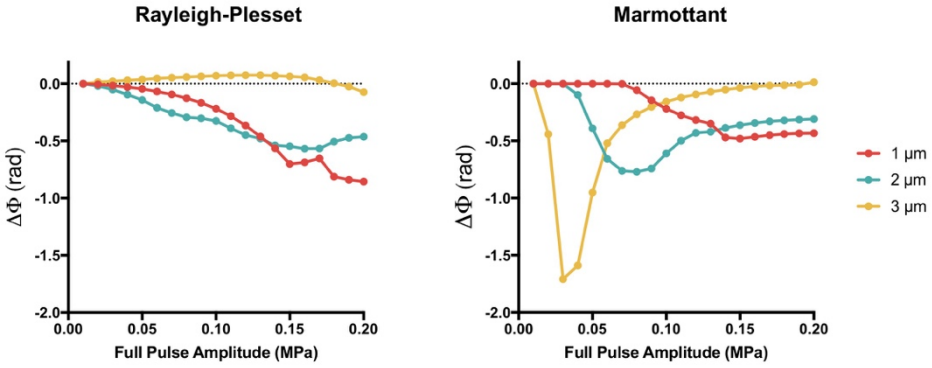

Fig. 5.4: $\Delta\Phi_{AM}$ as a function of the full pulse amplitude. The unshelled bubbles considered exhibit $\Delta\Phi_{AM}$ that mainly increases with increasing pressure, while the shelled bubbles exhibit $\Delta\Phi_{AM}$ that is more prominent at large radii and small pressures.

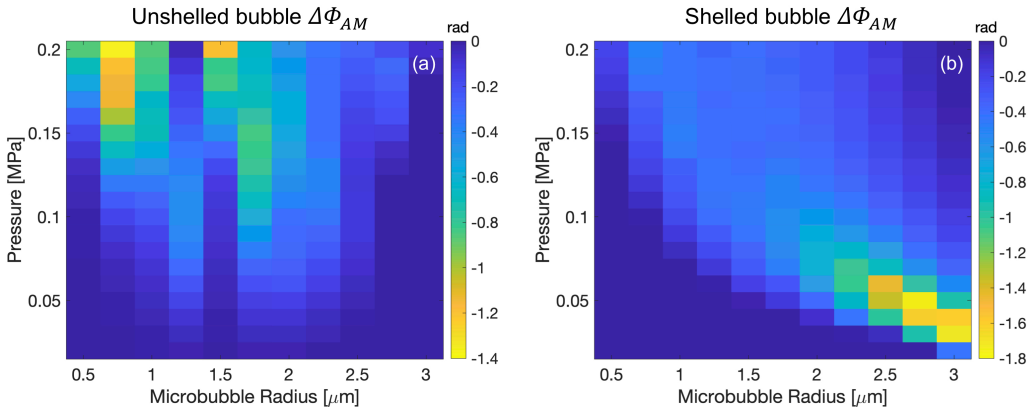

Fig. 5.5: $\Delta\Phi_{AM}$ resulting from unshelled and shelled bubbles as a function of the full pulse pressure and the microbubble radius. As in Fig. 4, the $\Delta\Phi_{AM}$ resulting from the unshelled bubble seems mostly dependent on amplitude and to a somewhat lesser degree on bubble radius, while the $\Delta\Phi_{AM}$ from the shelled bubble seems more dependent on bubble size and is in fact more prominent at smaller acoustic

5.3.2 $\Delta\Phi_{AM}$ from nonlinear propagation

Simulated waveforms from nonlinear propagation modeled with the KZK equation at pre-, at- and post-focal axial distances and various pressures are shown in **Fig. 5.6** (a-c), respectively. (d) shows $\Delta\Phi_{AM}$ versus the source pressure of p_{full}. Interestingly, the $\Delta\Phi_{AM}$ trends change based on location; at the focus, $\Delta\Phi_{AM}$ decreases with increasing source pressure. Before the focus, $\Delta\Phi_{AM}$ increases with increasing source pressure. After the focus, $\Delta\Phi_{AM}$ both first increases and then decreases with increasing source pressure but remains positive for the amplitudes considered. This behavior is due to the combined effects of diffraction and nonlinearity [10]. Notably, the magnitude of $\Delta\Phi_{AM}$ is much lower in magnitude from nonlinear propagation (d) than microbubble oscillation (**Fig. 5.4**). (e) shows absolute phase (not $\Delta\Phi_{AM}$) from the first, second, and third harmonics at various axial locations from the highest source pressure (1.2 MPa). It can be seen that the higher harmonics produce larger phase beyond focus compared to that produce by lower harmonics. This observation is consistent with what is shown in prior works [10], [25] and explains the existence of $\Delta\Phi_{AM}$ and its dependence on amplitude.

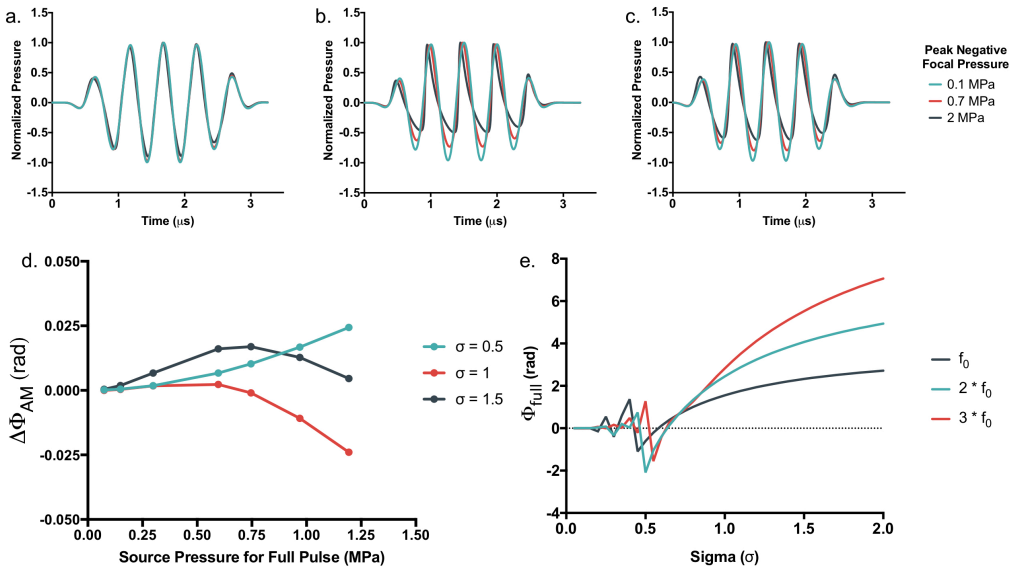

Fig. 5.6: (a) – (c) show pulses propagating nonlinearly in tissue at σ=0.5 (a), 1.0 (b), and 1.5 (c). A σ of 1 is equal to the focal length. Nonlinear behavior becomes much more prominent at and beyond the focus. (d) shows the calculated $\Delta\Phi_{AM}$ at each of these distances as a function of pressure. $\Delta\Phi_{AM}$ resulting from nonlinear propagation is much smaller in magnitude than the bubble simulations. (e) shows absolute phase of three harmonics at various axial locations from the highest source pressure (1.2 MPa).

5.3.3 $\Delta\Phi_{AM}$ from *in vitro* scattering

Example scattered echoes from a linear reflector without microbubbles (a) and from Sonazoid (b) when excited with a 0.2 MPa / 0.1 MPa AM pair can be seen in **Fig. 5.7**. Where the linear reflector scattered echoes that were well-defined and lacked any obvious $\Delta\Phi_{AM}$, microbubbles scattered much more irregular echoes that were lower in amplitude and had visible $\Delta\Phi_{AM}$.

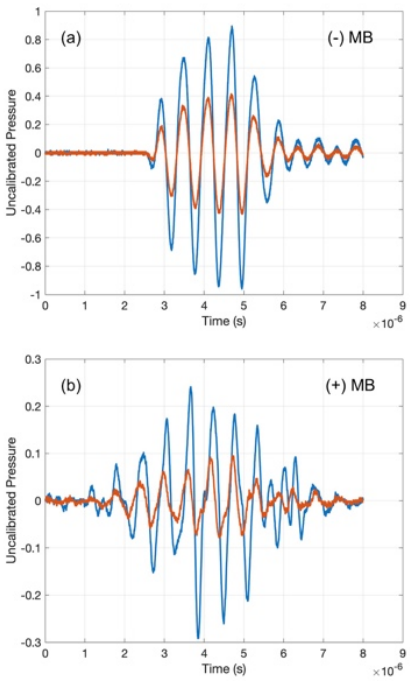

Fig. 5.7: Example scattered echoes from (a) a metal reflector, and (b) Sonazoid excited at 200 MPa (blue) and 100 MPa (orange). The echoes from the linear reflector were linear and without a visible phase difference $\Delta\Phi_{AM}$, while the echoes from Sonovue were nonlinear and with a visible $\Delta\Phi_{AM}$ (the zero crossings and the peaks and nulls did not align).

The average $\Delta\Phi_{AM}$ across all 20 trials can be seen in **Fig. 5.8**. The $\Delta\Phi_{AM}$ from all microbubble formulations was negative, consistent with the theoretical results. There was no obvious $\Delta\Phi_{AM}$ resulting from scattering off the linear reflector, although a very slight decline in $\Delta\Phi_{AM}$ at high pressures is registered. In general, Sonazoid and Optison generated $\Delta\Phi_{AM}$ that decreased with increasing pressure, and Sonovue generated $\Delta\Phi_{AM}$ that remained relatively constant. However, due to the inherent variability of scattering, the standard deviations were quite large, obfuscating clear trends between formulations and pressures.

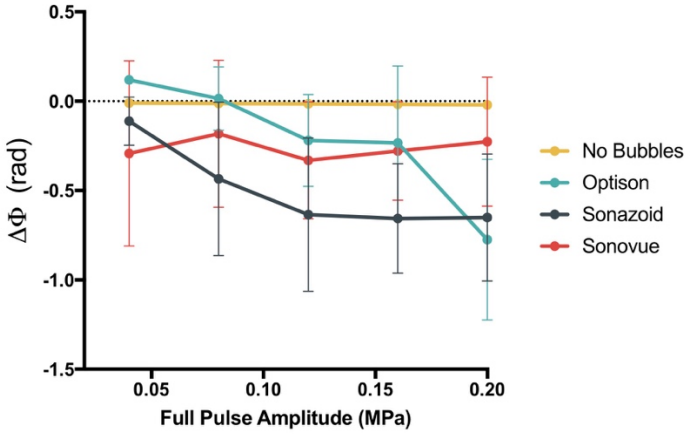

Fig. 5.8: $\Delta\Phi_{AM}$ measurements from scattering experiments. All microbubble types produced a negative $\Delta\Phi_{AM}$, while linear echoes from a metal tube did not produce obvious $\Delta\Phi_{AM}$, although a very slight decline registered at the highest pressures).

5.3.4 $\Delta\Phi_{AM}$ from RF data acquisition

Fig. 5.9 shows the region of interest (ROI) locations analyzed for $\Delta\Phi_{AM}$ in the (a) C5-1 and (b) L12-5, and the resultant $\Delta\Phi_{AM}$ beneath. $\Delta\Phi_{AM}$ for all MIs ranged from -0.1 rad to -0.4 rad for the C5-1 (1.7 MHz transmit frequency) and 0 rad to -0.3 rad for the L12-5 (4.1 MHz transmit frequency). Different microbubble formulations had slightly different $\Delta\Phi_{AM}$ behavior; Sonazoid provided a lower $\Delta\Phi_{AM}$ than Sonovue or Optison at low MI. At high MI, $\Delta\Phi_{AM}$ was similar between all formulations. At the 4.1 MHz frequency, Sonovue, in general, produced the greatest $\Delta\Phi_{AM}$, although Sonazoid provided a similar $\Delta\Phi_{AM}$ when excited with the highest pressure.

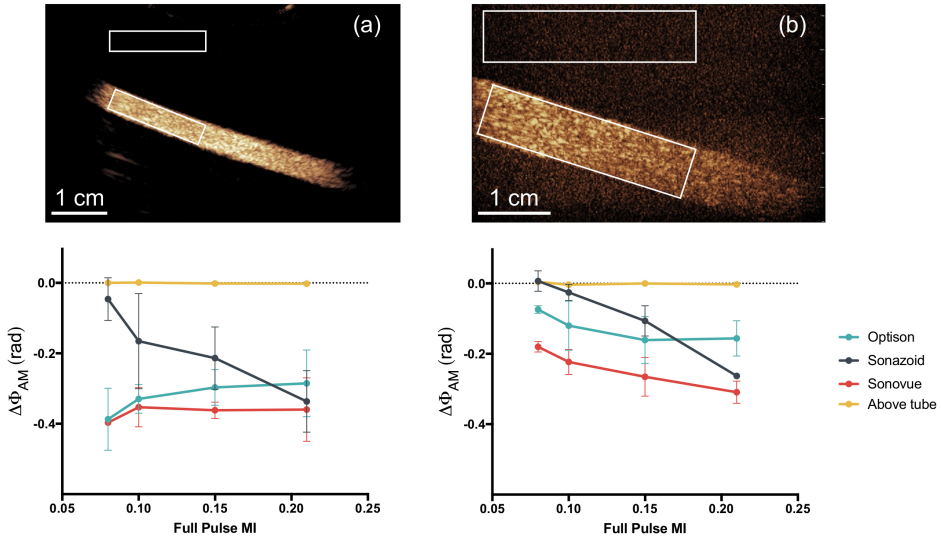

Fig. 5.9: $\Delta\Phi_{AM}$ measurements from radiofrequency (RF) data acquisition with a (a) C5-1 curvilinear array and (b) L12-5 array on the Philips iU22 scanner. The top row shows the regions of interest (ROIs) selected for analyzing the phase in the echoes and calculating $\Delta\Phi_{AM}$ for three microbubble formulations. An additional ROI for both the C5-1 and L12-5 above the tube was taken as a tissue control. $\Delta\Phi_{AM}$ results are shown in the bottom row. All microbubble formulations produced a negative $\Delta\Phi_{AM}$, while tissue produced a negligible $\Delta\Phi_{AM}$. Slight differences in $\Delta\Phi_{AM}$ between formulations could be attributed to size and composition).

5.4 DISCUSSION

The goal of this work was to investigate $\Delta\Phi_{AM}$ resulting from both unshelled and shelled microbubble oscillation as well as nonlinear propagation in tissue through both theoretical simulations and *in vitro* experimentation, with the goal of informing optimal parameters for phase segmentation. We observed that both shelled and unshelled microbubbles produced a significant negative $\Delta\Phi_{AM}$, validated with measurements using AM imaging on commercial microbubble formulations in a flow phantom. We also observed that nonlinear propagation resulted in a small degree of $\Delta\Phi_{AM}$, a new finding which could both implicate the reliability of phase segmentation at high mechanical indices as well as open the possibility for phase segmentation during tissue harmonic imaging.

We first evaluated $\Delta\Phi_{AM}$ resulting from unshelled and shelled bubble oscillation during amplitude modulation using the Rayleigh-Plesset and Marmottant Equations, respectively. The most striking result of these simulations was that both shelled and unshelled bubbles produce a distinct negative $\Delta\Phi_{AM}$, dependent on both pressure and bubble size but with differences in overall trends. Unshelled bubbles modeled with the Rayleigh-Plesset Equation provided a $\Delta\Phi_{AM}$ that increased in magnitude with increasing pressure and seemed to be most resonant around 0.7-1.5 μm. We also performed the same calculation with the Gilmore equation [15] which accounts for liquid compressibility and violent bubble collapse including shocks and found very similar results. We chose to use the Rayleigh-Plesset equation instead since the Marmottant model is based on it. Shelled bubbles modeled with the Marmottant Equation resulted in waveforms that were more consistent with "compression-only" behavior [27] as seen in Fig. 3, and different overall $\Delta\Phi_{AM}$ trends. Large, shelled bubbles excited at low pressures resulted in the greatest magnitude of $\Delta\Phi_{AM}$. At smaller radii, $\Delta\Phi_{AM}$ of shelled bubbles was mostly dependent on pressure. We calculated that

the resonance size of a free bubble at 1.7 MHz was approximately 1.5 μm and assumed that the resonance size would be larger for shelled bubbles. The $\Delta\Phi_{AM}$ results were consistent with these assumptions as well as with previous results observed by Tremblay-Darveau, et al. [13]. Previously, Tremblay-Darveau attributed the appearance of $\Delta\Phi_{AM}$ solely to shell parameters. The results from our work simulating free gas bubbles suggests that $\Delta\Phi_{AM}$ may have more dependence on nonlinear oscillation of the bubble, whereas the specific trends and resonance characteristics of the $\Delta\Phi_{AM}$ results are impacted by the shell parameters. Due to the strong dependence of $\Delta\Phi_{AM}$ on microbubble radius, phase segmentation could likely be enhanced by using monodisperse microbubbles [28].

The *in vitro* measurements evaluating $\Delta\Phi_{AM}$ with a single element transducer setup first and the ultrasound scanner next confirmed and extended the simulation results. We observed predominantly negative phase differences dependent on microbubble formulation and pressure. Sonazoid produced the greatest magnitude of $\Delta\Phi_{AM}$ at high pressures, while Sonovue and Optison produced greater $\Delta\Phi_{AM}$ at low pressures. This is consistent with the fact that Sonazoid is recommended for use at higher MI [29] than Sonovue and Optison which have lower overall cavitation thresholds [23]. The $\Delta\Phi_{AM}$ trends observed in our measurements were similar between the single element transducer setup and the imaging of a flow phantom with a scanner. Finally, we saw, in general, a greater $\Delta\Phi_{AM}$ when imaging at lower frequencies (C5-1 vs. L125 probes). This makes sense, given that microbubbles display resonance behavior dependent on size and frequency [30]. For lower frequency applications such as abdominal imaging this should not be a limitation for using phase segmentation during AM imaging. For clinical applications requiring higher frequencies such as breast or peripheral imaging [31], the generated $\Delta\Phi_{AM}$ from microbubbles is lower and hence the signal segmentation may be more challenging but still feasible.

Finally, we evaluated $\Delta\Phi_{AM}$ resulting from nonlinear propagation in tissue using the KZK Equation. We found that nonlinear sound propagation from high pressure transmit pulses results in $|\Delta\Phi_{AM}|$ between 0 and 0.025 rad. The sign and magnitude of $\Delta\Phi_{AM}$ from nonlinear propagation depended on the axial location: pre-focally, the $\Delta\Phi_{AM}$ was mostly positive; at the focus, the $\Delta\Phi_{AM}$ was mostly negative; beyond the focus, the $\Delta\Phi_{AM}$ was again mostly positive. It has been previously reported that tissue produces minimal $\Delta\Phi_{AM}$ [13]. While indeed at a much lower

magnitude, our results indicate that nonlinear propagation does in fact result in clear $\Delta\Phi_{AM}$, which has not been evaluated before. That said, microbubble imaging generally takes place at low amplitudes (MI ≤ 0.1) [1], in which the $\Delta\Phi_{AM}$ from nonlinear propagation is very small. Furthermore, certain microbubble agents, such as Sonazoid, are clinically recommended for use at slightly higher MIs [29] than SonoVue and Optison, at which point $\Delta\Phi_{AM}$ from nonlinear propagation will have a higher value that must be considered for segmentation. Although not evaluated in the present work, the discovery of $\Delta\Phi_{AM}$ arising from nonlinear propagation could open the possibility of performing tissue harmonic imaging using an amplitude modulation scheme with phase segmentation at high MI to distinguish between linear and nonlinear tissue signals.

We acknowledge several limitations to this study. First, we limited our simulation acoustic parameters in order to use standard microbubble imaging parameters modeled off the contrast AM setting on the Philips iU22. Since we were primarily interested in comparison between shelled bubbles, unshelled bubbles, and tissue, we deemed that maintaining a constant imaging parameter set minimized complexity. Second, we opted to evaluate $\Delta\Phi_{AM}$ at the fundamental frequency, both to be consistent with prior work, and because microbubble signal is strongest at the fundamental. Future efforts could evaluate the use of harmonics or alternate methods of phase analysis, such as cross correlation analysis, to incorporate other frequencies. Finally, although we mention that $\Delta\Phi_{AM}$ could potentially be used in tissue harmonic imaging, we have not yet evaluated this method, but it presents an exciting opportunity for future work.

5.5 CONCLUSION

Phase difference between full and half amplitude echoes during amplitude modulation (defined in the present study as $\Delta\Phi_{AM}$) was investigated through simulations of nonlinear oscillation of free and shelled bubbles, nonlinear propagation in tissue, and *in vitro* scattering and AM imaging of commercial microbubbles. We observed that both shelled and unshelled microbubbles resulted in a $\Delta\Phi_{AM}$ with similar overall magnitude with some differences in trends; $\Delta\Phi_{AM}$ from unshelled bubbles was most prominent at large acoustic pressures, while $\Delta\Phi_{AM}$ from shelled bubbles was most prominent at low acoustic pressures and large bubble radii. Regardless, the appearance of $\Delta\Phi_{AM}$ from free bubble simulations, which have not been evaluated for this purpose before,

suggest nonlinear oscillation may be a dominant mechanism determining $\Delta\Phi_{AM}$, not shell parameters as previously reported. Simulations of nonlinear propagation in tissue resulted in $\Delta\Phi_{AM}$ of about |0.025| rad, much lower than that of simulated free gas bubbles (up to |1.4| rad), shelled microbubbles (up to |1.8| rad) and experimentally measured commercial microbubbles (up to |1| rad). Although low, the presence of phase difference in tissue has a strong implication on parameter selection for optimal segmentation based on echo phase.

5.6 ACKNOWLEDGMENTS

We gratefully acknowledge GE Healthcare for the Sonazoid and Optison microbubbles used in this study. We would also like to thank Dr. Thanasis Loupas and Dr. Matt O'Donnell for their helpful discussions.

5.7 REFERENCES

[1] M. A. Averkiou, M. F. Bruce, J. E. Powers, P. S. Sheeran, and P. N. Burns, *Imaging Methods for Ultrasound Contrast Agents*, vol. 46, no. 3. 2020, pp. 498–517. doi: 10.1016/j.ultrasmedbio.2019.11.004.

[2] S. Sirsi and M. Borden, "Microbubble Compositions, Properties and Biomedical Applications," *Bubble Sci Eng Technol.*, vol. 1, pp. 3–17, 2010, doi: 10.1179/175889709X446507.Microbubble.

[3] E. Stride, "Physical principles of microbubbles for ultrasound imaging and therapy," *Cerebrovascular Diseases*, vol. 27, no. SUPPL. 2, pp. 1–13, 2009, doi: 10.1159/000203122.

[4] J. R. Lindner, "Microbubbles in medical imaging: Current applications and future directions," *Nature Reviews Drug Discovery*, vol. 3, no. 6, pp. 527–532, 2004, doi: 10.1038/nrd1417.

[5] K. Ferrara, R. Pollard, and M. Borden, "Ultrasound Microbubble Contrast Agents: Fundamentals and Application to Gene and Drug Delivery," *Annu. Rev. Biomed. Eng*, vol. 9, pp. 415–47, 2007, doi: 10.1146/annurev.bioeng.8.061505.095852.

[6] R. J. Eckersley, C. T. Chin, and P. N. Burns, "Optimising phase and amplitude modulation schemes for imaging microbubble contrast agents at low acoustic power.," *Ultrasound in medicine & biology*, vol. 31, no. 2, pp. 213–9, Feb. 2005, doi: 10.1016/j.ultrasmedbio.2004.10.004.

[7] T.-Y. Lai and M. A. Averkiou, "Linear Signal Cancellation of Nonlinear Pulsing Schemes in a Verasonics Research Scanner," *IEEE Transactions on Ultrasonics, Ferroelectrics, and Frequency Control*, vol. 68, no. 5, pp. 1721–1728, May 2021, doi: 10.1109/TUFFC.2021.3050481.

[8] T.-Y. Lai and M. A. Averkiou, "Linear Signal Cancellation of Nonlinear Pulsing Schemes in a Verasonics Research Scanner," *IEEE Transactions on Ultrasonics, Ferroelectrics, and Frequency Control*, vol. 68, no. 5, pp. 1721–1728, May 2021, doi: 10.1109/TUFFC.2021.3050481.

[9] O. Couture, M. Fink, and M. Tanter, "Ultrasound contrast plane wave imaging.," *IEEE transactions on ultrasonics, ferroelectrics, and frequency control*, vol. 59, no. 12, pp. 2676–83, Dec. 2012, doi: 10.1109/TUFFC.2012.2508.

[10] M. F. Hamilton and D. T. Blackstock, *Nonlinear acoustics*. Academic press San Diego, 1998.

[11] P.-C. Li, C.-C. Shen, and S.-W. Huang, "Waveform design for ultrasonic pulse-inversion fundamental imaging.," *Ultrasonic imaging*, vol. 28, no. 3, pp. 129–43, Jul. 2006, doi: 10.1177/016173460602800301.

[12] P. J. Phillips, "Contrast pulse sequences (CPS): imaging nonlinear microbubbles," in *2001 IEEE Ultrasonics Symposium. Proceedings. An International Symposium (Cat. No.01CH37263)*, vol. 2, pp. 1739–1745. doi: 10.1109/ULTSYM.2001.992057.

[13] C. Tremblay-Darveau *et al.*, "The Role of Microbubble Echo Phase Lag in Multipulse Contrast-Enhanced Ultrasound Imaging," *IEEE Transactions on Ultrasonics, Ferroelectrics, and Frequency Control*, vol. 65, no. 8, pp. 1389–1401, Aug. 2018, doi: 10.1109/TUFFC.2018.2841848.

[14] P. Marmottant *et al.*, "A model for large amplitude oscillations of coated bubbles accounting for buckling and rupture," *The Journal of the Acoustical Society of America*, vol. 118, no. 6, pp. 3499–3505, Dec. 2005, doi: 10.1121/1.2109427.

[15] T. G. Leighton, *The acoustic bubble*. Academic Press, 1994. Accessed: May 04, 2020. [Online]. Available: https://books.google.com/books?hl=en&lr=&id=tR-8SNimBuEC&oi=fnd&pg=PP1&dq=the+acoustic+bubble&ots=gXFvww2dNm&sig=xWRjTxAgl6LhMTU51_kJDs4XWCM#v=onepage&q=the%20acoustic%20bubble&f=false

[16] V. Kuznetsov, "Equations of nonlinear acoustics," *Soviet Physics Acoustics*, vol. 16, pp. 467–470, 1971.

[17] E. Zabolotskaya, "Quasi-plane waves, in the nonlinear acoustics of confined beams," *Soviet Physics Acoustics*, vol. 15, pp. 35–40, 1969.

[18] W. Lauterborn, "Numerical investigation of nonlinear oscillations of gas bubbles in liquids," *Journal of the Acoustical Society of America*, vol. 59, no. 2, pp. 283–293, Aug. 1976, doi: 10.1121/1.380884.

[19] M. A. Averkiou, Y. Lee, and M. F. Hamilton, "Self-demodulation of amplitude- and frequency-modulated pulses in a thermoviscous fluid," *The Journal of the Acoustical Society of America*, vol. 94, no. 5, pp. 2876–2883, Nov. 1993, doi: 10.1121/1.407344.

[20] M. A. Averkiou and M. F. Hamilton, "Measurements of harmonic generation in a focused finite-amplitude sound beam.," *The Journal of the Acoustical Society of America*, vol. 98, no. 6, pp. 3439–42, Dec. 1995, doi: 10.1121/1.413795.

[21] T.-Y. Lai, M. Bruce, and M. A. Averkiou, "Modeling of the Acoustic Field Produced by Diagnostic Ultrasound Arrays in Plane and Diverging Wave Modes.," *IEEE transactions on ultrasonics, ferroelectrics, and frequency control*, vol. 66, no. 7, pp. 1158–1169, 2019, doi: 10.1109/TUFFC.2019.2908831.

[22] M. A. Averkiou and M. F. Hamilton, "Nonlinear distortion of short pulses radiated by plane and focused circular pistons," *The Journal of the Acoustical Society of America*, vol. 102, no. 5, p. 2539, Jun. 1998, doi: 10.1121/1.420308.

[23] S. B. Keller, P. S. Sheeran, and M. A. Averkiou, "Cavitation Therapy Monitoring of Commercial Microbubbles With a Clinical Scanner," *IEEE Transactions on Ultrasonics, Ferroelectrics, and Frequency Control*, vol. 68, no. 4, pp. 1144–1154, Apr. 2021, doi: 10.1109/TUFFC.2020.3034532.

[24] M. Minnaert, "On musical air-bubbles and the sounds of running water," *Philos. Mag.*, vol. 16, pp. 235–248, Aug. 1933, doi: 10.1080/14786443309462277.

[25] T. S. Hart and M. F. Hamilton, “Nonlinear effects in focused sound beams,” *The Journal of the Acoustical Society of America*, vol. 84, no. 4, pp. 1488–1496, Oct. 1988, doi: 10.1121/1.396595.
[26] N. de Jong *et al.*, “‘Compression-Only’ Behavior of Phospholipid-Coated Contrast Bubbles,” *Ultrasound in Medicine and Biology*, vol. 33, no. 4, pp. 653–656, Apr. 2007, doi: 10.1016/j.ultrasmedbio.2006.09.016.
[27] T. Segers, P. Kruizinga, M. P. Kok, G. Lajoinie, N. de Jong, and M. Versluis, “Monodisperse Versus Polydisperse Ultrasound Contrast Agents: Non-Linear Response, Sensitivity, and Deep Tissue Imaging Potential,” *Ultrasound in Medicine & Biology*, vol. 44, no. 7, pp. 1482–1492, Jul. 2018, doi: 10.1016/J.ULTRASMEDBIO.2018.03.019.
[28] J. Y. Jang *et al.*, “Current consensus and guidelines of contrast enhanced ultrasound for the characterization of focal liver lesions,” *Clinical and Molecular Hepatology*, vol. 19, no. 1, p. 1, 2013, doi: 10.3350/cmh.2013.19.1.1.
[29] A. A. Doinikov, J. F. Haac, and P. A. Dayton, “Resonance frequencies of lipid-shelled microbubbles in the regime of nonlinear oscillations.,” *Ultrasonics*, vol. 49, no. 2, pp. 263–8, Feb. 2009, doi: 10.1016/j.ultras.2008.09.006.
[30] M. Bruce *et al.*, “High-Frequency Nonlinear Doppler Contrast-Enhanced Ultrasound Imaging of Blood Flow,” *IEEE Transactions on Ultrasonics, Ferroelectrics, and Frequency Control*, vol. 67, no. 9, pp. 1776–1784, Sep. 2020, doi: 10.1109/TUFFC.2020.2986486.

Chapter 6. CONTRAST ENHANCED ULTRASOUND WITH OPTIMIZED APERTURE PATTERNS

Abstract

Amplitude modulation (AM) is often implemented with checkerboard apertures to suppress tissue signals and detect microbubble signals in contrast-enhanced ultrasound (CEUS). However, the crosstalk between transmitting and non-transmitting array elements may compromise tissue suppression in AM. Using alternative AM aperture patterns may reduce the degree of crosstalk and possibly generate more nonlinear microbubble signals compared to conventional AM. Furthermore, previous studies have shown that the phase difference between the echoes in AM pulsing sequence may be used as a segmentation criterion for tissue and microbubbles to improve tissue signal suppression and the contrast-to-tissue ratio (CTR) of CEUS images. However, the CTR of the image produced by alternative AM aperture patterns and the effect of segmentation approach on these alternative apertures has not been investigated yet. We evaluated 29 AM aperture patterns in order to find the optimal AM aperture pattern with the highest CTR. We found that AM2, which uses alternating groups of 2 elements, had the highest CTR for the probe used and was ~2 dB higher than conventional AM. The addition of segmentation based on echo phase differences (between the full and the half pulses-- $\Delta\Phi_{AM}$, between the complimentary half pulses-- $\Delta\Phi_{half}$, and the maximum of the two-- $\Delta\Phi_{max}$) was considered in the AM aperture optimization process and increased the CTR by 20-25 dB. Finally, AM2 segmented with $\Delta\Phi_{max}$, had a 10 dB higher CTR in a flow phantom and a 7 dB higher contrast in a perfused pig liver than conventional AM segmented with $\Delta\Phi_{AM}$.

Manuscript in preparation

6.1 INTRODUCTION

Contrast-enhanced ultrasound (CEUS) utilizes the nonlinear echoes from microbubbles [1] for real-time imaging of perfusion of organs and tumors [2-4]. CEUS provides information of the macro- and microvasculature of organs and tumors [5, 6]. In recent years, ultrafast imaging techniques such as plane wave imaging (PWI) and diverging wave imaging (DWI) have emerged [7]. PWI/DWI excites a large number of the array elements to insonify the whole field of view in one transmit event while beamforming multiple receive lines and thus allowing a significant improvement in frame rate. A previous study has demonstrated the possibility of achieving frame rates close to 20,000 Hz with PWI, over 500 times greater than those achieved with conventional focused beamforming [8]. Combining ultrafast imaging with CEUS [9] has enabled super resolution imaging [10, 11], which allows visualization of the microvasculature of the organs down to a few microns.

Nonlinear pulsing schemes are imaging strategies that isolate the nonlinear components of the echo to form the image. In nonlinear pulsing schemes, the scattered echoes of a series of transmitted pulses are combined in a way that the linear signals (produced by tissue) are cancelled while the nonlinear signals (produced by microbubbles) are detected. The two most common nonlinear pulsing schemes today are pulse inversion (PI) [12] and amplitude modulation (AM) [13, 14]. PI involves transmitting 2 pulses with the second pulse being the inverse of the first pulse (different in phase by π). By adding the produced echoes, the fundamental (and all odd harmonics) are removed prior to any RF-filtering operation while the second (and all even) harmonics are detected. The AM technique involves transmitting 2 pulses at different amplitudes. A commonly used version of AM is one where the amplitude of the second pulse is half that of the first pulse. The linear signals are removed by scaling the echoes of the second pulse by a factor of 2 and then subtracting them from the echoes of the first.

Tissue signal suppression is important in CEUS to achieve good image contrast and microbubble specificity. Incomplete tissue signal cancellation may mask real enhancement caused by microbubbles or be incorrectly interpreted as real enhancement [4]. However, transmitting two identical pulses with different polarities or with an exact amplitude ratio at different voltages is

challenging for the hardware due to nonlinearities in the signal generation and power amplifier [4]. A slight imperfection of the pulse inversion or amplitude change of the transmitted pulses would inevitably result in incomplete cancellation of the linear tissue signal.

Previous studies have shown that implementing AM with complimentary apertures improves tissue signal cancellation and requires less complex hardware [4, 9, 13, 15, 16]. This technique involves transmitting 3 pulses with the following sequence: p_{even}, p_{full}, and p_{odd}.With this technique, only even elements are used for transmitting p_{even}, only odd elements are used for p_{odd}, while all the elements are used for p_{full}. Since only half the elements are used for p_{even} and p_{odd}(when considering AM with a factor of 2 between the two amplitudes), the pressure produced by either p_{even} or p_{odd}, is half of that produced by $p_{full.}$ However, the crosstalk between transmitting and non-transmitting array elements may still compromise the degree of tissue signal suppression in AM [4]. Moreover, the degree of crosstalk may be more severe in ultrafast CEUS compared to that in conventional focused ultrasound since larger apertures are used for ultrafast imaging. In our previous work, we observed that the linear signal cancellation of a L7-4 array in plane wave mode is ~7 dB lower than that in focused mode at low MIs (≤ 0.1) [17]. The spatial characteristics of the acoustic fields in the AM pulsing sequences may also impact the nonlinear response from microbubbles. Using an alternative combination (instead of p_{even} and p_{odd}) for AM that still uses half or all the elements may reduce the degree of crosstalk between on/off elements while generating more nonlinear microbubble response compared to that generated by conventional AM. However, to the best of our knowledge, no studies have investigated the possibility of performing AM with other combinations of aperture patterns.

The image quality of CEUS is also limited by the tissue harmonics generated from the nonlinear propagation of sound waves in tissue. Optimal CEUS imaging is performed at low mechanical index (MI ≤0.1) to avoid microbubble destruction and the generation of tissue harmonics typically generated at MI>0.3, which may interfere with or mask the microbubble signals in CEUS images [18]. However, even at low MIs the tissue still generates some nonlinear response, which degrades the image contrast of CEUS [19, 20]. Efforts have been made to segment tissue echoes from microbubble echoes. Recently, it has been shown that microbubble contrast may also be generated by a difference in the phase between full and half amplitude pulses in AM [21]. This phase

difference is amplitude dependent. Since AM sequences in tissue are not expected to result in the same degree of phase difference as that in microbubbles, utilizing phase difference as a segmentation technique can therefore contribute towards better tissue signal suppression and higher image contrast in [21]. For this tissue segmentation technique to work, the phase difference in microbubble echoes should be significantly greater than that in tissue. In addition, previous studies have only utilized the phase difference produced by different pressure amplitude between full and half amplitude pulses for image segmentation. No studies have investigated the possibility of utilizing the phase difference between the complementary half amplitude pulses for phase segmentation. The phase difference between the complementary half amplitude pulses results from the difference between the spatial distribution of the complementary fields, which may induce additional microbubble phase response and would be useful for improving segmentation of microbubble signals.

There are 3 objectives in the present study. First, to evaluate the contrast-to-tissue ratio (CTR) of ultrafast CEUS when imaging with different aperture patterns and identify an optimal aperture for AM that would improve tissue signal suppression and image contrast for ultrafast CEUS. Second, to study how the phase difference between the complementary half amplitude pulses changes when using different aperture patterns and investigate the feasibility of utilizing this phase difference for segmentation of microbubble signals. Third, to propose a segmentation algorithm that utilizes not only the phase difference between the echoes of full and the sum of half amplitude pulses, but also the phase difference between the echoes of half amplitude pulses in the AM pulsing sequence.

6.2 METHODS

6.2.1 *Evaluation of aperture patterns for AM*

AM consists of transmitting 3 pulses with the following sequence: p_{even}, p_{full}, and p_{odd}. With this technique, the transmit voltage and transmit beamforming delays are not changed between p_{even}, p_{full}, and p_{odd}. As a result, the effective beam of the sum of p_{even} and p_{odd} is identical to that of the p_{full}. We can further generalize AM by transmitting 3 pulses with the following

sequence: p_h, p_{full}, and p_{h*}. Half of the elements are used for transmitting p_h, while the other half are used for p_{h*}, and all the elements are used for p_{full}.

Two possible combinations of aperture patterns used for p_h, p_{h*}, and p_{full} are shown in **Fig. 6.1**, where the elements in blue are transmitting elements and the elements in white are non-transmitting elements. To evaluate the different aperture patterns, we consider the following two parameters: (1) the number of on/off interfaces in the selected aperture pattern, and (2) the degree of overlap between two complementary apertures, which is calculated as the number of transmitting elements in the overlapped area between complementary apertures. As shown in **Fig. 6.1**, the complementary apertures in example 1 are highly overlapped and there are 12 transmitting elements in the overlapped area (within the red dashed lines). In addition, each aperture pattern has many on/off interfaces between elements. Conversely, the complementary apertures in example 2 (which admittedly is an extreme case and shown here for demonstration purposes) are not overlapped at all and have only 1 on/off interface between elements. We expected the acoustic fields of p_h and p_{h*} to be more uniform across the whole aperture when the complimentary apertures are more overlapped with each other. In addition, the crosstalk increases when more on/off interfaces are in an aperture pattern. We evaluated the acoustic field and the contrast-to-tissue ratio (CTR) of the CEUS images produced by 26 different aperture patterns. Each combination has different degree of overlap between the complimentary apertures and the number of on/off interfaces as it is shown in **Fig. 6.2**.

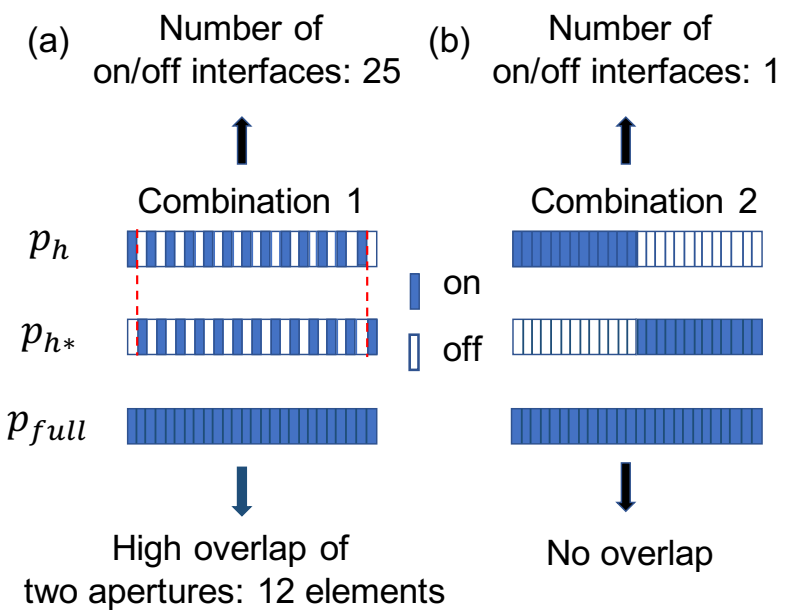

Fig. 6.1. Two examples of the 26 aperture patterns considered. The blue elements are transmitting elements and the white elements are non-transmitting elements. Example 1 has high overlap of its two complementary aperture patterns (indicated by red dashed lines) while example 2 has no overlap. Example 1 has more on/off interfaces than example 2 which has only 1.

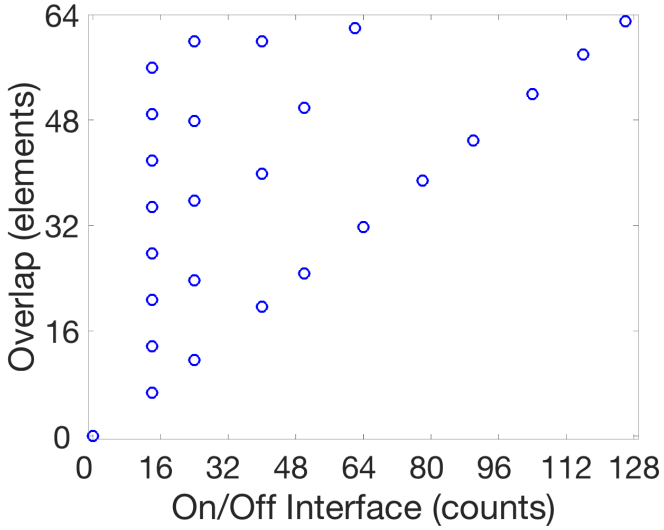

Fig. 6.2. The degree of overlap between complementary apertures and the number of on/off interfaces for the 26 apertures considered. Each blue circle represents a unique AM aperture pattern.

We also considered using spatially more dissimilar p_h and p_{h*} fields generated by random selection of the elements, referring to this scheme as random AM (RAM). We evaluated the

acoustic field produced by 3 combinations of random aperture pattern. RAM is considered here to further increase the spatial difference between the p_h and p_{h*} fields. For RAM, half of the array elements were randomly selected for transmitting p_h while the other half for transmitting p_{h*}. We evaluated 3 RAM examples with different number of on/off interfaces (47, 65, and 92) to produce various degrees of spatial differences between p_h and p_{h*} fields. The apertures for RAM were carefully chosen such that they have comparable degree of overlap between complementary apertures and minimal grouping of elements in the aperture pattern.

6.2.1.1 *Simulations of the acoustic field produced by different apertures*

The acoustic field produced by a Philips L7-4 array (Philips Healthcare, Bothell, WA, USA) using each of the 26 apertures were modeled with Field II [22, 23]. Field II is a transducer field simulation software based on the Rayleigh integral and is capable of modeling the acoustic field of non-axisymmetric sources with arbitrary focusing, apodization, and attenuation [22, 23]. The physical dimension of the transducer stack of the L7-4 array is 38.4 mm × 7.5 mm (azimuthal × elevation). For the simulations in this study, each simulation was modeled with 200 MHz sampling frequency and 25 sub-division in element height and width. The transmitted pulse has 2.5 cycles with a center frequency at 3.5 MHz. The imaging depth for the simulation was 6 cm.

6.2.1.2 *CTR when using different apertures*

We evaluated the CTR of CEUS images produced by 26 different apertures in a flow phantom system. Ultrafast acquisitions were performed with a Verasonics scanner (Verasonics Inc., Kirkland, WA, USA) connected with a L7-4 array. The transmitted pulse has 2.5 cycles with a central frequency at 3.5 MHz. The pulse repetition frequency (PRF) was 4000 Hz. The derated mechanical index (MI) of the full pulse in the pulsing sequence was 0.07. These imaging parameters were used for all the experiments in this study.

CTR was calculated as the mean intensity difference between a region with microbubbles and a region with tissue only in dB. The CTR calculation was performed on 100 CEUS images produced by the same combination of aperture pattern. The average CTR of 100 CEUS images was used for comparisons.

6.2.2 *Segmentation of microbubble signals based on the phase of echoes*

6.2.2.1 *Phase difference between the echoes from the full and the half amplitude pulses in AM*

AM was implemented on the Verasonics scanner according to the following equation:

$$ps_{AM}(i,j) = \frac{1}{3}ps_{full}(i,j) - \frac{1}{3}ps_h(i,j) - \frac{1}{3}ps_{h*}(i,j), \quad (6.1)$$

where ps_h, ps_{full}, and ps_{h*} are the echoes from microbubbles when transmitting p_h, p_{full}, and p_{h*} at point (*i,j*) in the image. The phase difference ($\Delta\Phi_{AM}$) resulting from the pressure amplitude difference between ps_{full} and the sum of ps_h and ps_{h*} were calculated according to equation (6.2):

$$\Delta\Phi_{AM}(i,j) = \angle\frac{ps_{full}(i,j)}{\{ps_h(i,j) + ps_{h*}(i,j)\}} \quad , \quad (6.2)$$

where $\angle$ is the "angle" operator on the complex signals. Equation (6.2) is equivalent to a two-pulse 1-D autocorrelator [24]. Since the sum of p_h and p_{h*} is identical to that of p_{full}, the acoustic field phase produced by the sum of p_h and p_{h*} is identical to that produced by p_{full}. We can then simplify equation (6.2) to:

$$\Delta\Phi_{AM} = \Phi_{full} - \Phi_{half} \quad , \quad (6.3)$$

where Φ_{full} and Φ_{half} are the phase from the microbubble scattering of ps_{full} and the sum of ps_h and ps_{h*}, respectively.

6.2.2.2 *Phase difference between the echoes of complementary half amplitude pulses in AM*

In order to further differentiate tissue and microbubble echoes we will also use the phase difference between ps_h and ps_{h*}. We hypothesized that the difference between the spatial distribution (diffraction pattern) of acoustic fields produced by p_h and p_{h*} may induce additional phase

difference in microbubble response, which could be used to improve the segmentation of microbubble signals. The phase difference ($\Delta\Phi_{half}$) resulting from the difference between the spatial distribution of p_h and p_{h*} fields were calculated according to equation (6.4):

$$\Delta\Phi_{half}(i,j) = \angle\frac{ps_h(i,j)}{ps_{h*}(i,j)} \ . \tag{6.4}$$

However, since p_h and p_{h*} fields are spatially different, the acoustic field phases produced by them are different and would not cancel out each other in equation (4). Since the phase of microbubble echoes are constantly changing from $-\pi$ to π over time during volumetric oscillation of microbubbles, the average value of the phase of microbubble echoes over time would be close to 0. As a result, the average of $\Delta\Phi_{half}$ over time would be equivalent to the phase difference between the acoustic field phase of ps_h and ps_{h*}. The phase difference ($\Delta\Phi_{half}$), after subtracting the average of $\Delta\Phi_{half}$ over time is:

$$\Delta_2\Phi_{half} = \Delta\Phi_{half} - Avg\left[\Delta\Phi_{half}\right] \ , \tag{6.5}$$

where $\Delta_2\Phi_{half}$ is the phase difference from the microbubble scattering of ps_h and ps_{h*}. According to equation (5), $\Delta_2\Phi_{half}$ increases as the phase difference from the microbubble echoes of ps_h and ps_{h*} increases, which we hypothesized that can be achieved by using spatially more dissimilar p_h and p_{h*} fields.

6.2.2.3 *Combined phase segmentation approach*

Finally, we proposed an approach that uses the maximum phase difference ($\Delta\Phi_{max}$) between $\Delta\Phi_{AM}$ and $\Delta_2\Phi_{half}$ for phase segmentation. $\Delta\Phi_{max}$ was calculated by using the maximum absolute phase difference at every point (*i,j*) between $\Delta\Phi_{AM}$ and $\Delta_2\Phi_{half}$ such that:

$$\Delta\Phi_{max}(i,j) = \max_{i,j}\left\{\left|\Delta\Phi_{AM}(i,j)\right|, \left|\Delta_2\Phi_{half}(i,j)\right|\right\} \ . \tag{6.6}$$

We expect that by utilizing the phase difference resulting from the pressure amplitude and the spatial difference of the fields at the same time, it would improve the segmentation of microbubble signals from tissue signals.

6.2.2.4 *Phase difference and image quality when using different phase segmentation approaches*

The phase difference between complex signals was calculated at the fundamental frequency. Complex signals for calculating the phase difference, including ps_h, ps_{full}, and ps_{h*}, were filtered with a passband FIR filter of 2-4 MHz bandwidth to preserve the signal only at the fundamental frequency. We investigated the change in the phase difference as spatial differences between p_h and p_{h*} increased. Five combinations of aperture patterns, including AM1, AM2, and 3 RAM examples, were used for comparisons. We calculated the $\Delta\Phi_{AM}$, $\Delta_2\Phi_{half}$, and $\Delta\Phi_{max}$ for all points in the image for AM1, AM2, and the 3 RAM examples.

To perform image segmentation, the phase difference information was used as a mask to remove the noise and the nonlinear tissue clutter. More specifically, the phase segmented signal ps'_{AM} at point (i,j) was calculated by multiplying the original nonlinear signals ps_{AM} with the Heaviside function $H(x)$ such that:

$$ps'_{AM}(i,j) = ps_{AM}(i,j)H(|\Delta\Phi(i,j)| - \Delta\Phi_{th}), \tag{6.7}$$

where $\Delta\Phi_{th}$ is a threshold value in rad. Pixels in $ps_{AM}(i,j)$ that have smaller $\Delta\Phi$ than $\Delta\Phi_{th}$ were set to the average of the lowest value in each image of $ps_{AM}(i,j)$. We then selected a $\Delta\Phi_{th}$ value that maximizes the CTR of the image. The segmented images may still present tissue or noise signals when the $\Delta\Phi_{th}$ value is very low, however, they may lose most of the microbubble signals when $\Delta\Phi_{th}$ is too high. We used different $\Delta\Phi_{th}$ values that maximized the CTR of the images produced by each combination of aperture pattern and phase segmentation approach. We compared the CTR of the CEUS images of a flow phantom with microbubbles produced by AM1 (which uses alternating groups of 1 elements), AM2 (which uses alternating groups of 2 elements), and 3 RAM examples, each segmented with $\Delta\Phi_{AM}$, $\Delta_2\Phi_{half}$, or $\Delta\Phi_{max}$.

Finally, we compared AM2 with AM1 in a perfused pig liver model [25]. A 32s CEUS image loop of the pig liver vasculature was acquired by each of AM1 and AM2. We also compared the time-intensity curves (TIC) calculated with images produced by AM to that produced by AM2. TIC provides information of the wash in and washout of the microbubbles in a region of interest (ROI) [4, 26] and it may be used [27, 28] for assessing tumor response after treatment [29]. We formed TICs from a ROI in the liver microcirculation. The CEUS images produced by AM1 and AM2 for calculating the TICs were segmented with $\Delta\Phi_{AM}$ and $\Delta\Phi_{max}$, respectively, to compare the performance of the proposed phase segmentation approach to that of a previous phase segmentation approach. $\Delta\Phi_{th}$ values that maximized the difference in the average intensity of the ROI between 2 time points (before bolus injection and when microbubbles were fully perfused) were used for image segmentation.

6.2.3 *Flow phantom experiment setup*

The experimental setup used for evaluating different apertures and different phase segmentation approaches is shown in **Fig. 6.3**. A closed loop flow phantom with a single flow channel was used. The main components of this setup are: (1) a peristaltic pump that consists of Masterflex L/S Variable Drive, 600 rpm (Model 07528-10; Cole Parmer, Vernon Hills, IL) with an Easy-Load II pump head (Model 77200-62; Cole Parmer), and (2) a peripheral vascular Doppler flow phantom (Model 523A-modified; ATS Laboratories, Bridgeport, CT), of which we used the 8.0 mm conduit. Tygon Silicone Tubing (Cole Parmer) of 1/4 inch (=6.4 mm) inner diameter was used to connect the various components. A short stretch of Masterflex L/S Platinum-Cured Silicone Tubing (model 96410-24; Cole Parmer) was used for the peristaltic pump. Quick connect and disconnect fittings (Colder Products Company, St Paul, MN) were used for connections. The flow rate was controlled at 140 mL/min. The L7-4 array was coupled to the tissue phantom with ultrasound gel and was held by a passive arm. The alignment was such that the center of the imaged conduit was at 3.5 cm image depth. The total image depth was 6 cm. Optison microbubbles (GE Healthcare, Chicago, IL, USA) were prepared as described by the manufacturer. They were then drawn from the vial with a 21G needle and diluted to a 1/10000 concentration in deionized water, before the solution was flowed within the flow-system.

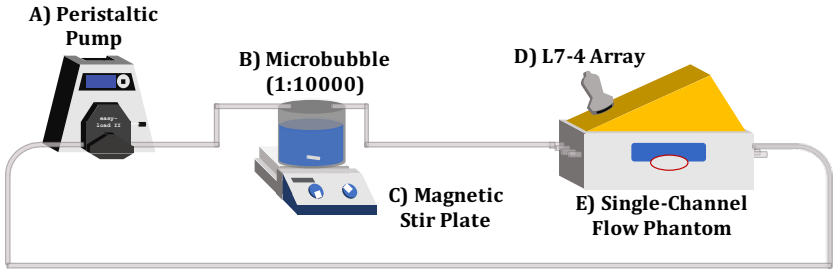

Fig. 6.3. Experimental setup for the flow phantom system.

6.2.4 *Perfused pig liver experiment setup*

The perfused pig liver model provides an ideal environment for pre-clinical imaging investigations since it is very similar to an *in vivo* environment. The setup for perfused pig liver experiment is a slight modification of the setup described previously [29]. Briefly, healthy porcine livers were isolated and surgically removed from a deceased pig within 30 minutes of the animal's death. This is to limit ischemic tissue death and vascular stenosis by thrombosis. The portal vein and hepatic artery of the liver were then flushed with 8 liters of lactated ringer's solution (6 liters at room temperature and 2 liters ice cold) followed by 3 liters of ice-cold histidine-tryptophan-ketoglutarate (HTK) solution (prepared in-house). Subsequently, the liver was placed in 2 liters of HTK solution in static cold storage and transported back to the laboratory, where it was connected to a normothermic machine-perfusion system. The liver was perfused with 8 liters of blood mimicking fluid that consist of Powdered Williams Medium E, sodium bicarbonate, heparin, insulin, and dexamethasone. The liver was also supplied with 95% oxygen/5% carbon dioxide via an oxygenator in the machine-perfusion system.. The alignment was such that the center of the liver was at 2 cm, which is also the center of the total image depth (4 cm). Optison microbubbles (GE Healthcare, Chicago, IL, USA) were prepared and injected in the liver in the same manner as done in the flow phantom.

6.3 RESULTS

6.3.1 *The acoustic fields produced by different apertures*

Example Field II simulations of the acoustic field produced by 6 (of the 26) aperture patterns evaluated in this study are shown in **Fig. 6.4**. We only show the p_h fields in the figure since p_h and p_{h*} are complementary and p_{full} is simply the whole aperture. The numbers in parenthesis in each figure represent the number of on/off interfaces and overlap in terms of elements of the complementary apertures, respectively. The acoustic field produced by AM1 (conventional AM) is shown in **Fig. 6.4** (f). As expected, the acoustic field is more uniform across the whole aperture when the complementary apertures are more overlapped with each other. In addition, the acoustic field is more uniform across the whole aperture when the aperture pattern has more on/off interfaces [**Fig. 6.4** (c)-(f)]. The peak pressure of the p_h fields is larger when the complementary apertures are less overlapped with each other. For example, the peak pressure in **Fig. 6.4** (a) is about twice the peak pressure in **Fig. 6.4** (f). Field II simulations of the p_h and p_{h*} fields produced by RAM_{41}, RAM_{65}, and RAM_{92} (subscript indicates the number of on/off interfaces) are shown in **Fig. 6.5**. As seen in the figure, p_h and p_{h*} fields are spatially more different when RAM has a smaller number of on/off interfaces.

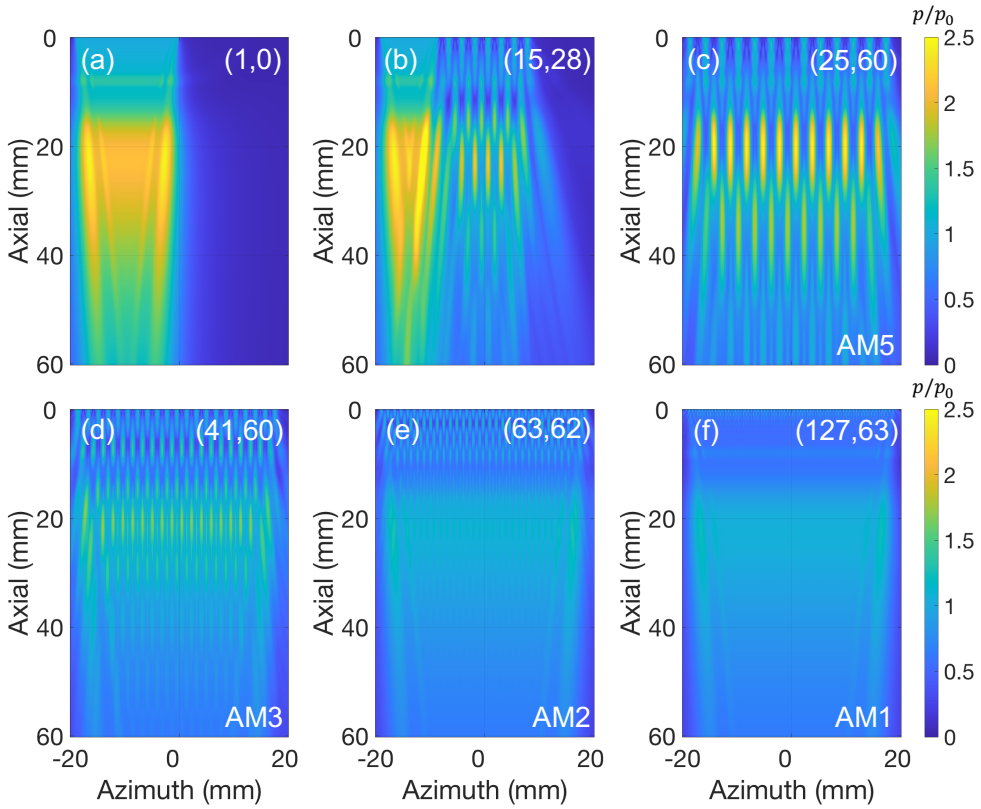

Fig. 6.4. Field II simulations of the acoustic field produced by the 6 (out of the 26) apertures evaluated in this study. Only the p_h field is shown in the figure since p_h and p_{h*} are complementary. The numbers in parenthesis at the top of the figure represents the number of on/off interfaces and overlap in terms of elements of the complementary apertures, respectively.

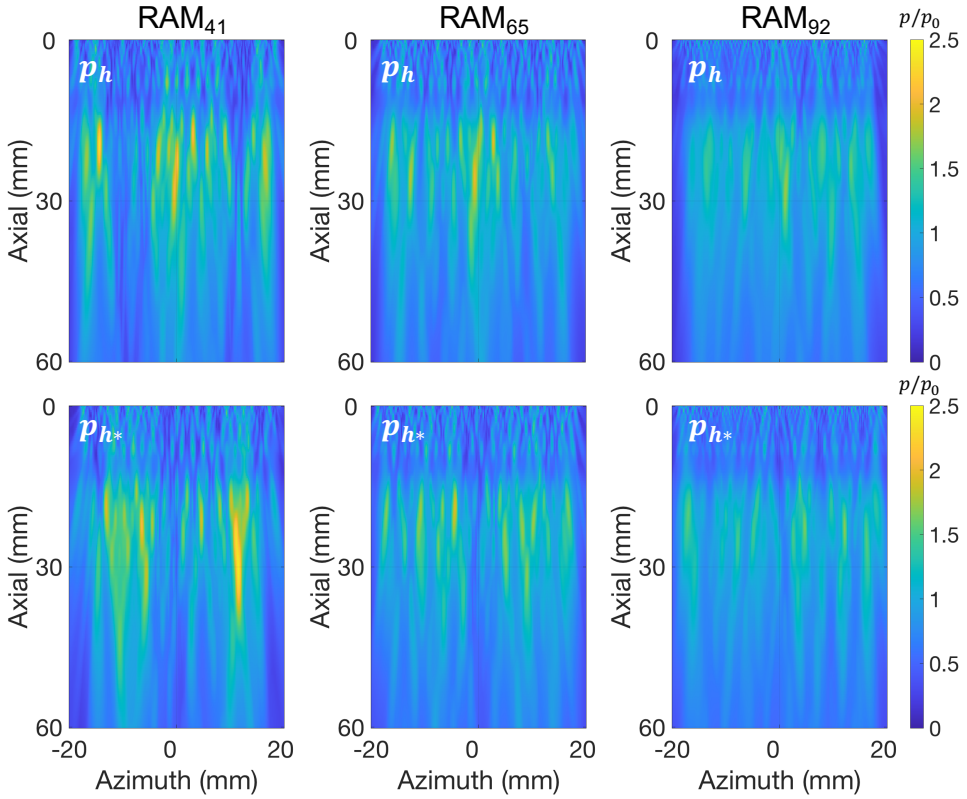

Fig. 6.5. Field II simulations of the acoustic field produced by the 3 random aperture patterns (RAM_{41}, RAM_{65}, and RAM_{92}). The subscript indicates the number of on/off interfaces in the aperture pattern.

6.3.2 *The effect of different aperture patterns*

CEUS images of the flow phantom produced by the apertures in **Fig. 6.4** (a), (e), and (f) are shown in **Fig. 6.6**. The intensity of the contrast signal is higher [**Fig. 6.6** (a) vs (c)] as p_h and p_{h*} fields are more overlapped with each other [**Fig. 6.4** (a) vs (f)]. We also observed that the intensity of the tissue signals and noise is lower [**Fig. 6.6** (b) vs (c)] when complementary apertures have similar degree of overlap but lower number of on/off interfaces [**Fig. 6.4** (e) vs (f)].

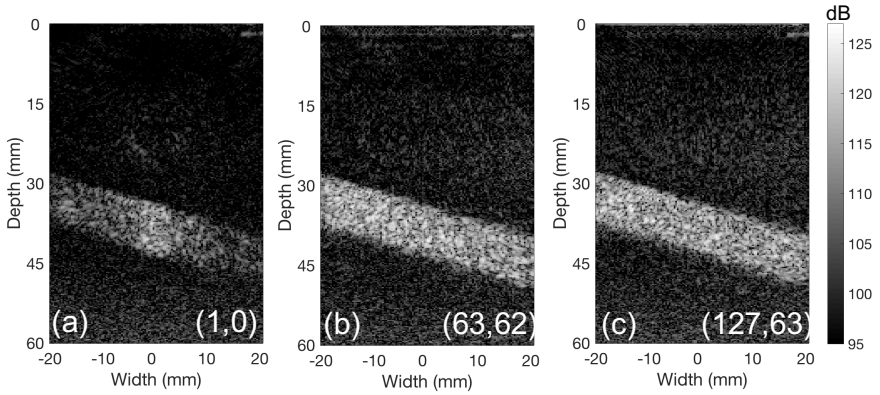

Fig. 6.6. CEUS images of a flow phantom produced by the 3 (out of the 26) apertures evaluated. The numbers in parenthesis in the figure represents the number of on/off interfaces and overlap in terms of elements of the complementary apertures, respectively.

Next, we evaluated the CTR of the images acquired with the 26 apertures considered. The ROIs for calculating the CTR of the image are shown in **Fig. 6.7** (a), where the ROI for contrast signals is shown in red and the ROIs for tissue signals are shown in yellow. The CTRs of the images produced by 26 apertures are shown in **Fig. 6.7** (b). When the number of on/off interfaces remains the same, the CTR increased with more overlapped complementary apertures. AM2 had the highest CTR (pointed by a red arrow). Although AM1 and AM2 have similar degree of overlap of complementary apertures (63 and 62, respectively), AM2 has half the number of on/off interfaces, which indicates lower crosstalk and thus better tissue signal suppression, compared to AM1.

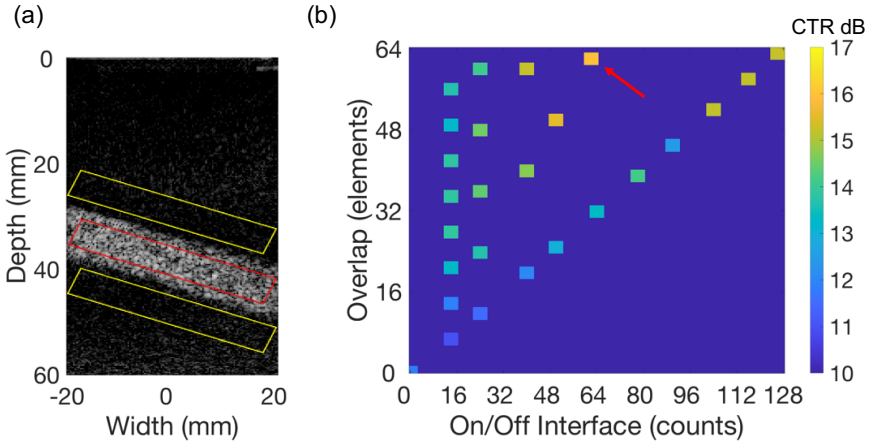

Fig. 6.7. (a) The CEUS image of the flow phantom and the ROIs for calculating CTR. ROIs for contrast signal are red and tissue signal are yellow. (b) CTR of the 26 apertures considered.

6.3.3 *The effect of phase segmentation*

Phase images for calculating $\Delta\Phi_{AM}$ are shown in **Fig. 6.8** (a)-(c), where (a) shows Φ_{full}, (b) Φ_{half}, and (c) $\Delta\Phi_{AM}$ produced by AM2. The phase values are shown in absolute scale for better visualization. As it is shown in **Fig. 6.8** (c), tissue has lower phase difference than microbubbles. Phase images for calculating $\Delta_2\Phi_{half}$ are shown in **Fig. 6.8** (d)-(e), where (d) shows $\Delta\Phi_{half}$, (b) $Avg[\Delta\Phi_{half}]$ from 100 CEUS images, and (f) the $\Delta_2\Phi_{half}$ produced by RAM41. The phase values are shown in absolute scale. As it is shown in **Fig. 6.8** (e), the average value of the phase produced by microbubbles over time was close to 0, as expected.

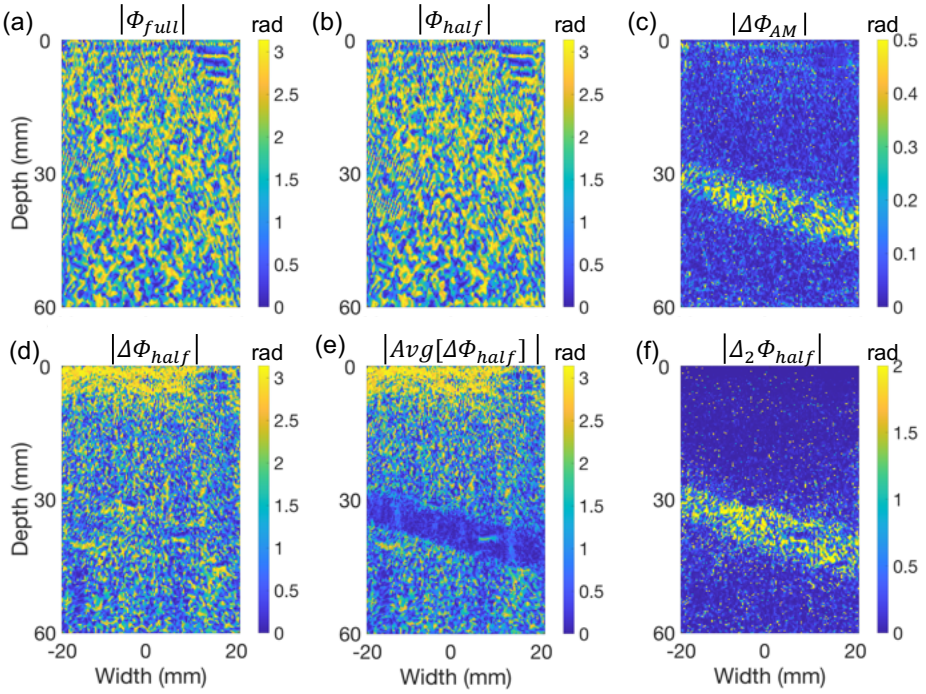

Fig. 6.8. Absolute phase of (a) Φ_{full}, (b) Φ_{half}, and (c) $\Delta\Phi_{AM}$ produced by AM2. Absolute phase of (d) $\Delta\Phi_{half}$, (e) $Avg[\Delta\Phi_{half}]$, and (f) $\Delta_2\Phi_{half}$ produced by RAM41.

Fig. 6.9 shows $|\Delta\Phi_{AM}|$ produced by AM1 and AM2. We observed that $|\Delta\Phi_{AM}|$ of AM1 at most of the tissue regions is higher than 0.1 rad. In contrast, $|\Delta\Phi_{AM}|$ of AM2 at most of the tissue regions has a lower value. As a result, it may be easier to segment contrast and tissue signals with a phase threshold for AM2 compared to AM1. We then compared the mean phase difference in the contrast region produced by different apertures. The ROI for calculating the average value of the phase

differences in the contrast region is shown in red in **Fig. 6.7** (a). As shown in **Fig. 6.10** (a), AM1 produced the highest $|\Delta\Phi_{AM}|$ (blue line) and RAM_{41} produced the lowest from the aperture patterns considered. This suggests that uniform p_h and p_{h*} fields would produce higher $|\Delta\Phi_{AM}|$. On the other hand, RAM_{41} produced the highest $|\Delta_2\Phi_{half}|$ (black line) and AM produced the lowest compared to other apertures. This confirms what we expected from equation (5) that more spatially different p_h and p_{h*} fields (**Fig. 6.4**) would produce higher $|\Delta_2\Phi_{half}|$. Finally, we observed that $|\Delta\Phi_{max}|$ (pink line) is larger than $|\Delta\Phi_{AM}|$ and $|\Delta_2\Phi_{half}|$ for all apertures. Images segmented with $\Delta\Phi_{max}$ will have higher CTR.

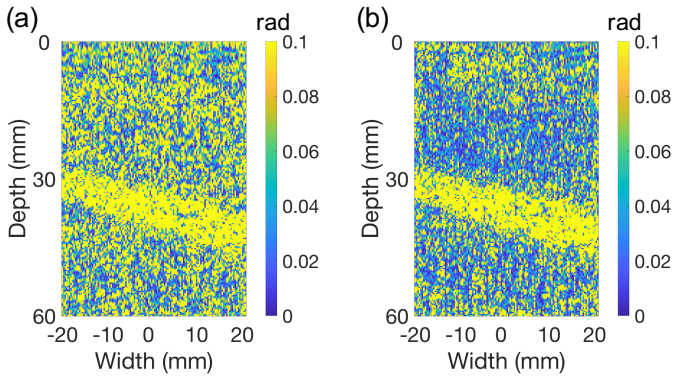

Fig. 6.9. The phase difference ($\Delta\Phi_{AM}$) between ps_{full} and $ps_h + ps_{h*}$ in images produced with AM1 (a) and AM2 (b).

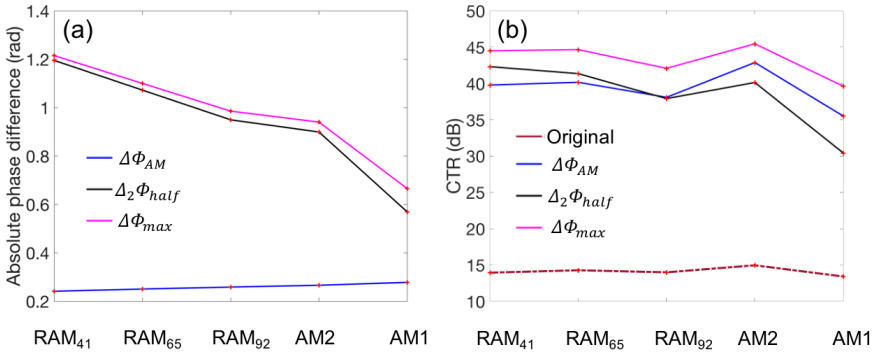

Fig. 6.10. (a) 3 types of phase differences ($\Delta\Phi_{AM}$, $\Delta_2\Phi_{half}$, and $\Delta\Phi_{max}$) produced by 5 different apertures. (b) The CTR of the image produced by the 5 apertures before and after phase segmentation with $\Delta\Phi_{AM}$, $\Delta_2\Phi_{half}$, or $\Delta\Phi_{max}$.

In **Fig. 6.10** (b) we show the CTR of the images segmented with different phase segmentation approaches. The ROIs for calculating CTR of the image are shown in **Fig. 6.7** (a). The CTR of the image produced by different apertures without phase segmentation are shown as brown dashed

line in **Fig. 6.10** (b). When the images were segmented with $\Delta\Phi_{AM}$ (blue line), the images produced by AM2 have the highest CTR (42.9 dB), 7.4 dB higher than that produced by AM1 (35.5 dB). Images produced by the RAM approach have 2.6-4.6 dB higher CTR than that produced by AM1. Although AM1 produced the highest $|\Delta\Phi_{AM}|$ in the contrast region [**Fig. 6.10** (a)], it has the lowest CTR due to lower tissue signal suppression that compromised the CTR. Next, when the images were segmented with $\Delta_2\Phi_{half}$ (black line), those produced by RAM_{41} have the highest CTR (42.3 dB), 11.9 dB higher than that produced by AM1 (30.4 dB). The images produced by RAM_{65} have the second highest CTR (41.3 dB) while the images produced by AM1 have the lowest CTR. This trend is consistent with what we observed in **Fig. 6.10** (a), where RAM produced larger $\Delta_2\Phi_{half}$ than AM1 and AM2. Therefore, it would be optimal to segment contrast signals with $\Delta_2\Phi_{half}$ in images produced by RAM. Finally, when images were segmented with $\Delta\Phi_{max}$ (pink line), the ones produced by AM2 have the highest CTR (45.5 dB), 5.9 dB higher than that produced by AM1 (39.6 dB). We observed a 2.6-4.7 dB improvement in CTR (depending on combination of aperture pattern) when the images were segmented with $\Delta\Phi_{max}$ compared to when segmented with $\Delta\Phi_{AM}$. The images produced with AM2 and segmented with $\Delta\Phi_{max}$ have the highest CTR compared to that produced by any other aperture pattern and segmentation approach.

CEUS images of a flow phantom produced by AM1 and AM2, each segmented with $\Delta\Phi_{AM}$ or $\Delta\Phi_{max}$ are shown in **Fig. 6.11**. The $\Delta\Phi_{th}$ value used in each case is shown in the figure. We observed that the segmented images [(b), (c), (e), and (f)] have better tissue signal suppression compared to the original images [(a) and (d)], yet some contrast signals were inevitably lost. Comparing images segmented with $\Delta\Phi_{max}$ [(c) and (f)] with those segmented with $\Delta\Phi_{AM}$ [(b) and (e)], we observed that the bubbles were brighter and the tissue dimmer than the images segmented with $\Delta\Phi_{AM}$. We also observed that the bubbles were brighter in the segmented AM2 images [(e) and (f)] compared to those with AM1 [(b) and (c)]. When using $\Delta\Phi_{AM}$ for segmentation, AM2 has higher CTR than AM1 since it has better tissue signal suppression and it requires a smaller $\Delta\Phi_{th}$ value to remove tissue signals. Using a smaller $\Delta\Phi_{th}$ value would preserve more contrast signals in the image. When using $\Delta\Phi_{max}$ for segmentation, AM2 has more contrast signals than AM1 since AM2 produced a much higher $|\Delta\Phi_{max}|$ than AM1 as it is shown in **Fig. 6.10** (a).

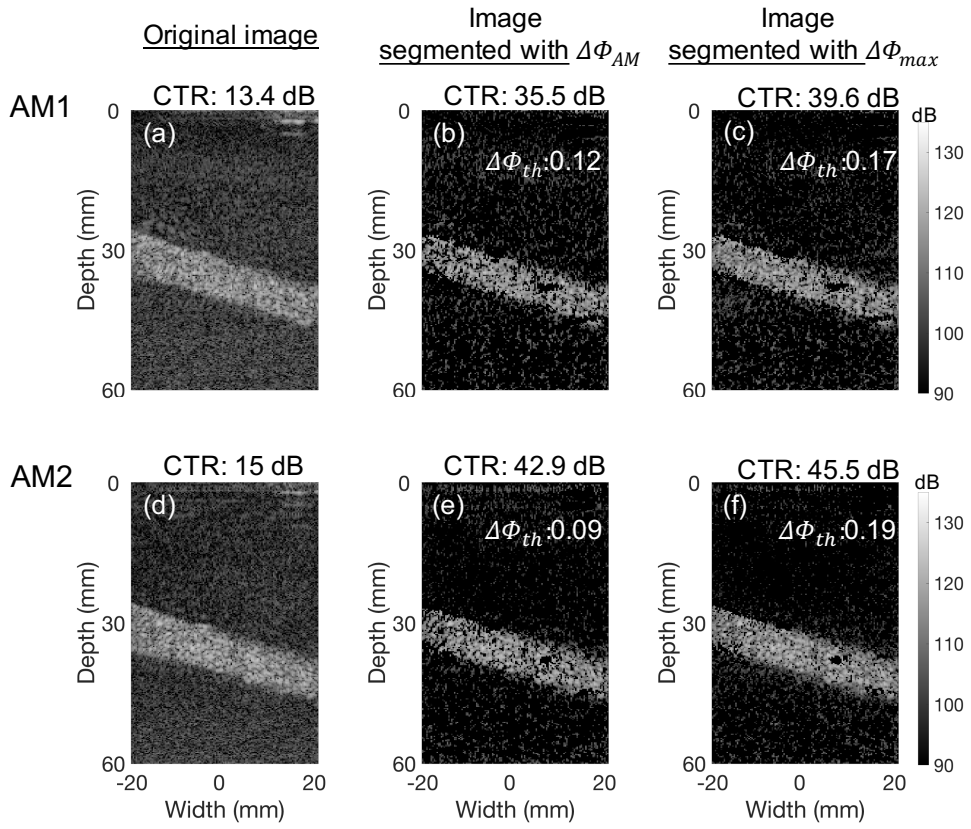

Fig. 6.11. CEUS images of a flow phantom produced by AM1 (a) and AM2 (b), each segmented with $\Delta\Phi_{AM}$ (b, e) and $\Delta\Phi_{max}$ (c, f)

CEUS images from the perfused liver produced by AM2 before and after phase segmentation with $\Delta\Phi_{max}$ at different time points during a bolus injection (0, 9, and 13 sec) are shown in **Fig. 6.12** (a)-(f). $Avg[\Delta\Phi_{half}]$ from 100 images before any microbubbles arrived was used for calculating $\Delta_2\Phi_{half}$ [equation (5)]. We observed that before microbubbles arrived (at $t = 0$ s), the image segmented with $\Delta\Phi_{max}$ (b) has better tissue signal suppression than without phase segmentation (a). The strong reflections from the cloth membrane holding the liver were also reduced in (b). The signals at the bottom left corner of the image were true contrast signals produced by microbubbles flowing in the solution. When the microbubbles first arrived in the field of view through the artery (at $t = 9$ s), we observed in (d) that performing phase segmentation with $\Delta\Phi_{max}$ was still able to remove most of the tissue signals and reflections from the plastic plate in (c) without losing much of the contrast signals. Finally, when more microbubbles were in the liver at 13 s, the difference between (e) and (f) was small since most of the signals were produced by microbubbles. However, reflections from the plastic plate were not removed in (f) due to the nonlinear propagation artifact

generated by contrast agents [31]. The TICs in **Fig. 6.12** (g) show that AM2 (red line) has slightly better tissue signal suppression and thus better image contrast compared to AM1 (blue line) before segmentation. We next compared TICs calculated from images after segmentation in (h). We observed that the TIC from images produced by AM2, segmented with $\Delta\Phi_{max}$ (pink line), shows better tissue signal suppression while preserving more contrast signals compared to that produced by AM1, segmented with $\Delta\Phi_{AM}$ (black line).

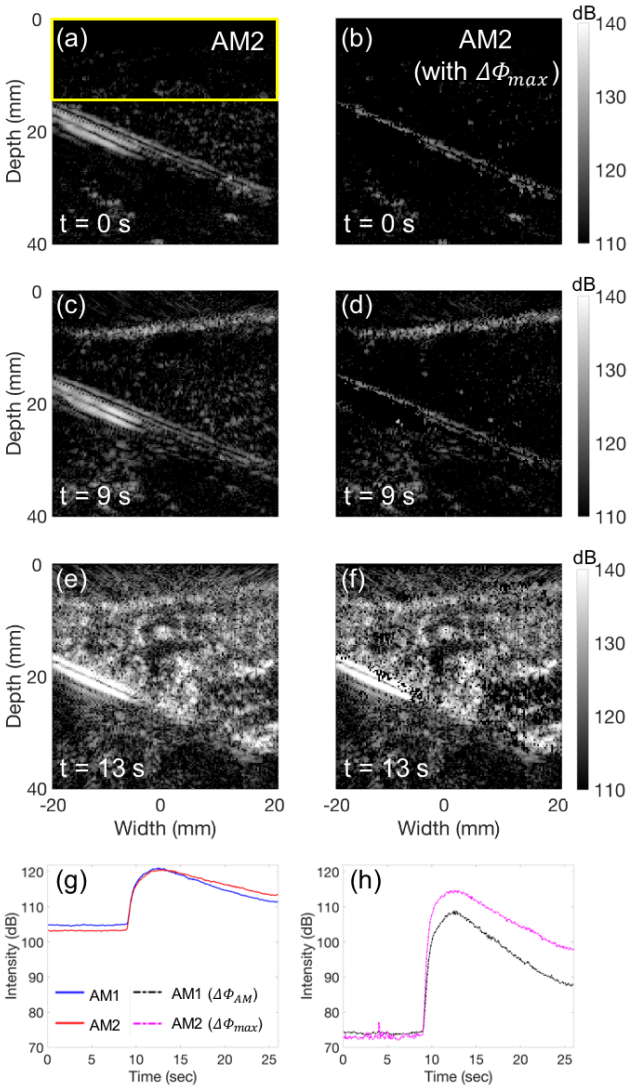

Fig. 6.12. (a)-(f) CEUS images produced by AM2 before and after segmentation with $\Delta\Phi_{max}$ at different time points (0, 9, and 13 sec) in the image loop . The time intensity curves acquired with AM1 (g) and AM2 (h)before and after segmentation. The ROI for tracking the time intensity curve is shown in yellow in (a).

6.4 DISCUSSION

6.4.1 *Implications of aperture patterns for contrast imaging*

We first evaluated the acoustic fields produced by different apertures. Although it is impossible to evaluate every possible aperture pattern, the 26 apertures evaluated in this study provided a good variety to examine the overlap between complementary apertures and the number of on/off interfaces (**Fig. 6.2**), for optimal CTR.

We observed in **Fig. 6.4** that the peak pressure of p_h field is higher when the 2 AM complementary apertures are less overlapped with each other. Since the nonlinear signals in AM arise because the microbubbles respond nonlinearly to different amplitude pulses [4, 32], the sensitivity of detecting contrast signals with AM is reduced when the peak pressure of p_h or p_{h*} field is closer to the peak pressure of p_{full} field. A clear example of this phenomenon is shown in **Fig. 6.6** (a), where the intensity of contrast signals is much lower in the region that the p_h and p_{h*} fields are not overlapped (side regions) compared to the region that the edges of p_h and p_{h*} fields are slightly overlapped (center region). When the complementary apertures are highly overlapped the sensitivity of detecting contrast signals is greatly improved.

An approach to minimize the number of on/off interfaces for better tissue signal suppression while maintaining large overlap between p_h and p_{h*} fields is to use alternating groups of multiple elements for p_h and p_{h*} (e.g., 2 on, 2 off) as it is shown in **Fig. 6.4** (e). However, we observed that the peak pressure of the p_h or p_{h*} fields increased when more elements are grouped together in the aperture pattern. As shown in **Fig. 6.4**, the peak pressure of the produced field is higher when every other 3 or 5 elements are used for transmit [**Fig. 6.4** (d) and (c), respectively] compared to when using even elements for transmit [**Fig. 6.4** (f)]. Although grouping more elements for transmit may further reduce the effect of crosstalk between on/off elements, the sensitivity of detecting contrast signals may also be compromised since the peak pressure of the produced p_h and p_{h*} fields would be closer to that of p_{full} field.

Moreover, we observed increased generation of grating lobes in p_h and p_{h*} fields when using groups of 3 or more elements for p_h and p_{h*} [**Fig. 6.4** (c) and (d)]. A grating lobe is an unwanted feature of the ultrasound beam that produces image artifacts, and it is generated as a result of undersampling of the spatial frequencies in the transmitted ultrasound beams [33]. We observed increased image artifacts produced by grating lobes in the nearfield (pointed by a red arrow) in **Fig. 6.13** (b) compared to that in **Fig. 6.13** (c) since the gap between transmitting elements is larger (compare for example **Fig. 6.4** (d) and (f)). In addition, the angle of the grating lobes from the center axis is smaller when the spacing between individual elements is larger [34, 35]. Further increasing the gap between transmitting elements has a similar effect to the angle of the grating lobes. We observed that as the gap between transmitting elements increased from that in **Fig. 6.4** (d) to that in **Fig. 6.4** (c), the angle of the grating lobes is reduced, producing image artifacts at deeper regions of the image in **Fig. 6.13** (a). As it is shown in **Fig. 6.13** (a), we observed increased image artifacts in deeper regions (15-30 mm) compared to that in (b) and (c).

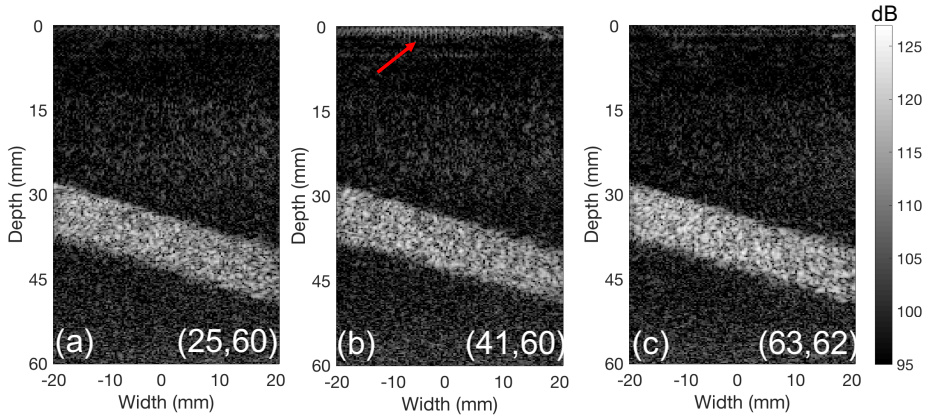

Fig. 6.13. CEUS images of a flow phantom produced by the 3 (out of the 26) apertures evaluated in this study. The numbers in parenthesis in the figure represents the number of on/off interfaces and overlap in terms of elements of the complementary apertures, respectively.

We found that the aperture pattern that uses alternating groups of 2 elements (2 on, 2 off) for this specific probe/frequency had the highest CTR. This is due to AM2 having comparable contrast sensitivity to AM1, yet better tissue signal suppression. When comparing AM2 to the aperture patterns that use alternating groups of 3 or more elements, AM2 has better contrast sensitivity and less image artifacts produced by grating lobes. However, different combinations of aperture

patterns were only tested on an L7-4 array in this study. Since the degree of crosstalk and the generation of the grating lobes is highly related to the specification of the imaging array such as the width and kerf of the individual element and the frequency, it is possible that AM3 or AM4 have better CTR than AM2 when they are implemented on other arrays.

6.4.2 *Phase segmentation of the microbubble signals*

According to the Rayleigh scattering theory, the phase difference in tissue echoes from full and half amplitude pulses should be close to zero [21, 36] when imaging at low MIs (MI ≤0.1) and generation of tissue harmonics is negligible. However, even at low MIs, the crosstalk between on/off elements may affect the precision of the pulse and therefore compromise the degree of tissue signal cancellation, resulting in false phase differences in the tissue [Fig. 9(a)] Since AM2 has better tissue signal suppression compared to AM1, tissue has lower $|\Delta\Phi_{AM}|$ in the image produced with AM2 than that with AM1 (**Fig. 6.9**). Consequently, it would be easier to segment contrast signals from tissue signals when using AM2 than when using AM1. As it is shown in **Fig. 6.10** (b) and **Fig. 6.11**, images of AM2 have greater CTR improvement after segmentation with $\Delta\Phi_{AM}$ compared to that of AM (28 dB vs 22 dB, respectively).

In addition, we demonstrated that it is feasible to utilize the phase difference ($\Delta_2\Phi_{half}$) between complementary half amplitude pulses for segmentation of contrast signals. We found that $\Delta_2\Phi_{half}$ increased as p_h and p_{h*} fields are more spatially dissimilar from each other. RAM produced larger $|\Delta_2\Phi_{half}|$ compared to AM1 and AM2. Although AM2 also have similar p_h and p_{h*} fields, $|\Delta_2\Phi_{half}|$ produced by AM2 is 0.3 rad larger than that produced by AM1 and only 0.05-0.3 rad lower than that produced by RAMs.

We observed in **Fig. 6.10** (b) that images segmented with $\Delta\Phi_{max}$ have higher CTR than that segmented with either $\Delta\Phi_{AM}$ or $\Delta_2\Phi_{half}$. Since microbubbles have different phase response in $\Delta\Phi_{AM}$ and $\Delta_2\Phi_{half}$, a microbubble that has small phase difference in $\Delta\Phi_{AM}$ may have high phase difference in $\Delta_2\Phi_{half}$ and vice versa. Utilizing both $\Delta\Phi_{AM}$ and $\Delta_2\Phi_{half}$ at the same time for segmentation may therefore increases the CTR. Since tissue is expected to have low phase

difference, it is reasonable to combine $\Delta\Phi_{AM}$ and $\Delta_2\Phi_{half}$ by using the maximum absolute phase difference ($\Delta\Phi_{max}$) at every point (*i,j*) between $|\Delta\Phi_{AM}|$ and $|\Delta_2\Phi_{half}|$. Higher contrast sensitivity is very important in the segmentation process to remove tissue signals without losing much contrast signals. As it is shown in **Fig. 6.11**, since $\Delta\Phi_{max}$ has higher contrast sensitivity than $\Delta\Phi_{AM}$, a higher threshold value $\Delta\Phi_{th}$ can be used for images segmented with $\Delta\Phi_{max}$ to further improve tissue signal suppression without losing much of the contrast signals compared to that segmented with $\Delta\Phi_{AM}$ only. This trend was also demonstrated in the perfused pig liver [**Fig. 6.12** (h)], where the TIC in images segmented with $\Delta\Phi_{max}$ shows better tissue signal suppression (lower intensity before microbubble appeared) and higher contrast sensitivity (higher intensity when microbubbles were well perfused) compared to that in the images segmented with $\Delta\Phi_{AM}$. The enhanced tissue signal suppression and contrast sensitivity offered by the proposed segmentation approach may be beneficial to imaging techniques that require high bubble specificity such as super-resolution imaging.

However, we observed in **Fig. 6.12** that although the phase segmentation technique had good tissue signal suppression on the reflections from the cloth membrane when no bubbles were present, it offered less improvements when bubbles were present due to the nonlinear propagation artifact. This is due to the ultrasound pulse being distorted after passage through dense microbubbles [31].

Although phase segmentation may not affect some perfusion parameters derived from TIC such as time to peak and rise time, it could potentially influence as the calculation of peak intensity, and area under the curve [4]. Further studies are needed to investigate if using the perfusion parameters derived from the TIC in images after phase segmentation improves or reduces the accuracy of using those parameters for diagnosis.

Finally, phase variations as a result of microbubble destruction at high pressure amplitudes (4.7 MPa) have been previously reported [37] and utilized as an imaging technique [38]. However, the generation of tissue harmonics at high MIs could also cause phase differences in tissue. In addition, certain microbubble contrast agents, such as Sonazoid (GE Healthcare, Amersham, UK), are used at higher MIs [39], and could potentially benefit from the proposed segmentation techniques here to improve tissue signal suppression.

6.5 Conclusion

We have evaluated plane wave AM aperture approaches including random apertures (reported here for first time) for CEUS in terms of CTR in a flow phantom and a perfused pig liver. We demonstrated that the cross talk between neighboring elements and the overlap of the effective apertures used in AM are the two main optimization parameters. We found that AM2 which uses alternating groups of 2 elements (2 on, 2 off) had the highest CTR, at least 2 dB higher than that of conventional AM. We also developed a bubble-tissue segmentation approach based on differences in the phase of the echoes from the individual ultrasound firings in AM in order to further increase the CTR. We demonstrated that by using phase differences between the full pulse and the half pulse as well as between the two complimentary half pulses we can increase the CTR of CEUS images by further suppressing tissue signals and noise. We have reported CTR increases of 20-25 dB in vitro and ex vivo. Our approach here may be applied to other probes and clinical applications as well.

6.6 Acknowledgments

The research reported in this study was supported by the National Institute of Biomedical Imaging and Bioengineering of the National Institutes of Health under Award Number T32EB001650 and College of Engineering Fellowship from the James Chao-Yao Koh and Maria Lee Koh Endowed Fellowship fund. We would like to thank Thanasis Loupas for valuable discussions and comments on the phase calculations.

6.7 References

[1] T. Leighton, *The acoustic bubble*. Academic press, 2012.
[2] H. Becher and P. N. Burns, *Handbook of contrast echocardiography: Left ventricular function and myocardial perfusion*. Springer Science & Business Media, 2012.
[3] S. R. Wilson, P. N. Burns, D. Muradali, J. A. Wilson, and X. Lai, "Harmonic hepatic US with microbubble contrast agent: initial experience showing improved characterization of

hemangioma, hepatocellular carcinoma, and metastasis," *Radiology,* vol. 215, no. 1, pp. 153-161, 2000.
[4] M. A. Averkiou, M. F. Bruce, J. E. Powers, P. S. Sheeran, and P. N. Burns, "Imaging methods for ultrasound contrast agents," *Ultrasound in medicine & biology,* vol. 46, no. 3, pp. 498-517, 2020.
[5] M. D'Onofrio, S. Crosara, R. De Robertis, S. Canestrini, and R. P. Mucelli, "Contrast-enhanced ultrasound of focal liver lesions," *American journal of roentgenology,* vol. 205, no. 1, pp. W56-W66, 2015.
[6] F. Piscaglia *et al.*, "Characterization of focal liver lesions with contrast-enhanced ultrasound," *Ultrasound in medicine & biology,* vol. 36, no. 4, pp. 531-550, 2010.
[7] M. Tanter and M. Fink, "Ultrafast imaging in biomedical ultrasound," *IEEE transactions on ultrasonics, ferroelectrics, and frequency control,* vol. 61, no. 1, pp. 102-119, 2014.
[8] J. Provost *et al.*, "3D ultrafast ultrasound imaging in vivo," *Physics in Medicine & Biology,* vol. 59, no. 19, p. L1, 2014.
[9] O. Couture, M. Fink, and M. Tanter, "Ultrasound contrast plane wave imaging," *IEEE transactions on ultrasonics, ferroelectrics, and frequency control,* vol. 59, no. 12, pp. 2676-2683, 2012.
[10] C. Errico, B.-F. Osmanski, S. Pezet, O. Couture, Z. Lenkei, and M. Tanter, "Transcranial functional ultrasound imaging of the brain using microbubble-enhanced ultrasensitive Doppler," *NeuroImage,* vol. 124, pp. 752-761, 2016.
[11] C. Errico *et al.*, "Ultrafast ultrasound localization microscopy for deep super-resolution vascular imaging," *Nature,* vol. 527, no. 7579, pp. 499-502, 2015.
[12] D. H. Simpson, C. T. Chin, and P. N. Burns, "Pulse inversion Doppler: a new method for detecting nonlinear echoes from microbubble contrast agents," *IEEE transactions on ultrasonics, ferroelectrics, and frequency control,* vol. 46, no. 2, pp. 372-382, 1999.
[13] G. A. Brock-Fisher, M. D. Poland, and P. G. Rafter, "Means for increasing sensitivity in non-linear ultrasound imaging systems," ed: Google Patents, 1996.
[14] V. Mor-Avi, E. G. Caiani, K. A. Collins, C. E. Korcarz, J. E. Bednarz, and R. M. Lang, "Combined assessment of myocardial perfusion and regional left ventricular function by analysis of contrast-enhanced power modulation images," *Circulation,* vol. 104, no. 3, pp. 352-357, 2001.
[15] P. Phillips and E. Gardner, "Contrast-agent detection and quantification," *European radiology,* vol. 14, pp. P4-10, 2004.
[16] C. Tremblay-Darveau, "Contrast-enhanced Doppler ultrasound imaging using plane waves," 2016.
[17] T.-Y. Lai and M. A. Averkiou, "Linear Signal Cancellation of Nonlinear Pulsing Schemes in a Verasonics Research Scanner," *IEEE Transactions on Ultrasonics, Ferroelectrics, and Frequency Control,* vol. 68, no. 5, pp. 1721-1728, 2021.
[18] M. F. Hamilton and D. T. Blackstock, *Nonlinear acoustics*. Academic press San Diego, 1998.
[19] P.-C. Li, C.-C. Shen, and S.-W. Huang, "Waveform design for ultrasonic pulse-inversion fundamental imaging," *Ultrasonic imaging,* vol. 28, no. 3, pp. 129-143, 2006.
[20] P. Phillips, "Contrast pulse sequences (CPS): imaging nonlinear microbubbles," in *2001 IEEE Ultrasonics Symposium. Proceedings. An International Symposium (Cat. No. 01CH37263)*, 2001, vol. 2, pp. 1739-1745: IEEE.

[21] C. Tremblay-Darveau *et al.*, "The role of microbubble echo phase lag in multipulse contrast-enhanced ultrasound imaging," *IEEE transactions on ultrasonics, ferroelectrics, and frequency control,* vol. 65, no. 8, pp. 1389-1401, 2018.
[22] J. A. Jensen and N. B. Svendsen, "Calculation of pressure fields from arbitrarily shaped, apodized, and excited ultrasound transducers," *IEEE transactions on ultrasonics, ferroelectrics, and frequency control,* vol. 39, no. 2, pp. 262-267, 1992.
[23] J. A. Jensen, "Field: A program for simulating ultrasound systems," in *10TH NORDICBALTIC CONFERENCE ON BIOMEDICAL IMAGING, VOL. 4, SUPPLEMENT 1, PART 1: 351--353*, 1996: Citeseer.
[24] C. Kasai, K. Namekawa, A. Koyano, and R. Omoto, "Real-time two-dimensional blood flow imaging using an autocorrelation technique," *IEEE Transactions on sonics and ultrasonics,* vol. 32, no. 3, pp. 458-464, 1985.
[25] M.-L. Izamis, A. Efstathiades, C. Keravnou, E. L. Leen, and M. A. Averkiou, "Dynamic contrast-enhanced ultrasound of slaughterhouse porcine livers in machine perfusion," *Ultrasound in medicine & biology,* vol. 40, no. 9, pp. 2217-2230, 2014.
[26] C. Dietrich, M. Averkiou, J.-M. Correas, N. Lassau, E. Leen, and F. Piscaglia, "An EFSUMB introduction into Dynamic Contrast-Enhanced Ultrasound (DCE-US) for quantification of tumour perfusion," *Ultraschall in der Medizin-European Journal of Ultrasound,* vol. 33, no. 04, pp. 344-351, 2012.
[27] S. Aoki *et al.*, "Contrast-enhanced ultrasound using a time-intensity curve for the diagnosis of renal cell carcinoma," *BJU international,* vol. 108, no. 3, pp. 349-354, 2011.
[28] X. Pei *et al.*, "Quantitative analysis of contrast-enhanced ultrasonography: differentiating focal nodular hyperplasia from hepatocellular carcinoma," *The British journal of radiology,* vol. 86, no. 1023, p. 20120536, 2013.
[29] N. Lassau *et al.*, "Validation of dynamic contrast-enhanced ultrasound in predicting outcomes of antiangiogenic therapy for solid tumors: the French multicenter support for innovative and expensive techniques study," *Investigative radiology,* vol. 49, no. 12, p. 794, 2014.
[30] C. P. Keravnou, I. De Cock, I. Lentacker, M.-L. Izamis, and M. A. Averkiou, "Microvascular injury and perfusion changes induced by ultrasound and microbubbles in a machine-perfused pig liver," *Ultrasound in medicine & biology,* vol. 42, no. 11, pp. 2676-2686, 2016.
[31] A. Thapar, J. Shalhoub, M. Averkiou, C. Mannaris, A. H. Davies, and E. L. Leen, "Dose-dependent artifact in the far wall of the carotid artery at dynamic contrast-enhanced US," *Radiology,* vol. 262, no. 2, pp. 672-679, 2012.
[32] R. Eckersley, "Contrast Media, Ultrasound, Amplitude Modulation," in *Encyclopedia of Diagnostic Imaging*, A. L. Baert, Ed. Berlin, Heidelberg: Springer Berlin Heidelberg, 2008, pp. 522-522.
[33] A. Ilovitsh, T. Ilovitsh, and K. W. Ferrara, "Multiplexed ultrasound beam summation for side lobe reduction," *Scientific reports,* vol. 9, no. 1, pp. 1-8, 2019.
[34] Y. Paul, D. Barthez, R. Léveillé, V. Peter, and D. Scrivani, "Side lobes and grating lobes artifacts in ultrasound imaging," *Veterinary Radiology & Ultrasound,* vol. 38, no. 5, pp. 387-393, 1997.
[35] T. L. Szabo, *Diagnostic ultrasound imaging: inside out*. Academic press, 2004.
[36] R. S. Cobbold, *Foundations of biomedical ultrasound*. Oxford university press, 2006.

[37] J. E. Chomas, P. Dayton, J. Allen, K. Morgan, and K. W. Ferrara, "Mechanisms of contrast agent destruction," *IEEE transactions on ultrasonics, ferroelectrics, and frequency control,* vol. 48, no. 1, pp. 232-248, 2001.

[38] M. Siepmann *et al.*, "Phase shift variance imaging-a new technique for destructive microbubble imaging," *IEEE transactions on ultrasonics, ferroelectrics, and frequency control,* vol. 60, no. 5, pp. 909-923, 2013.

[39] J. Y. Jang *et al.*, "Current consensus and guidelines of contrast enhanced ultrasound for the characterization of focal liver lesions," *Clinical and molecular hepatology,* vol. 19, no. 1, p. 1, 2013.

Chapter 7. CONCLUSIONS

This thesis has investigated the beamforming approaches for combining ultrafast imaging and nonlinear ultrasound imaging techniques; (1) tissue harmonic imaging (THI) and (2) contrast-enhanced ultrasound (CEUS). In this work, we used the numerical model we developed based on KZK equation to identify optimal beamforming approach for ultrafast THI that still produces a good level of 2nd harmonic in tissue. We also proposed a segmentation approach for ultrafast CEUS by using the difference between the phase response of microbubble and tissue as a criterion to improve tissue signal suppression in CEUS images. This work lays down the fundamental concepts and trade-offs in beamforming approaches for ultrafast THI and ultrafast CEUS.

7.1 ULTRAFAST TISSUE HARMONIC IMAGING (CHAPTER 2-3)

Combining plane/diverging wave imaging (PWI/DWI) and THI for ultrafast THI offers improvements in image quality in PWI/DWI. Some previous studies suggested it would be a challenge to produce sufficient harmonic components using plane/diverging waves due to the reduced amplitudes. A first step in this thesis was to investigate the feasibility of ultrafast THI by calculating the 2nd harmonic component generated by these fields in tissue with a robust and reliable model of nonlinear propagation in tissue. The model we developed to study nonlinear propagation of ultrasound produced by diagnostic arrays in plane or diverging wave mode is based on the Khokhlov-Zabolotskaya-Kuznetsov (KZK) equation. We have first confirmed the ability of our model to simulate the linear field by comparing it with the Field II simulation which is widely accepted in the field of ultrasound as an accurate model of linear propagation. We have found good agreement between the 2 models with mean relative differences being less than 5%. Field II cannot calculate the nonlinear field though, but our model can. To validate our model in terms of nonlinear propagation, we have compared simulations of nonlinear propagation with hydrophone measurements in water and good agreement was found. Our numerical model opens the door to further investigations evaluating the nonlinear field produced by diagnostic arrays operating in plane/diverging wave modes and various investigation of new imaging modes that require this type of beamforming. This work also allows us to study the spatial extend of the second harmonic component in ultrafast THI, which was not possible before our model.

In echocardiography, THI is crucial for improving cardiac images of CVD patients, who are often overweight and difficult to image due to various image artifacts. Compared to conventional 2D imaging, live 3D imaging with a matrix array enables physicians to examine 3D cardiac structures in real-time and in a more intuitive manner. However, current commercial live 3Dultrasound systems typically rely on conventional beamforming techniques to sample the volume and are thus limited to a few volumes per second at best. In order to produce acceptable volume rates in live 3D cardiac THI, broader beams and/or PWI and DWI approaches must be used. To the best of our knowledge, our work is the first in-depth investigation of harmonic generation in tissue with a matrix array and while utilizing broad beam approaches. We investigated the harmonic generation of a matrix array for finding the optimal beamforming strategies for live 3D cardiac THI that still produce a good level of second harmonic in tissue. From this work we identified that the transducer surface temperature is the main amplitude (fundamental and second harmonic) limiting factor, as opposed to the *MI*, I_{sppa}, or I_{spta}. The peak 2nd harmonic component produced by PWI was found to be 9-20 dB lower than that produced by conventional focused beamforming approaches when maintaining the transducer temperature to the maximum allowable value. The 2nd harmonic component produced by DWI was 23-40 dB lower than that of a conventional focused beamforming approach. Despite the lower level of second harmonic component produced by PWI/DWI, the SNR can be partly recovered by receive beamforming techniques such as coherent compounding and delay-encoded harmonic imaging techniques. Therefore, it may still be feasible to use PWI and DWI for live 3D cardiac THI. In addition, recent developments in shear-wave elastography (SWE) have led to improvements in heat removal and deposition, which have mitigated the problem of transducer surface heating and may lead to the use of higher source pressures for live 3D cardiac THI. We have shown in our previous work that when operated at the same MI of 1.9, the 2nd harmonic generated by PWI/DWI in tissue was found to be only 2-16 dB lower than that of focused beams. This result highlights the importance of using higher source pressure for live 3D cardiac THI. The volume rates for the beamforming approaches we have considered for live 3D cardiac THI are in the range 1-8 Hz with conventional focused beamforming (depending on the focal depths), 44 Hz with PWI, and 444 Hz with DWI. This work provides useful insight into the compromise between the magnitude and the spatial extent of the 2nd

harmonic produced by different beamforming approaches, and outlines an analytical framework for identifying optimal beamforming approaches for specific applications.

7.2 ULTRAFAST CONTRAST ENHANCED ULTRASOUND (CHAPTER 4-6)

Linear (tissue) signal cancellation (LSC) is an important requirement for good CTR in CEUS. Incomplete tissue signal cancellation reduces the CTR and may mask real enhancement caused by microbubbles or be incorrectly interpreted as real enhancement. A first step in this work was to investigate the LSC performance of two scanners, the Verasonics and the Philips iU22, in pulse inversion (PI) and amplitude modulation (AM) mode which has not been investigated before. This work is important in identifying the optimal nonlinear pulsing scheme for performing contrast imaging with the Verasonics research scanner. We found that at low MI (≤0.1), both scanners (the Verasonics and the iU22) had a greater LSC in AM (~40 dB) than PI (~30 dB). As a result, AM may be preferred over PI when the clinical application requires high bubble specificity due to having a higher LSC. In addition, our published work in this area describes in detail how PI and AM are implemented on the Verasonics scanner which may be helpful to future researchers trying to implement these pulsing schemes on a research scanner.

In addition, the LSC of AM was found to be generally lower in plane/diverging wave mode than in conventional focused mode. We were able to identify that this is due to crosstalk between transmitting and non-transmitting elements. In addition, we have explained that the degree of physical overlap between the two complimentary apertures in AM pulse sequences may also impact the nonlinear response from microbubbles. Using an alternative pattern (instead of even and odd elements or every other element) for AM may reduce the degree of crosstalk between on/off elements while generating more nonlinear microbubble response compared to that generated by AM. We evaluated the image quality of ultrafast CEUS when imaging with different combinations of aperture pattern and suggested an optimal combination for AM that would improve tissue signal suppression and image contrast for ultrafast CEUS. We observed that the aperture using alternating groups of 2 elements (2 on, 2 off which we call AM2) had the highest CTR, ~2 dB higher than conventional AM1. For example, although AM1 and AM2 have similar

overlap of complementary apertures, AM2 has half the number of on/off interfaces, which indicates lower cross talk and thus better tissue signal suppression.

The image quality of CEUS is also limited by the tissue harmonics generated from the nonlinear propagation of sound waves in tissue. We used the phase difference between the full and half amplitude echoes ($\Delta\Phi_{AM}$) for tissue and microbubble echoes as a segmentation technique to distinguish bubbles from tissue. To study $\Delta\Phi_{AM}$ we evaluated the amplitude-dependent phase difference in tissue and free gas bubbles. We observed phase differences on the order of |0.025 rad| from tissue, lower than that of simulated free gas bubbles (up to |1.4| rad), shelled microbubbles (up to |1.8| rad) and experimentally measured commercial microbubbles (up to |0.4-1| rad). Previous studies believe that $\Delta\Phi_{AM}$ are generated solely by the shell properties of the microbubbles. However, we have demonstrated in this work that $\Delta\Phi_{AM}$ may also be an effect of both nonlinear propagation in tissue and nonlinear oscillations of the gas core of the microbubble.

It is necessary to have larger phase difference in microbubbles than that in tissue for phase segmentation techniques to accurately segment microbubble signals from tissue signals. The phase difference ($\Delta_2\Phi_{half}$) between echoes from complementary half amplitude pulses results from the difference between the spatial distribution (diffraction pattern) of the complementary fields. We demonstrated that it is feasible to also use $\Delta_2\Phi_{half}$ for segmentation of microbubble signals from tissue signals. We observed that $\Delta_2\Phi_{half}$ increases as the complementary fields are spatially more dissimilar. Finally, we proposed a segmentation approach that utilizes not only $\Delta\Phi_{AM}$, but also $\Delta_2\Phi_{half}$ in the AM pulsing sequence. We tested the proposed segmentation approach in a flow phantom and in a perfused pig liver. The proposed segmentation approach was found to have better tissue signal suppression and contrast sensitivity compared to a previous phase segmentation approach. We found that the proposed segmentation approach resulted in a 9.9 dB higher CTR in a flow phantom and higher tissue signal suppression in the TIC curve of a perfused pig liver compared to that acquired with a previous phase segmentation approach. This work provides useful insight into how aperture patterns affects the image quality of ultrafast CEUS, and outlines a framework that may be useful for identifying the optimal aperture pattern of AM for other clinical applications. The enhanced tissue signal suppression and contrast sensitivity offered by the

proposed phase segmentation approach may be beneficial to imaging techniques that requires high bubble specificity such as super-resolution imaging.

Combining ultrafast imaging with THI and CEUS has enabled many innovations such as live 3D cardiac THI, functional ultrasound imaging of the brain, and super-resolution imaging. We hope that the present work provides a fundamental scientific basis for the development of ultrafast nonlinear ultrasound imaging techniques and that it will enable its clinical translation in future diagnostic tools.

7.3 FUTURE STUDIES

7.3.1 *Ultrafast THI – quasilinear solution of KZK*

A quadratic relationship of attenuation with frequency is assumed in the KZK predictions in this thesis, whereas tissue attenuation is typically linearly related with frequency. Thus, the absorption at the higher harmonics is slightly overestimated in our nonlinear simulations in tissue. This implies that the difference between 2nd harmonic produced by focused ultrasound and PWI/DWI is slightly overestimated and it would be easier to combine PWI/DWI and THI than what is predicted in this work.

This difference in attenuation may be addressed by implementing the quasilinear solution of KZK equation [1] in the numerical model. A previous study has implemented the quasilinear solution of the KZK for modeling piston sources [2]. However, as far as we are concern, a numerical model based on the quasilinear solution of the KZK has not yet been developed. Future work in this field should then focus on implementing the quasilinear solution of the KZK in the numerical model to provide more accurate predictions of the 2nd harmonic level in tissue.

7.3.2 *Ultrafast THI – reducing computation time for nonlinear simulations*

The KZK field simulation for the linear array took around 4-12 hours (depending on field of view and nonlinearity) to finish. However, the simulation of phase and convex arrays, since not only a smaller step size in x was required to capture the curvature of the wave fronts, but a pulse with a longer tail was also necessary to correctly model the diffraction in regions far away from the main

axis, the simulation took up to 48 hours to finish. The computation time may be quadruple when modeling a non-axisymmetric in both azimuth and elevation plane.

Multi-Gaussian beam (MGB) models have been widely used to describe the propagation of ultrasound beams from planar or focused transducers [3]. One of the advantage of using MGB methods is that it is very computational efficient. The MGB model of the quasilinear solution of the KZK equation is described in a previous study [2]. Implementing the MGB model in our numerical model may dramatically improve the computation time of the model and allow us to use it for modeling the nonlinear acoustic fields produced by non-axisymmetric sources effieciently. For example, modeling the harmonic generation of a 2D sparse array in tissue.

7.3.3 *Ultrafast CEUS – using segmented images for diagnosis*

Time intensity curve (TIC) provides perfusion parameters such as wash-in and wash-out of the microbubbles in a region of interest and it is a useful tool for assessing tumor response after treatment. Although performing segmentation of microbubbles with the phase may not affect some perfusion parameters derived from the TIC such as time to peak and rise time, it may have huge influences on other parameters such as peak intensity, and area under the curve.

Further studies are therefore needed to investigate if using the perfusion parameters derived from the TIC in images after segmentation improves or reduces the accuracy of using those parameters for diagnosis.

7.3.4 *Ultrafast CEUS – aperture patterns for 3D contrast imaging*

Typical 1D arrays have 64-256 elements. However, 2D arrays may have more than 65,000 elements on the array. The impact of crosstalk on the tissue signal cancellation may be way more severe on 2D arrays compared to 1D arrays. On the other hand, 2D arrays offers much more flexible use of aperture patterns to produce acoustic fields that generates more microbubble responses. The addition of another dimension (1D array becomes 2D) dramatically increases the complexity in the aperture optimization process.

Future studies are therefore needed to utilize the knowledge we learned from studying the aperture patterns on the 1D array to identify the optimal AM aperture for a 2D array that improves the tissue signal suppression in 3D contrast imaging. Since 2D arrays produce spatially more dissimilar complementary half amplitude fields when using random apertures (RAM) compared to that produced by 1D arrays. Future studies should also focus on designing specific RAMs to generate additional microbubble responses.

7.4 MAJOR CONTRIBUTIONS TO SCIENCE

The major contributions of this thesis to the fields of ultrafast THI and ultrafast CEUS are as follows:

- We developed and validated a numerical model based on KZK equation for simulations of the nonlinear acoustic fields produced by diagnostic arrays (Ch. 2).
- We determined the difference between the 2^{nd} harmonic generated by conventional focused ultrasound and that generated by ultrafast imaging techniques (Ch. 2).
- We determined the trade-offs between produced 2^{nd} harmonic level and volume rate when using different beamforming approaches for live 3D cardiac THI (Ch. 3).
- We demonstrated the methodology for implementing PI and AM on a Verasonics research ultrasound scanner and we measured the linear signal cancellation of a ultrasound scanner (Ch. 4).
- We demonstrated that AM has higher linear signal cancellation than PI on clinical systems. Therefore, AM may be preferred over PI when the clinical application requires high bubble specificity (Ch. 4).
- We determined the degree of the phase difference between full and half amplitude pulses generated by nonlinear propagation of tissue and nonlinear oscillation from free and shelled gas microbubbles (Ch. 5).
- We identified an aperture pattern that improves the tissue signal cancellation for ultrafast CEUS (Ch.6).

- Proposed and tested a new segmentation approach for ultrafast CEUS, by evaluating the phase difference between complimentary half amplitude pulses in AM pulsing sequence to improve the removal of tissue signals compared to a previous segmentation approach (Ch. 6).

7.5 LIST OF PUBLICATIONS AND PRESENTATIONS

Peer-reviewed publications

1. **Lai, TY**, Averkiou, MA. "Contrast enhanced ultrasound with optimized aperture patterns." *[in preparation]*
    - Chapter 6
2. Keller, SB**, Lai, TY**, Koninck, LD, Averkiou, MA. "Investigation of the phase of the fundamental component of nonlinear echoes during amplitude modulation." *[in review]*
    - Chapter 5
3. **Lai, TY**, Loupas, T, Averkiou, MA. "Harmonic Generation in Tissue with a 2D Matrix Array for 4D Cardiac THI." *[in preparation]*
    - Chapter 3
4. **Lai, TY**, Averkiou, MA. "Linear Signal Cancellation of Nonlinear Pulsing Schemes implemented on the Verasonics Research Scanner." *IEEE Transactions on Ultrasonics, Ferroelectrics, and Frequency Control 68.5 (2021): 1721-1728.*
    - Chapter 4
5. **Lai, TY,** Bruce, M, Averkiou, MA. "Modeling of the Acoustic Field Produced by Diagnostic Ultrasound Arrays in Plane and Diverging Wave Modes." *IEEE transactions on ultrasonics, ferroelectrics, and frequency control 66.7 (2019): 1158-1169.*
    - Chapter 2

Presentations at national and international conferences

1. **Lai, TY,** Averkiou, MA. "Contrast enhanced ultrasound with optimized aperture patterns." 2021 IEEE International Ultrasonics Symposium (poster presentation)

2. Keller, SB**, Lai, TY**, Koninck, LD, Averkiou, MA. "Investigation of the phase of the fundamental component of nonlinear echoes during amplitude modulation." 2021 IEEE International Ultrasonics Symposium (poster presentation)

3. **Lai, TY,** Averkiou, MA. "The Nonlinear Field Produced by 1D and 2D Imaging Arrays with Plane and Diverging Wave Modes for Ultrafast Imaging." 2020 Acoustical Society of America (oral presentation)

4. **Lai, TY,** Averkiou, MA. “Linear Signal Cancellation of Nonlinear Pulsing Schemes implemented on the Verasonics Research Scanner.” 2020 IEEE International Ultrasonics Symposium (poster presentation)

5. **Lai, TY,** Averkiou, MA. “Contrast enhanced ultrasound with optimized aperture patterns.” 26th European Symposium on Ultrasound Contrast Imaging (poster presentation)

6. **Lai, TY,** Kou, S, Bruce, M, Loupas, T, Averkiou, MA. “Harmonic Generation in Tissue with Matrix Arrays for 4D Cardiac THI.” 2019 IEEE International Ultrasonics Symposium (oral presentation)

7. **Lai, TY,** Averkiou, MA. “The Linear and Nonlinear Ultrasound Field of Convex Arrays Operating in a Diverging Wave Mode.” 2018 IEEE International Ultrasonics Symposium (poster presentation)

8. **Lai, TY,** Bruce, M, Averkiou, MA. “Modeling of the Nonlinear Field Produced by Diagnostic Ultrasound Arrays in Plane Wave Mode.” 23rd European Symposium on Ultrasound Contrast Imaging (poster presentation)

9. **Lai, TY,** Bruce, M, Averkiou, MA. “Modeling of the Nonlinear Field Produced by Diagnostic Ultrasound Arrays in Plane Wave Mode.” World Federation for Ultrasound in Medicine and Biology 2017 (oral presentation)

7.6 REFERENCES

[1] M. F. Hamilton and D. T. Blackstock, *Nonlinear acoustics*. Academic press San Diego, 1998.

[2] H. Jeong, S. Zhang, D. Barnard, and X. Li, "Significance of accurate diffraction corrections for the second harmonic wave in determining the acoustic nonlinearity parameter," *AIP Advances,* vol. 5, no. 9, p. 097179, 2015.

[3] J. Wen and M. Breazeale, "A diffraction beam field expressed as the superposition of Gaussian beams," *The Journal of the Acoustical Society of America,* vol. 83, no. 5, pp. 1752-1756, 1988.